Exploring the Influence of thin-film morphology and interfaces on the charge transport in organic electronic devices

（有機電子デバイスの電荷輸送に対する薄膜形態と界面の影響の調査）

DISSERTATION

FOR THE DEGREE OF

DOCTOR OF PHILOSOPHY

NIKITA KUMARI

Supervisor: SHYAM S. PANDEY

Division of Green Electronics

Graduate School of Life Sciences and Systems Engineering

Kyushu Institute of Technology

2020

Dedicated

To

The Almighty God

Abstract

Semiconducting polymers (SCPs) have gained huge scientific interests owing to their excellent optical, electrical, and mechanical properties making them a potential candidate for the practical realization organic electronics. Overall performance of organic electronic devices (OEDs) is being controlled by the nature of the SCPs, their thin-film morphology, and related interfaces. Charge transport in SCPs thin-films is dictated by various phenomena like transport along π-conjugated backbone followed by intermolecular as well as inter-domain hopping. In the recent past, huge efforts have been directed to improve the crystallinity of SCP thin-films by chemical structure engineering, developing various thin-film fabrication techniques, imparting molecular orientation and post-processing of the thin films aiming towards enhancing the charge carrier transport. Existing issues of thin-film fabrications such as the use of toxic halogenated solvents, difficulty in multilayer film fabrication, and swift characterization of large area thin films are still the stumbling blocks towards the large area implementation of the OEDs.

Chapter 1 introduces the concerns related to the present state-of-art in organic electronics, problems related to thin-film fabrication techniques for SCPs, the need for a comprehensive understanding of the SCP/dielectric, SCP/metal interfaces and their implication on the charge carrier transport. The theory of electrical conduction in SCPs, their charge carriers, energy band as well as charge carrier transport, with existing thin-film fabrication techniques has been discussed in detail followed by challenges currently being faced and justification for the aim of the present research work.

In chapter 2, brief outline of the SCPs like P3HT, PBTTT, PQT, their thin-film processing adopting spin-coating, drop-casting, floating film transfer, and friction transfer techniques have been provided. Various techniques used for the characterization and analysis of the oriented thin films along with the fabrication and analysis of various organic electronic devices have been discussed in detail.

3rd chapter deals with the development of a novel 2D-positional mapping technique for the swift microstructural characterization of the large area oriented thin-films aiming towards the fast optimization of experimental parameters. With this mapping technique, position-dependent polarized absorption spectra were measured at varying locations utilizing the aligned light source and multichannel photonic analyzer and XY motion-controlled mobile sample stage. The sample was scanned along multiple lines to probe changes in the absorption spectra leading to the swift analysis of the uniformity and microstructural distribution. The validity of results pertaining to the thin film uniformity and molecular orientation was successfully demonstrated using FTM fabricated thin films of PQT-C12 using the mapping system and

conventional spectrophotometer. At the same time, the usefulness of this method verified using thin films of PBTTT-C14 as conjugated polymer prepared by different methods such as spin coating, friction transfer method, and FTM having different thickness range and their uniformity.

Chapter 4 deals with the investigation on the effect of the interface and the thin-film morphology on in-plane and out-of-plane charge transport. To analyze the effects on vertical charge transport, organic Schottky diodes (OSDs) were fabricated with varying metal/SCP interfaces and morphology utilizing different thin-film fabrication techniques. A new generalized model was proposed for the analysis of charge transport and extraction of the device parameters. In-plane charge transport was studied by fabricating organic field transistors (OFETs). In general, the thin film fabrication method using sheer forces, leads to face-on orientation of the macromolecules, which are although good for vertical devices but not suitable for the planer devices like OFETs. Results of in-plane GIXD and out-of-plane XRD of as-cast and annealed films of friction transferred PBTTT on HMDS treated substrate revealed the almost complete transformations from the face-on to edge-on after annealing the thin-films at about 200 °C, which was further verified by enhanced OFET mobility. Results on the temperature and interface dependent electrical and optical characterization of OFETs utilizing friction transferred PBTTT thin-films led to the proposal of a new carrier-transport mechanism to interpret the obtained experimental results.

In chapter 5, efforts were directed towards the development of the large area and environmentally benign thin film fabrication and their improvisation followed by their utilization to fabricate OEDs like OSDs, OFETs, and organic memristors. Fabrication of large area and highly oriented thin films of PBTTT was demonstrated by improvised friction transfer technique. Improvisation of the friction transfer method was done utilizing very small of the hydrophobic solvent between the polymeric pellet and the substrate. This resulted in to not only the uniform large area thin films but also the change of molecular conformation from conventional face-on to edge-on leading to highly pronounced charge carrier mobility from 0.035 cm^2/Vs to 0.4 cm^2/Vs. Subsequent optical characterization of the thin film revealed a highly extended polymer backbone, which was evidenced from in-plane grazing-incidence X-ray diffraction pattern. Further facile in-plane charge transport was demonstrated by fabricating OFETs, which consequently shown significant enhancement in the charge carrier mobility.

Finally, chapter 6 of this thesis presents the overall conclusion of the whole work summarizing the main results along with future scopes of the work and their perspectives.

Table of Contents

Chapter 1: Introduction

1.1 Research Background

Modern days and recent past have observed a huge advancement of technology and for them, the fast electronic devices in terms of carrier transport, sensing, transducing, etc. is an essential element. However, to fulfill the further desire for ultrafast technology, a lot of development is still required. Presently a significant amount of the research in this area is dedicated towards the fabrication of devices that are of low cost, light weight, power efficient, environmentally sustainable. Apart from these, the portable and wearable electronics also triggered significant research interest towards miniaturization and fabricating flexible devices, which is also an essential component in our lives.

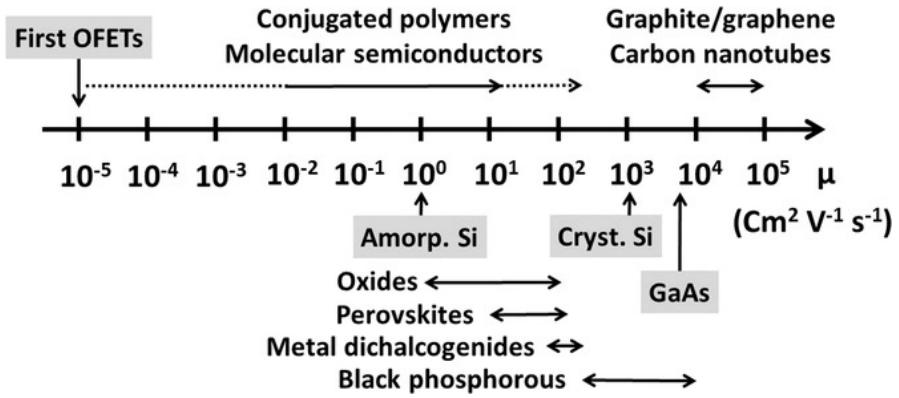

Figure 1.1 Comparative range of charge carrier mobility for various semiconducting materials. Reproduced with Permission,[1] Copyright 2020 WILEY-VCH.

For the last two centuries, immense scientific research and development interest have been focused on the advancement of various inorganic semiconducting materials, and largely silicon-based material remained an optimal choice owing to its unique characteristics. However, facilities required for the production of high purity silicon (crystalline) wafer consists of many sophisticated,

expensive, complex, and energy consuming processes. Moreover, purifying the raw-material is also a challenging task in order to decrease the terminal cost. Besides, high-class clean room is inevitable for research and development or fabrication of the devices. The processing could be decreased, by minimizing the need for sophisticated facilities. Nevertheless, organic semiconductors, in which charge transport occurs through π-electron cloud, are more advantageous because of their low-cost handling as well as easy tuning of physical properties through chemical structure engineering. Although the transport characteristics of an organic electronic device (OED) cannot match with that of crystalline silicon-based devices especially the single crystal based, it is certainly not an essential requisite instead the aim of the development of the field of organic electronics is to complement the existing inorganic semiconductor based electronics.

Though the electrical characteristics of amorphous-Si in terms of charge carrier mobility significantly lag behind singlecrystalline-Si (as described in **Figure 1.1**)[1], presently amorphous Si is the key material for flexible electronic devices such as radio frequency identification tags, backplane circuitry in display technology, etc. So far the amorphous-Si based thin-films are deposited through chemical vapor deposition technique. In the meantime, umpteen amount of advancements have been recorded in the field of inorganic semiconductors[1,2]. However, irrespective of these developments, it is a long way to go to realize the low-cost, large scale flexible circuits with inorganic semiconductors, for instance, the fabrication processes needs to be decreased. In this regard, organic-inorganic hybrid devices can be a better alternative. For example, the overall cost can be reduced by mass fabrication of printed flexible organic based displays for which the high-speed carrier transport is not required; however, the speed of the device can still be retained by interfacing it with the inorganic semiconductor based high speed processors.

Table 1.1 Comparison chart for printed electronics versus Conventional Electronics

Printed Electronics	Conventional Electronics
Less expensive	High manufacturing costs
Simple process	Complex process
Compatible with flexible substrate	Compatible with rigid substrates
Large area fabrication is feasible	Commonly wafer scale fabrication
Small integration density	Extremely high integration density
High switching times	Switching times very small

Regarding above discussed challenges, the organic semiconducting materials primarily semiconducting polymers (SPs) have many advantageous properties that can be exploited to producing cost-efficient portable and wearable electronic devices (**Table 1.1**). These can be more understandable by analyzing by the scientific and developments demonstrated/achieved in the field of organic electronics and polymer science, to match with the electrical performance amorphous-Si based applications[3]. Mainly the organic semiconductors are more preferable in comparison to amorphous-Si due to the following reasons: i) their synthesis can be conducted in ambient conditions, ii) according to desired applications their optoelectronic properties can be varied by simple chemical structural modifications, iii) their thin-films can be fabricated using many cost-efficient solution processes, iii) the devices can be fabricated under ambient conditions, etc.[4] As discussed the hybrid organic-inorganic device can be more cost-efficient without compromising the electrical performance in comparison to only inorganic semiconductor based electronic devices. Therefore, it can be stated that the actual aim of the development of the organic semiconductor based devices is not at all to match the electrical characteristics of the singlecrystalline-Si based devices, instead they can be a suitable candidate to substitute the applications of amorphous-Si. Apart from this the unique, as well as tunable optoelectronic properties of the organic semiconducting materials, can also be utilized in much more worthwhile applications[5,6]. Some recent applications of organic semiconductors based typical electronic devices are shown in **Figure 1.2**.

Figure 1.2 Digital image of some organic electronic devices (a) the foldable FlexPai smartphone/tablet[7]; (b) flexible organic solar cell[8]; (c) wearable smartphones[9]; (d) Flexible TV (source: FlexEnable)[10].

Especially amongst organic semiconductors, SPs offer many benefits compared to small molecular organic semiconductors and some key advantages are their better solution processability and flexibility. Further, due to their quasi-one-dimensional nature transport properties of conjugated polymer based devices stringently depends on their average molecular weight as well as molecular structure, the thin-film morphology, the interfacial properties, and also the device structure. There are various reports which presented the comparative studies on these aspects[11–14]. The role of crystallinity and backbone orientation as well as its conformation in the polymer thin film is crucial for charge transport. In this thesis work, efforts were given to study their effect on the planer and vertical charge transport. Further, a new film fabrication technique was also developed to overcome the challenges in the existing orientation techniques. Furthermore, fabrication of organic electronic devices in layer-by-layer coating of solution processed polymer thin films was also demonstrated. Hence by considering all the sections of this thesis work it focuses on the environmentally sustainable fabrication of cost-efficient compact organic electronic devices which can address many existing challenges towards next-generation printed organic electronic devices.

1.2 Charge Transport in Semiconducting Polymers

Polymers can be defined as a substance having a molecular structure which mainly consists of a large number of repeat units, called monomers, bonded together. Generally, the carbon atoms joining the monomers are hybridized in sp^3 structure and connected through four σ-bonds with adjacent atoms. However, these σ-bonds do not offer any electrical conductivity to the polymers. Such polymers are insulators and widely used as dielectric materials in electronic devices and many other insulating or packaging applications. On the other hand, adjoining carbon atoms in semiconducting conjugated polymers' backbone are sp^2 hybridized having one π-bond. The alternate arrangement of single and double bonds across the conjugated polymers' backbone leads to the overlapping of p_z orbitals get overlapped and shared electrons are delocalized in order to lower their overall energy and increase. Moreover, lone pairs may also be part of the delocalized electron system. This is also termed as delocalized electron cloud which possesses high density of states and is responsible for charge transport. The chemical structures of some typical conjugated polymers are shown in **Figure 1.3**.

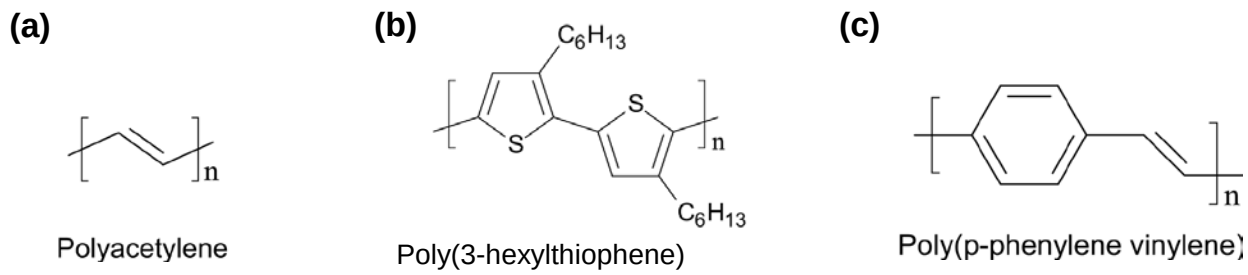

Figure 1.3 Molecular structure of some typical semiconducting polymers.

In the pristine or ideal intrinsic state, there are no free charge carriers in the conjugated polymers. The charge carriers are introduced through partial reduction or oxidation which consequently leas

to the generation of n-type carriers or p-type carriers respectively. The extrinsically generated carriers introduce charged defects like polarons, bipolarons, and solitons[15]. In terms of band theory, the concept of doping induced carrier transport can be understood from the perusal of **Figure 1.4**. Similar to the concepts of inorganic materials, the highest occupied band in conjugated polymers is called the valence band (VB) and the lowest unoccupied band is called the conduction band (CB). While the highest occupied molecular orbital (HOMO) and lowest unoccupied molecular orbital (LUMO) corresponds to the top edge of VB and bottom edge of CB respectively. The charge carrier needs a specific quantity of energy to move from the VB to the CB[15,16]. Therefore, the energy gap between the HOMO and LUMO levels is termed as bandgap (EG) which is responsible for the optoelectronic nature of the material i.e., conducting, semiconducting, or insulating as well as the color of the corresponding thin film. In metals, CB is partially overlapped with VB (EG = 0) and the electrons in the VB face no barrier to go to CB and become electrically conductive. In the case of conjugated polymers, a narrow gap exists between VB and CB (EG ≠ 0), and by various types of doping their band structure is further changed.

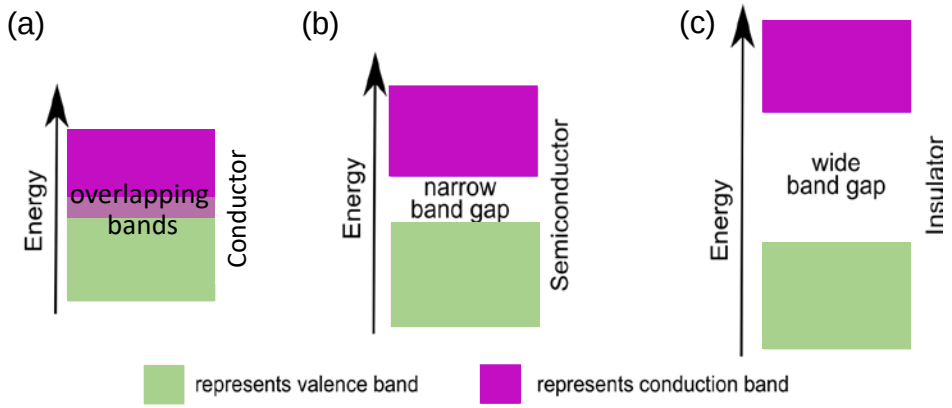

Figure 1.4 Schematic illustration for the bandgaps in (a) conductor, (b) semiconductor, and (c) insulator.

When an electron is being inserted into the LUMO (or taken out from HOMO) of a semiconducting polymer, the corresponding CB (or VB) becomes partially filled and the resulting

radical anion (or cation), is called polaron[17]. The polaron can possess both types of charges. Injection of a secondary electron to a conjugated polymer chain which already possessed a negative polaron leads to bipolaron formation and a similar concept is true for the positive bipolaron formation[17].

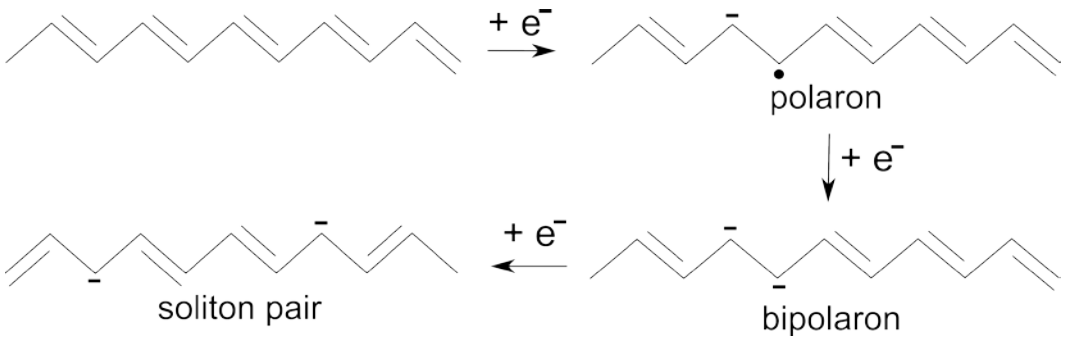

Figure 1.5. Schematic representation for the polaron, bipolaron, and soliton pair formation due to external doping on a polyacetylene backbone.

Doping in conjugated polymers can primarily be categorized into four types based on its method, discussed as follows:

Chemical-doping: SPs can either be partially reduced or oxidized by exposing them to a suitable by e^--donating e^--accepting or dopant material respectively which consequently lead to the formation of charge carriers[18].

Electrochemical-doping: In electrochemical processes, SPs, possessing a large amount of π-electron cloud, can be typically utilized as source/sink for the flowing electrons which further lead to their desired doping p-type/n-type respectively[19].

Photo-doping: By irradiating the SPs using photons of sufficient energy (> EG of the SP) the electrons present in the VB are promoted to CB leading to the formation of mobile charge carriers[20].

Charge injection-doping: The mobile carriers can be accumulated in the SP film by applying a specific amount of potential to the metal/insulator/SP multilayered structure[21].

1.3 Basics of Organic Electronic Devices

1.3.1 Importance of Orientation in Semiconducting Polymer Films

The over-performance of an organic electronic device is highly influenced by the thin film morphology.[22,23] Since the SPs possess quasi-1-dimensional structure, the charge carrier transport is improved when the polymer backbones are unidirectional oriented in the thin film, as shown in **Figure 1.6**. Since the π-electron cloud is more delocalized along the backbone, therefore, charge carriers are more mobile along the backbone orientation direction[24]. Further along the intermolecular p-p-stacking, the charge carrier mobility is lower than that along the backbone orientation direction but higher than that along the alkyl side chain direction. The alkyl side chains are attached to the polymer backbone to make it soluble in common organic solvents. Since the side chains do not possess conjugated π-bonds and corresponding π-electron cloud, they act as an insulator and the carrier mobility is least along the side chains. Hence, the backbone orientation also leads to anisotropic charge transport in the polymer thin film.

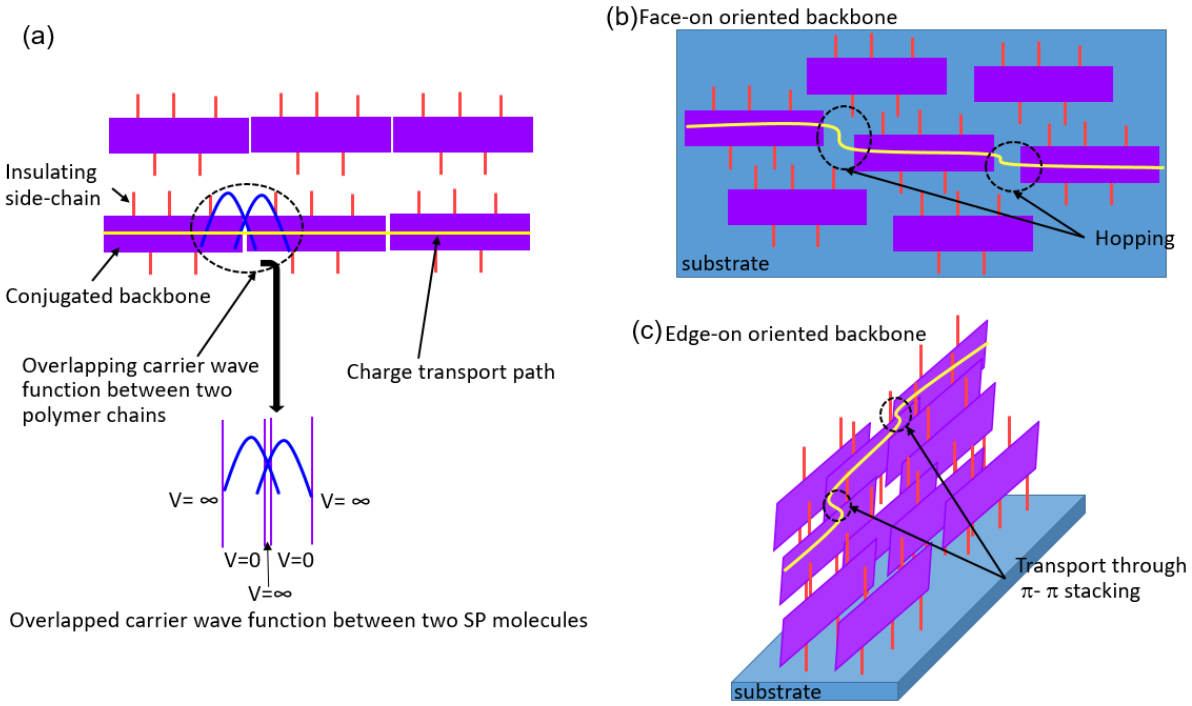

Figure 1.6 Schematic Representation for carrier transport mechanism along ideally the oriented polymer backbones (a). Schematic illustration for Face-on (b) and Edge-on (c) macromolecular conformation on the substrate.

The backbone conformation is also important in the overall charge transport. Depending on the relative arrangement of the polymer backbone with respect to the substrate plane, the conformation is cauterized in three types: face-on, edge-on, and end-on. In edge-on conformation, the alkyl chains lie along the substrate normal whereas the conjugated backbone and the π-π-stacking lie in the substrate plane. In the face-on conformation, the polymer-backbone and the alkyl side chain lies in the plane of the substrate while the p-p-stacking lies along the substrate normal. In the end-on conformation the conjugated backbone lies along the substrate normal whereas the π-π-stacking and the side chains lie in the plane of the substrate[25]. Since the ideal backbone cannot be attained in the polymer thin film, therefore, optimum carrier transport characteristics are attained when the conjugated-backbone and the π-π-stacking are kept in the plane of the transport. Hence, for efficient vertical charge transport (for example in organic solar cells, organic Schottky diodes,

organic light emitting diodes, etc.) end-on conformation would be preferred; however, attaining this conformation is quite difficult for common conjugated polymers. Therefore, for optimum vertical charge transport face-on macromolecular conformation is preferred[26,27]. On the other hand, for high in-plane charge transport (for example in organic field effect transistors, OFETs), the edge-on conformation is preferred; however, the charge transport anisotropy is high in the case of face-on conformation due to insulating nature of the alkyl side chains[28].

There are various orientation techniques which lead to varying macromolecular conformation in the polymer thin film. Generally, the solution processes (such as solution shearing[29], off-center spin coating[11], directional solvent evaporation on nanostructured substrates[11,30], etc.) lead to edge-on conformation because which is more thermodynamically stable, and in the presence of solvent, the polymer backbones get sufficient freedom to attain this state. Further, the orientation techniques in which mechanical force is applied on the polymer backbones, lead to face-on macromolecular conformation. However, there are reports regarding the face-on to edge-on transition after high temperature annealing of the polymer thin films. Furthermore depending on the interaction between the orienting substrate and the polymer backbones any of the three conformations is plausible in this category few techniques are as follows floating-film transfer technique[11,31], directional epitaxial crystallization[24,32], and dynamic-template-directed orientation[33], end-on orientation by surface segregation[25].

The orientation characteristics in the polymer thin films are quantitatively characterized through polarized UV-Vis-NIR absorption spectrophotometer, polarized Raman spectrophotometer, etc. However, the qualitative orientation characteristics i.e. backbone orientation along with macromolecular conformation and thin-film crystallinity is characterized

through more sophisticated techniques like electron diffraction measurements and grazing incidence X-ray diffraction measurements, etc.

1.3.2 Types and Effects of Interfaces in Organic Electronic Devices

The electrical characteristics of the conjugated polymer-based devices are sensitive to the morphology of the bulk of the semiconductor layer as well as the interface quality. Since organic electronic devices are generally fabricated by depositing layers of conducting, semiconducting, and/or dielectric layers, therefore, their transport and other characteristics can be controlled through proper understanding and optimization of the interfaces. Depending on the type of involved layers, interfaces can be divided into three categories such as i) conductor/semiconductor (conductor/SC) interface which mainly influence the charge injection to and extraction from the organic thin films, ii) semiconductor/semiconductor (SC/SC) interfaces present in layer-by-layer[34] structures, and iii) semiconductor/dielectric (SC/dielectric) interfaces mainly present in planar device structures[11]. Although interfaces can be of various kinds, their primary involvement can be understood in terms of charge trapping [35–37]. Near the interfaces, the availability of density of states due to chemical impurities, hamper the desired carrier transport. Especially in the planer device structure, the semiconductor to dielectric interface plays a crucial role. In the ON state of OFETs few molecular layers near the interface are responsible for carrier transport, and as extensively reported the thin film morphology near the dielectric interface is affected by the interaction between the organic semiconductor and chemical groups present at the interface, therefore the near interface macromolecular disorder may be detrimental to the overall carrier transport [38,39]. The energy band mismatch at the electrode/semiconductor interface also affects the charge injection and extraction which can be optimized by proper selection of materials and/or by depositing interfacial layer [40,41]. As discussed the effective resistance encountered at the conductor/SC interface, termed as contact

resistance, can be optimized by varying the type of electrode, an organic semiconductor, as well as by an interfacial-layer between them in some cases; nevertheless, the traps present at the interface play a crucial role in overall contact resistance[42–46]. As demonstrated by Tsukagoshi and coworkers, regardless of copper's lesser work function which leads to a larger barrier for hole injection at copper-pentacene contact, yet the effective contact resistance of pentacene based OFET, with copper as the top source and drain electrodes, was lower compared to the contact resistance in case of gold electrodes[43]. Further, it can be argued that in the field effect transistors, if there is a barrier for injecting holes through one electrode in such case there must be no barrier for extracting holes from the other electrode where the metal/organic interface at both the contacts possess a similar band structure. Since the estimated magnitude of contact resistance at both contacts was approximately similar, therefore, it can be speculated that the presence of traps at the interface significantly influenced the overall contact resistance[44]. Therefore to understand the transport properties of the organic electronic devices, exhaustive analysis of the effect of thin-film morphology and interfaces is crucial.

1.3.3 Planar Devices Structure: Organic Field Effect Transistor

Owing to the uncanny development of the technology, the field elect transistors have become an essential part of our lives. From simple switches to mobile phones or complicated supercomputers, their basic building block is the field effect transistor. In general concept of field effect can be understood as tuning the effective resistance of a semiconductor layer by applying and varying the electric field orthogonal to the plane of the film[47]. Similar to the capacitive operation in which the dielectric layer is placed between two conducting layers, the field effect transistor is fabricated by keeping the dielectric layer between the active semiconductor layer and the gate electrode. Further, depending on the applied potential at the gate electrode, charge carriers

are accumulated at the gate electrode and consequently, opposite charge carriers are accumulated in the semiconductor layer (near dielectric interface), similar to the charge accumulation in the capacitors. The type and magnitude of the accumulated charge is responsible for the variation of the overall resistance of the semiconductor layer near the dielectric interface, which precisely depends on the magnitude and direction of field applied between the gate and the semiconductor layers. The organic field effect transistors (commonly termed as OFETs) are a category of field effect transistors in which the organic semiconductors are utilized for fabricating the active semiconducting layer, as schematically shown in **Figure 1.7**. A typical OFET consists of three electrodes (also termed as terminals: source, drain, and gate) along with an organic semiconducting layer and a dielectric layer. Although for flexile organic circuits, all the constituent materials of the OFETs would by of flexible nature and there are various options in this regard as well as huge scientific effort is dedicated to developing such materials, due to ease of fabrication generally highly-doped Si (acting as a gate electrode) substrate with thermally grown SiO_2 at the top (acting as dielectric) is utilized to demonstrate research and development in OFETs[48].

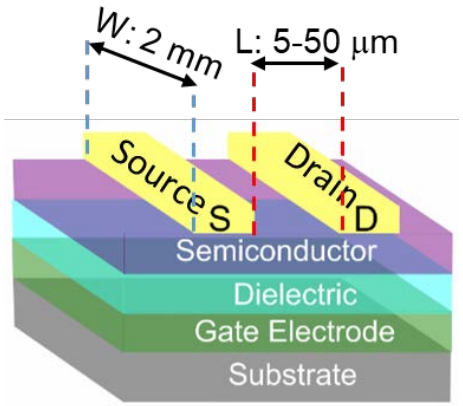

Figure 1.7 Schematic diagram of organic field effect transistor.

Following the above discussion, a dielectric layer is kept between the active layer and the gate electrode, and two electrodes (source and drain) are patterned such that there is some gap between them which is termed as the OFET's channel. Moreover, the source and drain electrodes are in contact with the active semiconducting layer, and responsible for charge injection and extraction. The width of the source and drain electrodes corresponds to channel width (*W*) whereas the gap between them is defined as the channel length (*L*). Theses OFET parameters are crucial for its transport characteristics. Depending on the fabrication flow, the OFET architecture is varied and it can be categorized mainly in four types i) Bottom gate top contact OFET, ii) Bottom gate bottom contact OFET, iii)top gate bottom contact, and iii) top gate bottom contact OFET, as shown in **Figure 1.8**. The OFET architecture also affects its optoelectronic properties and can be optimized by varying and the device architecture and comparing their transport properties.

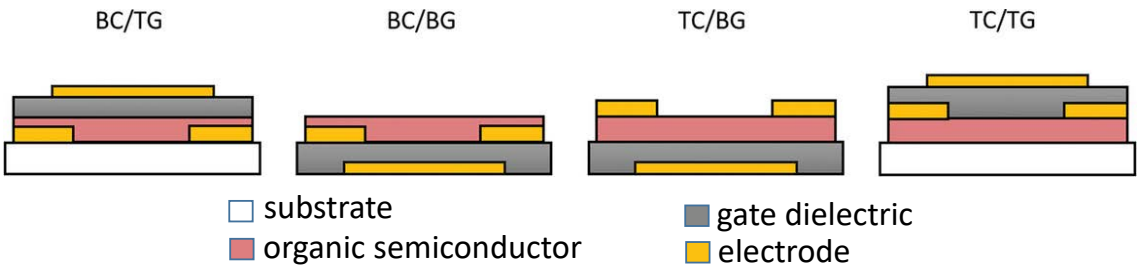

Figure 1.8 Schematic illustration for different architectures of OFET. From left to right, bottom contact top gate (BC/TG), bottom contact bottom gate (BC/BG), top contact bottom gate (TC/BG), and top contact top gate (TC/TG). Reproduced with Permission,[1] Copyright 2020 WILEY-VCH.

In deciding the OFET's electrical characteristics, the dimension and morphology of the dielectric layer are also key parameters apart from the OFET architecture and the channel dimension. The thickness and dielectric constant of the dielectric layer are responsible for the extent of charge accumulation in the semiconducting layer. Therefore depending on the desired

operating voltage (gate voltage) for any circuit element (OFET), the thickness and material for the dielectric layer can be optimized. In the recent past, many organic dielectric materials have been reported to satisfy the requirements of the operating voltage conditions of the evolving flexible organic circuits[48–51]. Their solution processability makes them a potential candidate for the cost-efficient fabrication of organic electronic devices.

To understand the operating mechanism of a typical OFET, the energy band diagram can be helpful, as shown in **Figure 1.9**. In the band diagram, the Fermi energy level (E_F) of the drain and source electrodes along with the HOMO and LUMO level of the organic semiconducting material is drawn side by side, following the OFET's in-plane structure. The energy band diagram provides the basic concept regarding the type of carrier transport in the film and the contact resistance. In the pristine form, the organic semiconductors do not possess any mobile charge carrier but the type of electrode as well as the applied gate voltage decides the type of carrier transport through a specific organic material. Therefore, depending on the HOMO/LUMO level of the organic semiconductor, an appropriate source, and drain electrode can support or hinder the specific type of carrier transport.

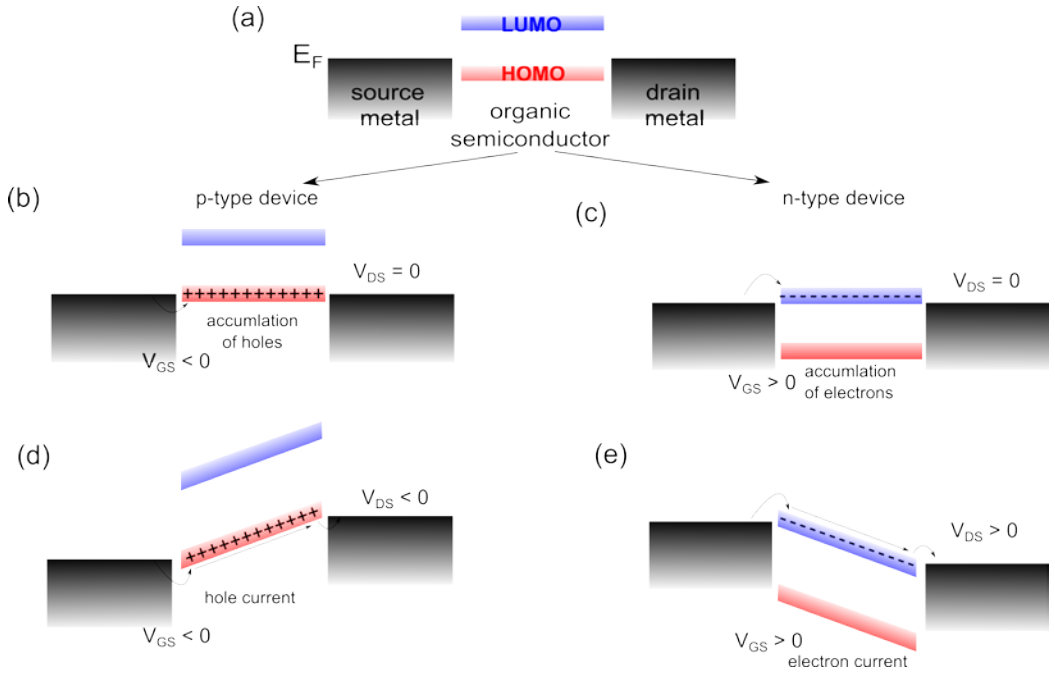

Figure 1.9 Schematic representation for the band diagram of OFETs.

Operating Mechanism: By applying a negative gate bias (V_{GS}) the positive charge carriers are accumulated in the organic semiconductor layer (near its dielectric interface) and the Fermi energy level of the source and drain electrode moves towards HOMO the organic semiconductor (p-type). A similar mechanism also occurs for the n-type organic semiconductor when the positive gate bias is applied, as shown in **Figure 1.9**. The accumulated charge carriers provide an electrically continuous path with higher conductivity compared to unbiased conditions. Further, by applying the appropriate electric field across the channel (i.e. by biasing the source and the drain electrodes), charge carriers are transported which is called ON state of the transistor, as depicted in **Figure 1.9**(c and d).

Analysis of OFET's Electrical Performance: Following the previous discussion, OFET can be compared to a capacitor, in which opposite charge carriers are accumulated in the organic

semiconductor layer. The amount of the charge carrier accumulation (here considering the carrier density as '*n*') can be easily tuned by varying the gate bias.

Average applied bias at a distance *x* can be equated to the difference of average channel potential with respect to the gate potential acting on the other side of the dielectric layer. Further, total charge carrier density at a distance x is $Q_T(x)$ on a capacitor plate is given by the following equation:

$$Q(x) = (V_{GS} - V(x) - V_{TH})\, C_i \tag{1.1}$$

Here C_i is the capacitance per unit area of the dielectric layer and $V(x)$ is the voltage at distance x.

Considering drift current density (J) in the channel is governed by Ohm's law, which is a product of the electrical conductivity (σ) and electric field (E) and can be expressed as follows:

$$J = \sigma\, E \tag{1.2}$$

Since σ is the product of unit charge (q), charge carrier density (n), and carrier mobility (μ), then Eq. 1.2 can be written as Eq. 1.3.

$$J = qn\mu E \tag{1.3}$$

Substituting $E = -\frac{dV}{dx}$, $qn(x) = Q(x) = (V_{GS} - V(x) - V_{TH})\, C_i$ in Eq. (1.3) with neglecting the negative sign, Eq. 1.3 can be written as Eq. 1.4.

$$J = (V_{GS} - V(x) - V_{TH})\, C_i \mu \frac{dV}{dx} \tag{1.4}$$

Eq. (1.4) can also be written as Eq. (1.5)

$$Jdx = C_i\mu(V_{GS} - V(x) - V_{TH})\, dV \tag{1.5}$$

Here J is constant. Further, integrating Eq. (1.5) from source to drain i.e. along the channel length (L) ($x = 0$ to $x = L$).

$$J\int_0^L dx = C_i\mu \int_{V(0)}^{V(L)} (V_{GS} - V(x) - V_{TH})\, dV \tag{1.6}$$

Since $V(0) = 0$ and $V(L) = V_{DS}$, on solving the Eq. (1.6), we get Eq. (1.7).

$$J = \frac{C_i\mu}{L}(V_{GS} - V_{TH})V_{DS} - \frac{{V_{DS}}^2}{2} \tag{1.7}$$

Upon substituting $J = I_{DS}W$, it must be noted that J for the channel is A/cm since $Q(x) = charge/cm^2$

$$I_{DS} = \frac{C_i\mu W}{L}(V_{GS} - V_{TH})V_{DS} - \frac{{V_{DS}}^2}{2} \tag{1.8}$$

Here Eq. (8) is valid under two assumptions: i) transverse electric field in the channel induced by V_{GS} is much larger than the field along the channel due to V_{DS}, and ii) the mobility is constant all over the channel. The first assumption is also called Shockley's gradual channel approximation of junction field effect transistor.[52] The validity of this approximation holds true if the thickness of the dielectric is too less than the channel length.

Since in linear region $V_{DS} \ll (V_{GS} - V_{TH})$ and $\frac{{V_{DS}}^2}{2}$ in the Eq. (1.8) will be very small, therefore, it can be neglected and I_{DS} in linear region (I_{DS}^{lin}) can be simplified as Eq. (1.9).

$$I_{DS}^{lin} = \frac{C_i \mu W}{L} (V_{GS} - V_{TH}) V_{DS} \tag{1.9}$$

Similarly in saturation where $V_{DS} \geq (V_{GS} - V_{TH})$, the I_{DS} in the saturation region (I_{DS}^{sat}) can thus be described by Eq. (1.10).

$$I_{DS}^{sat} = \frac{C_i \mu W}{2L} (V_{GS} - V_{TH})^2 \tag{1.10}$$

1.3.4 Basics of Organic Schottky diode a Vertical Device Structure

Among the organic electronic devices having vertical charge transport, the organic Schottky diode the most basic device structure. It this device structure the desired organic semiconducting active layer is sandwiched between two electrodes. One of the electrodes makes Ohmic contact with the active thin film while the other makes Schottky contact. The energy band diagram of a typical Schottky contact and the Ohmic contact at the electrode-semiconductor interface is shown in **Figure 1.10**. The selection of the electrode and the semiconductor materials significantly

influences the overall device performance. During the formation of electrode-semiconductor junction, the charge carriers move from one to other depending on their energy levels, such that the electrode's work function could match with the fermi-level of the semiconductor. The transfer of the charge carrier also leads to band bending. When the magnitude of the p-type semiconductor's fermi level is higher than the electrode's work-function, effectively the positive charge carriers are transferred from the semiconductor to the metal and Schottky barrier is formed at the junction with the barrier height of Φ_B, as shown in **Figure 1.10** (a). On the other hand, if the magnitude of p-type semiconductor's fermi level is smaller than the electrode's work-function, effectively the positive charge carriers are transferred from the electrode to the semiconductor layer leading to the formation of an Ohmic contact, and in this, the barrier height is negligible as shown in **Figure 1.10** (b). Although this concept is appropriate for inorganic semiconductors, slight improvisations are desired for organic semiconductors because the organic semiconductors possess a comparatively larger energy gap (typically >2 eV) and carrier density is also low which can be excited by the thermal energy. a small number of free charge carriers are thermally excited. Apart from this, the trend of band bending in the organic diodes is also quite different from the conventional inorganic diodes These concepts have been discussed in more detail in Chapter 4.

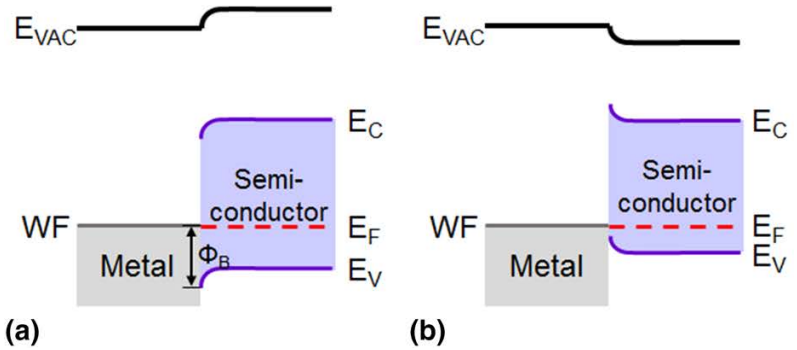

Figure 1.10 Energy level alignment at the metal/semiconductor contact for (a) the Schottky contact and (b) ohmic contact[53]. Reproduced with Permission, Copyright Materials Research Society 2017

1.4 Existing Problems and Research Motivation

Semiconducting polymers (SPs), due to their excellent optical, electrical, and mechanical properties, have gained huge scientific interest in fabricating efficient flexible electronics. Fabrication of Organic Electronic devices (OEDs) involve deposition and processing of various semiconducting, conducting, and/or layers dielectrics. Thus the overall electrical performance of an OED depends on individual thin-film morphology and the interface between them. Therefore, the corresponding optimization is essential to attain the desired OEDs performance. Charge transport in SPs thin-films occurs along the π-conjugated backbone, through π-π stacking between adjacent conjugated backbones, and intermolecular as well as interdomain hopping. Moreover, hopping assisted intramolecular charge transport also takes place at discontinuous π-conjugation present in folded and twisted SP chains. In recent past huge efforts of various research groups have been dedicated to improving the crystallinity of SP thin-films by chemical structure engineering, developing various thin-film fabrication techniques, and post-processing of the thin films aiming towards enhancement in transport characteristics of OEDs. Our group has also developed a novel technique, called floating-film transfer method (FTM), for oriented SP film fabrication at the atmosphere-liquid interface through which multilayered coating is also possible without damaging underlying layers. Further, there are reports regarding SP/dielectric and SP/metal interfaces, still comprehensive experimental investigations as well as theoretical analysis are required for clear understanding and enhancement in OEDs' transport characteristics.

Further, the environment and health related challenges of organic electronics is also a big issue to be addressed before its mass fabrication. Regarding large scale applications, inexpensive fabrication of polymer-based OEDs has been demonstrated with solution-based printing technique[11,54,55]. The vapor of halogenated solvents, which is commonly utilized in conjugated polymer thin film fabrication, can lead to serious health and environment hazard[56]. Therefore

efficient utilization or modification in existing techniques, as well as invention of new techniques, are highly desired to reduce or substitute the presently inevitable need of halogenated solvents in organic electronics.

After scrutinizing current state-of-art three of the major challenges were focused on towards large sale fabrication of sustainable organic electronics with controlled charge transport. In this thesis work some of the well-known SPs such as regioregular poly(3-hexylthiophene) (P3HT), poly[2,5-bis(3-tetradecylthiophen-2-yl)thieno[3,2-b]thiophene] (PBTTT), poly(3,3‴-didodecyl-quarterthiophene) (PQT), were utilized for thin-film fabrication through spin-coating, drop-casting, FTM, and friction transfer techniques and they characterized were carried out through polarized absorption spectroscopy, polarized Raman spectroscopy, interference microscope, X-ray diffraction, grazing incidence X-ray diffraction, and atomic force microscopy. To investigate the effect of thin-film morphology on their transport characteristics, their electrical measurements were conducted by fabricating thin-film transistors, Schottky diodes, and memristors. The device dimension and architectures were also varied to attain optimum electrical performance of OEDs.

In order to accomplish the aim of efficient fabrication and commercialization of organic electronics, certainly, there is a need for the development of efficient device fabrication technology aiming towards,

1. Cost-efficient
2. Large area thin film fabrication and swift characterization for efficient optimization of film morphology
3. Capable of increasing orientation and crystallinity of the films
4. Freedom of film's thickness and morphology tuning
5. Minimum material wastage

6. Environmentally sustainable system
7. Uncomplicated processes with simple instrument and ease of handling
8. Development of analytical/characterization techniques for efficient utilization of existing technology and further development.

As discussed various techniques have been reported for improving the crystallinity of the thin films and many of them, like FTM, friction transfer, solution-shearing, etc., lead to the inexpensive fabrication of large-area SP thin film. Corresponding thin film morphology, an implicit function of various casting parameters, can be optimized through a series of film fabrication by tuning the parameters and comparing their characteristics. Besides, position-dependent morphological variation is another big issue with large area SP thin films. There are many sophisticated techniques, atomic force microscopy, X-ray diffraction, near-edge x-ray absorption fine structure spectroscopy, variable angle spectroscopic ellipsometry, etc., through which precise microstructural characterization of SP thin films is performed but they are not suitable for swift characterization of large-area thin films (of several cm^2). 2D-positional mapping technique was developed for swift microstructural characterization of thin-films and fast optimization of experimental parameters resulting in charge transport uniformity at large-scale. With this mapping technique, position-dependent absorption spectra were measured at varying locations through the aligned light source and multichannel detector and by the controlled movement of the sample stage. The sample was scanned along multiple lines by comparing the intensity, broadening, and shifts of absorption spectra a map of microstructural distribution throughout the thin film was realized.

Further, as transport characteristics of OEDs primarily depend on the thin film morphology and the interfacial qualities, therefore, the effect of the interface and the thin-film morphology on in-plane and out-of-plane charge transport were studied. To analyze the effects on vertical charge transport, Organic Schottky diodes were fabricated with varying metal/SP interfaces, and the

morphology of the SP film was also varied by opting different casting techniques. An extensive transport model was also developed for calculation and comparative analysis of their transport parameters. In-plane charge transport was studied by fabricating organic field transistors, in bottom-gated top contact device architecture on bare and self-assembled mono-layer treated substrates (Si/SiO_2). On annealing, conformational changes in the thin film were observed which also varied depending on the substrates' surface energy. Consecutive effect on in-plane charge transport was also recorded and to interpret a pertinent carrier-transport mechanism was proposed in light of the obtained results from temperature and interface dependent electrical and optical characterization of the friction transferred PBTTT thin-films. Further efforts were also dedicated towards environmentally sustainable large scale fabrication of OEDs. In this regard, a new film fabrication technique was also developed which interestingly provided significant improvement in film crystallinity and in-plane charge transport.

1.5 Organization of the Thesis

Chapter 1 introduces the concerns related to the present state-of-art in organic electronics, problems related to thin-film fabrication techniques for SPs, the need for comprehensive understanding pertaining to the SP/dielectric, and SP/metal interfaces and their implication on the charge carrier transport. The theory of electrical conduction in SPs, their charge carriers, energy band as well as charge carrier transport, with existing thin-film fabrication techniques has been discussed in detail followed by challenges currently being faced and justification about the aim of the present research work conducted.

In chapter 2, a brief outline of the SPs like P3HT, PBTTT, PQT utilized in the present thesis, their thin-film processing adopting spin-coating, drop-casting, floating film transfer, and friction

transfer techniques. Various techniques used not only for the characterization and analysis of the oriented thin films but also for fabrication and analysis of various organic electronic devices have been discussed in detail.

3rd chapter deals with the development of a novel 2D-positional mapping technique for the swift microstructural characterization of the large area oriented thin-films and fast optimization of experimental parameters resulting in charge transport uniformity. With this mapping technique, position-dependent polarized absorption spectra were measured at varying locations utilizing the aligned light source and multichannel photonic analyzer along with the XY motion-controlled mobile sample stage. The sample was scanned along multiple lines by comparing the intensity, broadening, and shifts of absorption spectra to map the uniformity and microstructural distribution throughout the thin films.

Chapter 4 deals with the investigation on the effect of the interface and the thin-film morphology on in-plane and out-of-plane charge transport. To analyze the effects on vertical charge transport, organic Schottky diodes (OSDs) were fabricated with varying metal/SP interfaces and morphology of the SP films utilizing different thin-film fabrication techniques. A new generalized model was proposed for the analysis of charge transport and extraction of the device parameters. In-plane charge transport was studied by fabricating organic field transistors (OFETs). Results on the temperature and interface dependent electrical and optical characterization of OFETs utilizing friction transferred PBTTT thin-films led to the proposal of a pertinent carrier-transport mechanism to interpret the results pertaining to the implications of the conformational changes owing to the change in the substrates' surface energy and annealing temperature.

In chapter 5, efforts were directed towards the development of the large area and environmentally benign thin film fabrication and their improvisation followed by their utilization to fabricate OEDs like OSDs, OFETs, and organic memristors. Fabrication of large-area thin films of highly extended PBTTT chains was demonstrated improvised Friction transfer technique. Interestingly, by optimizing the casting conditions and placing a little amount of borderline solvent, oriented PBTTT thin films were drawn on low surface energy/hydrophobic substrates. Subsequent optical characterization of the thin film revealed a highly extended polymer backbone, for instance (003) peak corresponding to the polymer's repeat unit was evidenced from the in-plane grazing-incidence X-ray diffraction pattern. It is worth noting that this peak is rarely observed in this class of SPs due to unavoidable twists and folds occurred through many other casting techniques. Further facile in-plane charge transport was demonstrated by fabricating OFETs which consequently shown significant enhancement in the charge carrier mobility.

Finally, chapter 6 of this thesis presents the overall conclusion of the whole work summarizing the main results along with future work and their perspectives.

Chapter 2: Materials and Methods

2.1 Materials

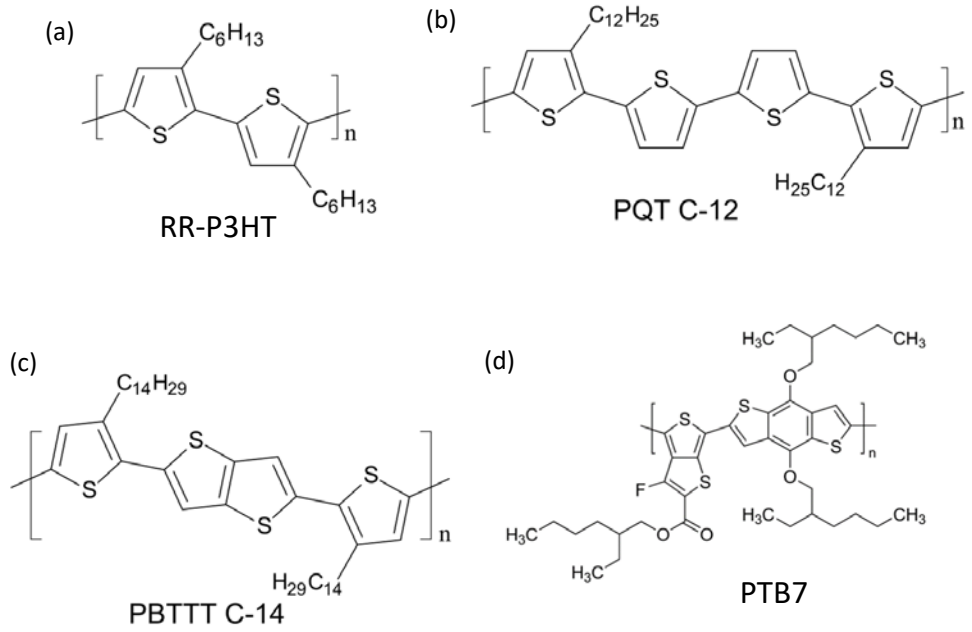

Figure 2.1 Chemical Structure of different π-conjugated semi-conducting polymer with their abbreviation used. (a) Regioregular poly(3-hexylthiophene), (b) Poly(3,3‴-didodecyl-quarterthiophene), (c) Poly[2,5-bis(3-tetradecylthiophen-2-yl)thieno[3,2-b]thiophene], (d) Poly[4,8-bis[(2-ethylhexyl)oxy] benzo [1,2-b:4,5-b']dithiophene-2,6-diyl][3-fluoro-2-[(2-ethylhexyl)carbonyl]thieno[3,4-b]thiophenediyl].

Poly(3,3‴-didodecyl-quarterthiophene) (PQT-C12) was synthesized following the repotrd method[57] . Further, after synthesis the semiconducting polymer (SPs) was purified through Soxhlet extraction technique[58,59]. Regioregular poly(3-hexylthiophene) (RR-P3HT) and poly(3,3‴-didodecyl-quarterthiophene) (PBTTT-C14) were purchased from Sigma Aldrich. Poly[4,8-bis[(2-ethylhexyl)oxy] benzo [1,2-b:4,5-b']dithiophene-2,6-diyl][3-fluoro-2-[(2-ethylhexyl)carbonyl]thieno[3,4-b]thiophenediyl] (PTB7) was supplied by from 1-Material. The chemical structure of the SPs are shown in **Figure 2.1**. Super dehydrated solvents (chloroform, chlorobenzene, 1,2-dichlorobenzene, toluene) were supplied by Sigma Aldrich.

2.2 Thin Film Fabrication Techniques

2.2.1 Spin coating technique

The most common technique to coat the laboratory scale thin film is the spin coating technique. From the initial stage of the field of organic electronics, it has been utilized for fabricating various organic thin films using organic semiconductors, dielectric materials, as well as occasionally the conducting materials also. To cast the film, at first, the desired material is dissolved in an appropriate solvent and further, the solution is placed on the substrate which was fixed on the spinning chuck of the spin-coating machine. To fix the substrate on the chuck it is connected to a vacuum pump which provides a mild vacuum, consequently, the substrate is adhered/sucked to the chuck. The digital image of the laboratory spin-coater along with the coating mechanism is shown in **Figure 2.2.** The spin speed and the time of spinning can be varied according to the requirement and the can be manually set in the operating program. The key parameters to decide the thickness, morphology and the crystallinity of a spin-coated film are the solution concentration and spin speed. The type of solution is also crucial because the volatile evaporates fast and lead to speedy drying of the film with higher thickness compared to that coated with less volatile solvents.

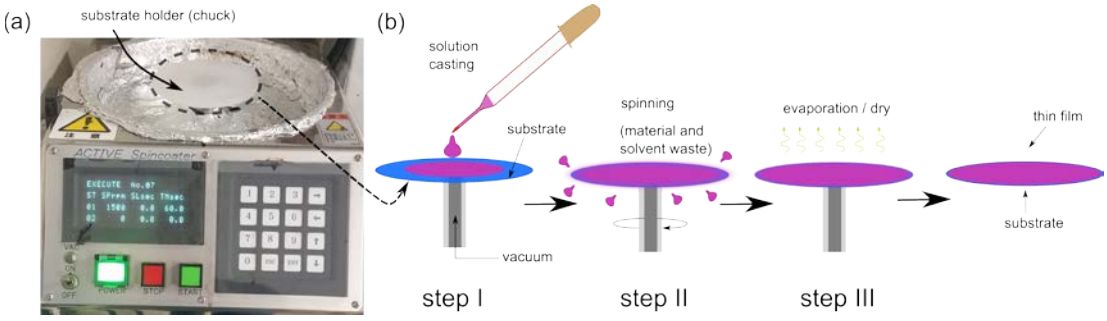

Figure 2.2 Digital image of a spin coating unit (a) and corresponding film fabrication mechanism.

2.2.2 Floating-film Transfer Method (FTM)

The floating-film transfer method is a recently developed technique to coat the oriented semiconducting polymer thin films[60,61]. In this technique, at first, the polymer thin films are fabricated at the interface of hydrophilic liquid and air. For oriented film fabrication, generally, the volatile solvent is selected and as the hydrophilic liquid substrate mixture of ethylene glycol and glycerol is utilized. The hydrophobic liquid (acting as the substrate for film fabrication) is pooled in a tray and ~10-15 µl of the polymer solution is placed on it. The polymer solution gets spread on the liquid substrate and simultaneously the solvent is evaporated. Moreover, during the expansion of the film the viscous hydrophobic liquid substrate exerts force in opposite direction to the expansion. Thus due to the simultaneous action of two opposing forces, the polymer backbones are oriented and since the solvent also gets evaporated fast, the oriented thin film is obtained. The film morphology can be optimized by tuning the casting parameters, which are: i) solution concentration, ii) viscosity of the liquid substrate, and iii) temperature of the liquid substrate. The solid film can easily be transferred to any desired substrate by stamping. Recently the expansion of the polymer thin film was controlled using a custom made slider which led to the formation of large area (>20 cm^2) oriented thin films with just one drop of the polymer solution, as shown in **Figure 2.3**.

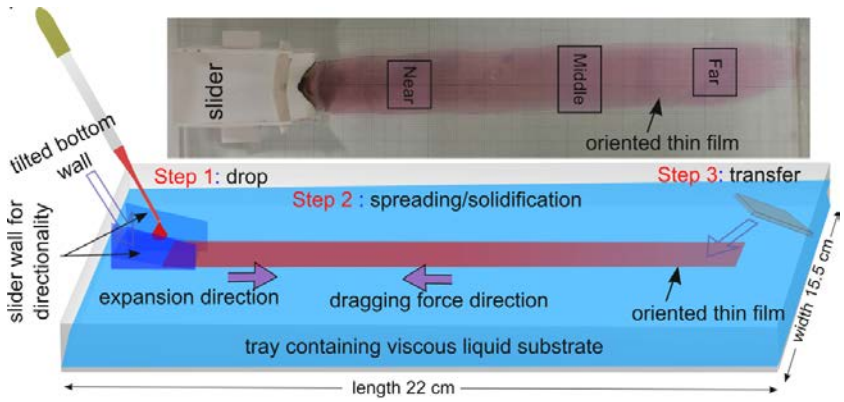

Figure 2.3 Schematic representation of thin-film fabrication by Floating Film Transfer Method and the digital image of a representative thin film.

Thus this technique is very cost-effective. The key advantage of this technique is that it qualifies the layer by layer casting of the solution-processed polymer thin films without damaging the existing layers on the substrate.

2.2.3 Friction Transfer Technique (FT)

Generally, the friction transferred thin films is fabricated on the bare substrate (glass, silicon or Si/SiO2) due to better adherence of the thin films; however, with some polymers with lower contact angle, the FT thin films can be cast on SAM treated substrate also. At first, a pellet is fabricated with the desired conjugated polymer powder for which it is compressed under ~1280 kgf/cm^2 for around 3 h. Subsequently, the pellet is sliced into two semi-circular parts. The flat surface of the semi-circular pellet-cut, attached to a pellet-holder, is fixed on the substrate mounted on the mobile stage, as shown in **Figure. 2.4**.

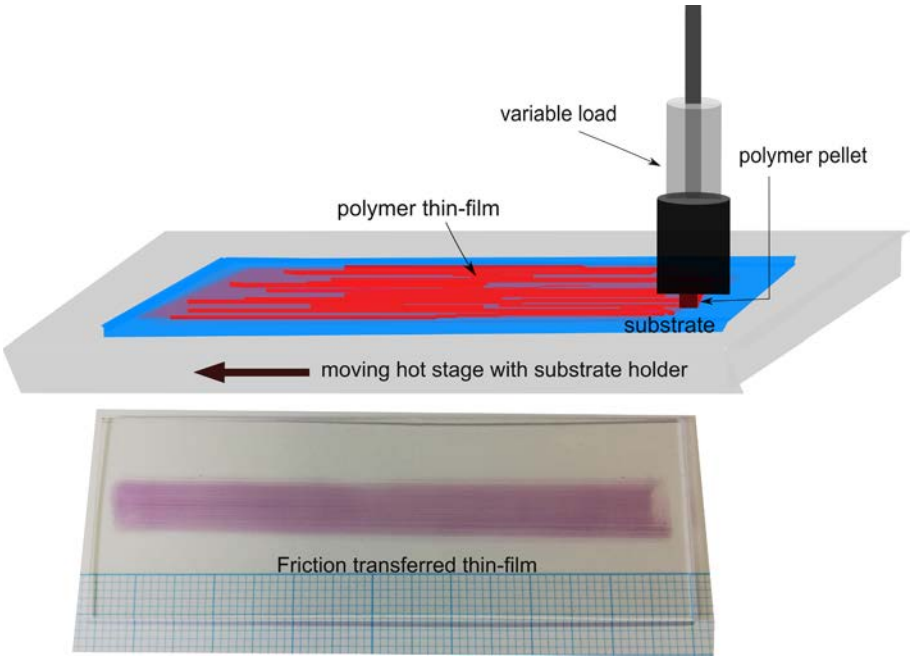

Figure 2.4 Schematic Illustration of Friction Transferred Technique for thin film fabrication. A digital image of representative friction transferred polymer thin film.

For friction transferred film fabrication, the pellet is squeezed and drawn on the substrate by moving the stage. Through this technique, the polymer backbone is aligned along the drawing direction and the extent of orientation is optimized by varying the casting parameters, which are squeezing load, stage speed, and substrate temperature. In the case of friction transfer of PBTTT C14, it was observed that at lower speed the thin films were more oriented which is further discussed in Chapter 4. In this casting technique, the shear force between the pellet and the substrate acts along the substrate plane, therefore generally face-on conformation is induced to the polymer backbone[62]. Although by annealing at high temperature there are chances for conformational change from face-on to edge-on[63], the extent of conformational change is highly sensitive to the substrates surface energy.

2.2.4 Drop Cast Technique

Generally, a high boiling point solvent is preferred for thin-film fabrication through the drop-cast technique which assists in slow solvent evaporation. Drop-casted films are prepared by placing drops of the polymer solution on the desired substrates which further covered with a petri-dish in order to control the slow solvent evaporation rate, the schematic illustration for thin-film fabrication is shown in **Figure 2.5**. Due to slow solvent evaporation, the polymer backbone gets sufficient time to attain more thermodynamically stable edge-on conformation, and thin-film crystallinity increases due to improved self-assembly.

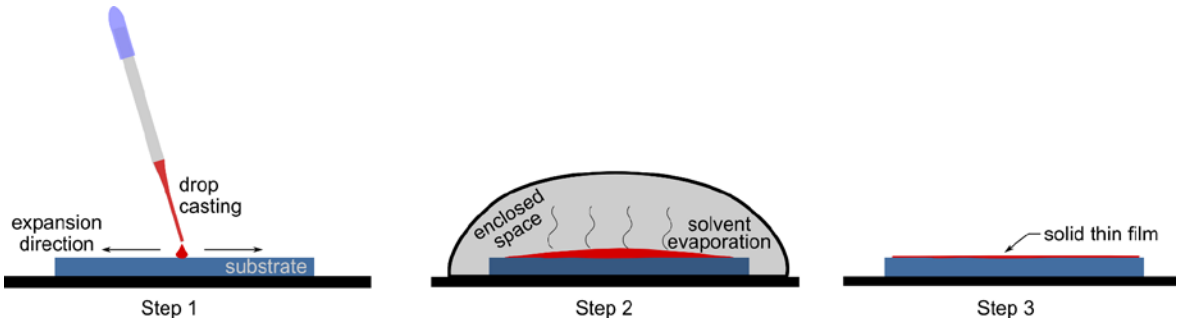

Figure 2.5 Schematic Illustration of Drop-cast Technique for thin-film fabrication.

2.3 Device Fabrication and Evaluation

2.3.1 Substrate Preparation

OFETs were fabricated in bottom gated top contact architecture on Si wafers which has heavily p-doped Si (as the gate) and thermally grown SiO_2 layer (of thickness 100 nm or 300 nm) at top acting as the dielectric. The capacitance values for the dielectric layers of thickness 100 nm and 300 nm were 30 nF/cm^2 and 10 nF/cm^2 respectively. The substrates were cleaned thoroughly by ultra-sonicating them sonicating in acetone, isopropanol, and ultra-pure water for 10 minutes each. Further, the substrates were dried and annealed at 150 °C under ambient conditions. Some of the substrates were also subjected to hydrophobic treatment by immersing them in the 10 mM solution of octadecyltrichlorosilane, following the reported literature[31].

For vertical device structure either ITO coated or plane glass substrates were utilized. To pattern, the bottom electrode desired portion of ITO was covered with polyimide tape and the remaining area was etched using the mixture of ZnO powder and hydrochloric acid. All the substrates were thoroughly cleaned similarly mentioned above followed by annealing at 150 °C for 1 h. Bottom electrodes on bare glass substrates were deposited by patterning thermally evaporated metal, under a high vacuum (pressure below 10^{-6} Torr).

2.3.2. Deposition of Active Layers and Electrodes

Isotropic thin-films of organic semiconductors were cast through spin-coat and drop-cast techniques whereas oriented thin films were deposited through FTM and friction transfer techniques. The top electrodes for OFETs i.e., source and drain, were patterned using Ni-mask of desires channel length and width as shown in **Figure 2.6**. For the vertical device structure, polymer thin films were coated on a glass substrate with the patterned bottom electrodes and the top electrode was deposited as metal strips orthogonal to the bottom electrodes, as schematically shown in **Figure 2.7**. For electrical characterization, the devices were fixed in a rigid box having conducting pins to which the electrodes were connected using thin gold wires.

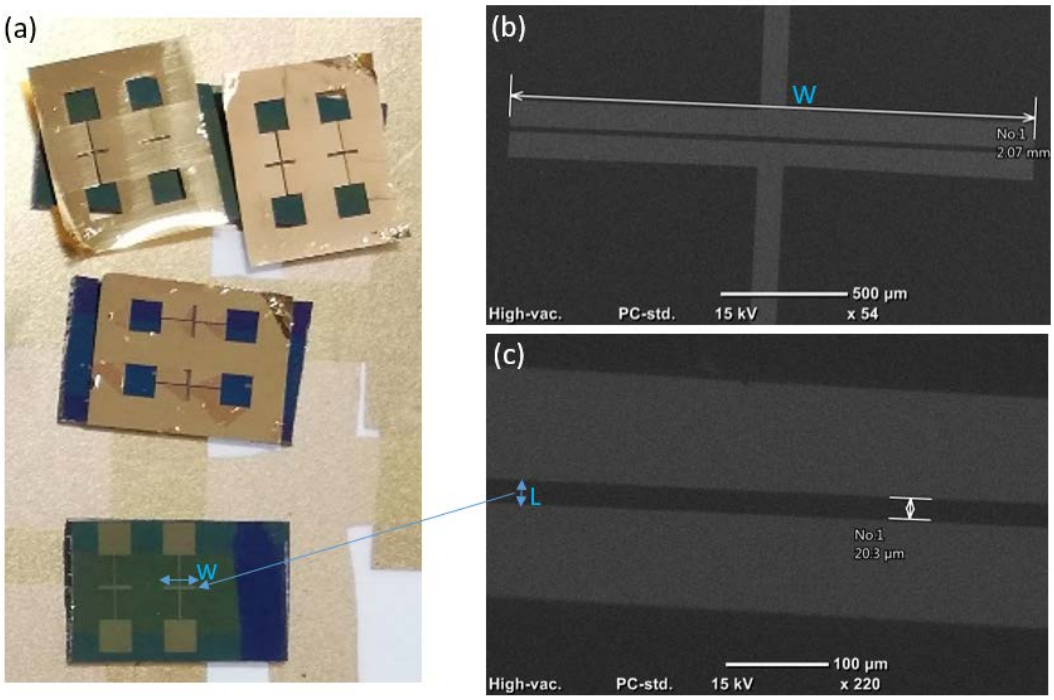

Figure 2.6 Digital image nickel shadow mask put on organic semiconductor film coated on Si substrates (a) and the bottom section of (a) shows thermally evaporated gold source and drain electrodes patterned with the shadow mask. Scanning electron microscope images of the channel width (W) of ~2 mm (b) and channel length (L) of ~20 µm (c).

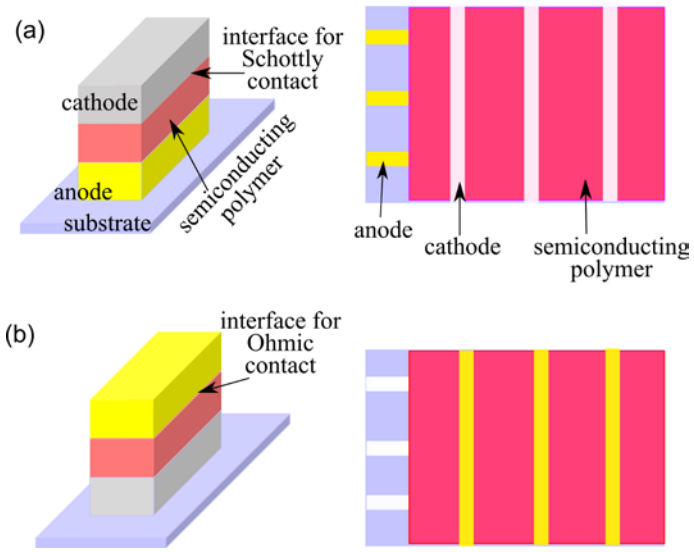

Figure 2.7 Schematic representation of the organic Schottky diodes with different architecture with Schottky contact at above (a) and below (b) the semiconductor layer; side views (left) and top views (right).

2.3.3 Electrical characterization

The electrical characterization of the devices was conducted under mild vacuum, pressure ~ 10^{-2} Torr. The current-voltage measurements of both OFET and diodes were conducted using a Keithley 2612 two-channel source-meter interfaced with a computer. For OFET's characterization, both the channels were operated to connect its three terminals. The field effect mobility (μ), the threshold voltage (V_{th}), and ON/OFF ratio of the OFET were estimated from their transfer characteristics as depicted in **Figure 2.8**. To estimate the μ, the saturation region the $\sqrt{I_{DS}}$ vs V_{GS} characteristics were analyzed with the help of Eq. (2.1 and 2.2).

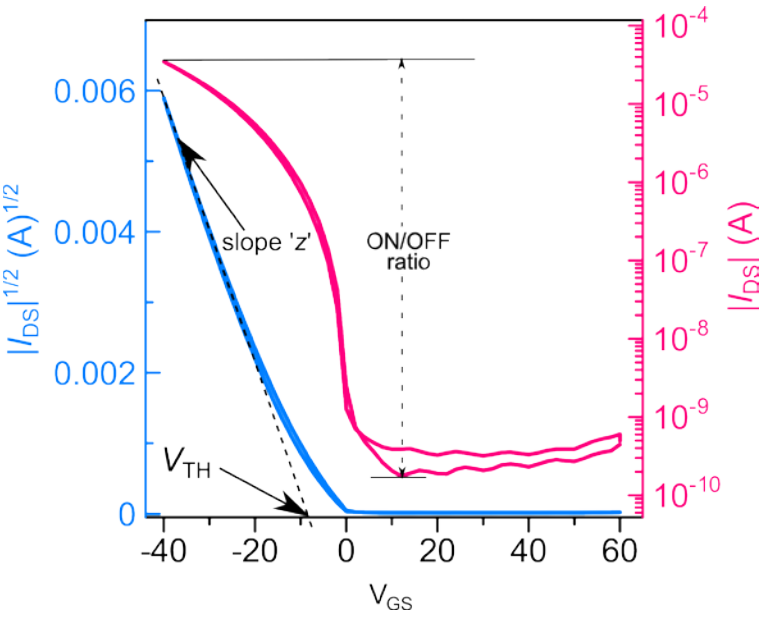

Figure 2.8 Representative transfer characteristics of OFET with the active layer of PBTTT-C14.

$$I_{DS} = \frac{C_i \mu W}{2L} (V_{GS} - V_{TH})^2 \tag{2.1}$$

After differentiating Eq. (2.1), rearranging and putting $\frac{\partial \sqrt{I_{DS}}}{\partial V_{GS}} = z$ the saturation mobility of an OFET can be written as follows:

$$\mu = \frac{2z^2}{C_i \frac{W}{L}} \tag{2.2}$$

The electrical performance of the organic Schottky diodes were conducted using one of the channels of the same source-measure unit as above. The ln$J$ –V plot of RR-P3HT based organic Schottky diode is shown in **Figure 2.9**. The diode parameters, i.e., reverse saturation current (J_0), ideality factor (η), and barrier height (ϕ_B) were calculated using the following expression corresponding to thermionic emission pphenomena[64–67]:

$$J = J_0 \left[\exp\left(\frac{qV}{\eta kT}\right) - 1\right] \tag{2.3}$$

Where,

$$J_0 = A^* T^2 \exp\left(-\frac{q\phi_B}{kT}\right) \tag{2.4}$$

Here J is the current density through the diode and V represents the applied voltage across it. k is the Boltzmann constant A^* is Richardson constant, T represents the ambient temperature and q is the electronic charge. At room temperature, when forward bias $V > (3kT/q)$, the thermionic emission model Eq. (2.3) can be approximated Eq. (2.5) [64–67]

$$J = J_0 \left[\exp\left(\frac{qV}{\eta kT}\right)\right] \tag{2.5}$$

From Eq. (2.5), J_0 can be estimated by extrapolating the linear section of the $\ln J$ versus V plot to $V = 0$ V. Moreover, the η is obtained from its slope. Therefore, calculating η Eq (2.5) is differentiated and rearranged resulting in Eq. (2.6).

$$\eta = \frac{q}{kT}\frac{dV}{d(\ln J)} \tag{2.6}$$

It was observed that the lower slop region which results in a higher value of η is more appropriate because in that region only the nonlinearity was evidenced in J versus V plot which is the typical nonlinearity as an effect of thermionic emission as described in Eq. (2.3).

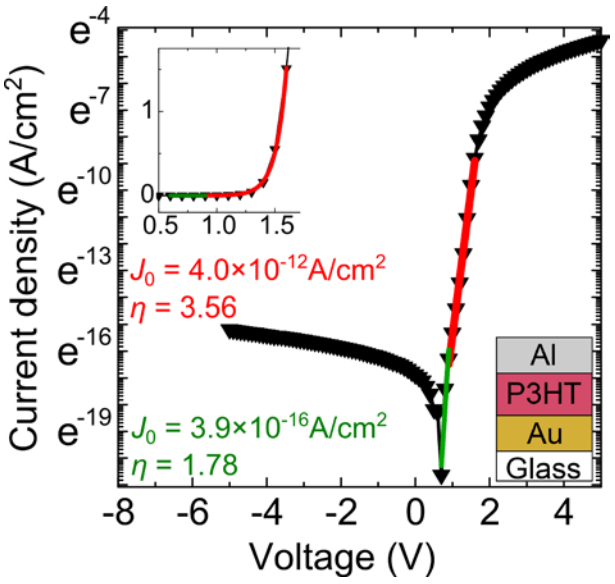

Figure 2.9 (a) ln*J* versus *V* plot for the organic Schottky diode with the device as schematically shown in the inset. Reproduced with permission[68]. Copyright (2019) American Institute of Physics.

Further, to measure the frequency response of the organic Schottky diodes, it is connected in series with a load resistor and a variable frequency AC-voltage source (Multi-Function Generator, WF1974). An oscilloscope (Agilent MSO-X 2004A) was connected across the resistor to monitor the ripple voltage. The rectified output voltage across the load resistance was measured and was compared with the input signal to determine the optimum frequency limit of the diode.

2.4 Thin-film Characterization

2.4.1 Ultraviolet-visible spectroscopy

When light is incident on organic materials having π electrons, it can be absorbed partially depending on the energy band gap in the organic material. Because the wavelength which corresponds to the required energy for exciting the ground state π electrons to a higher state π* orbital, is maximum absorbed and the λ_{max} can also vary depending on the film crystallinity. Therefore the resulting absorption spectra provides many key information regarding the sample. In this thesis work, for UV-Vis-NIR absorption spectroscopy the polymer thin film was coated on a

glass substrate and characterized by a dual-beam spectrophotometer (JASCO V-570). Moreover, to characterize the extent of optical anisotropy (due to oriented polymer backbone) in the thin film, a Glan−Thompson prism was also kept between the sample and the light source. Due to incident light, the π-π* transition occurs in the conjugated polymer and the corresponding dipole moment lies along the polymer backbone direction. Thus if the polymer thin-film is oriented, then the incident linearly polarized light be absorbed maximum when the polarization direction of the incident light is kept parallel to the backbone orientation direction (∥). Similarly, the absorbance will be minimum, when they are orthogonal (⊥). Further by comparing both of these absorbance values, the extent of orientation can be estimated in terms of dichroic ratio (DR) $=A_{\parallel}/A_{\perp}$, where $A_{\parallel}$ represents the maximum absorbance at $\lambda_{max\text{-}\parallel}$ (the wavelength corresponding to which the parallel absorption spectrum exhibits the maximum absorbance value) in the case of ∥ incident light and $A_{\perp}$ represents the absorbance value of spectra when the incident light is polarized ⊥.

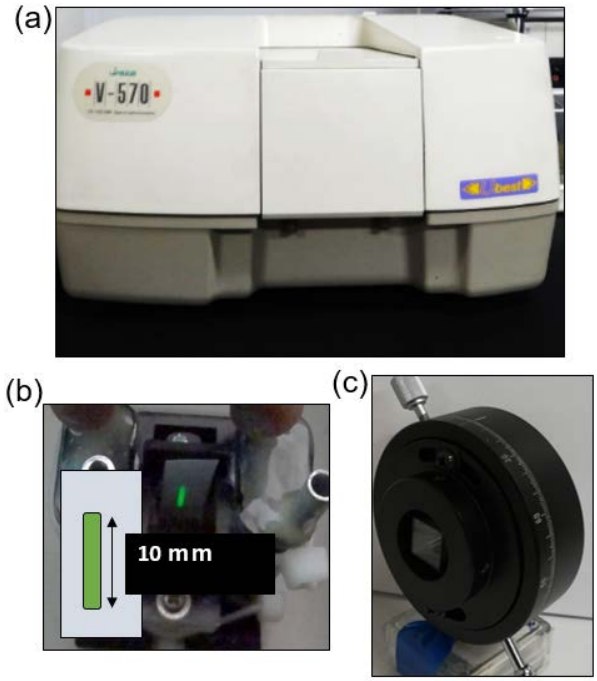

Figure 2.11 Digital image of (a) JASCO V-750 UV-vis spectrophotometer, (b) beam area scanned on the substrate, and its schematic is shown in the inset, and (c) Glan- Thomson prism utilized for polarized absorption spectroscopy.

2.4.2 X-ray Diffraction (XRD)

XRD measurement reveals the crystallinity, and macromolecular arrangement present in the thin films of organic semiconductors. The semiconducting polymers can attain stacking along any of the three-axis which simply can be defined as i) along the alkyl side-chains (a-axis), ii) along the intermolecular p-p-stacking (b-axis), and iii) along the polymer backbone, i.e., monomer repeat units (c-axis). Depending on the presence of such stacking in the polymer thin films (a00), (0b0), and (00c) peaks respectively can be obtained in the XRD pattern. The polymer backbone can attain three types of conformations with respect to the substrate, which is edge-on, face-on, and end-on[11]. Therefore, out-of-plane and in-plane XRD measurements are required for proper analysis of the polymer thin film. Out-of-plane XRD measurement provides the information regarding the type of stacking along the film thickness, and in this case, the typical θ - 2θ XRD measurement can be conducted, as schematically shown in **Figure 2.12 (a)**. In this thesis work, such measurements were conducted by a Rigaku X-ray diffractometer. However, in this setup the incident X-rays are not surface sensitive, therefore, it is not appropriate for in-plane characterization. Further, for in-plane measurements, the X-ray was incident at the grazing angle (ω) with respect to the substrates. When the grazing incidence angle is kept below the critical angle ($\omega < \omega_c$) the incident X-rays are totally externally reflected because of its index of refraction being <1. Consequently, the evanescent field propagates within the sample which is surface sensitive. Hence, based on this mechanism the in-plane grazing incidence X-ray diffraction (GIXD) measurements are conducted to characterize the microstructural distribution along the polymer thin film. In this thesis work, the in-plane GIXD measurements were conducted through Rigaku smart lab X-ray diffractometer. A typical schematic for GIXD measurement is shown in **Figure 2.12 (b)**.

During in-plane GIXD measurements, by keeping the incident X-ray at an appropriate ω with respect to a film (substrate is rotated in its plane), the surface and near-surface microstructures

are characterized. Since semiconducting polymer (having quasi 1-dimensional structure) can be oriented in the thin film, therefore, to characterize the anisotropic macromolecular arrangement in the plane of the film, in-plane GIXD measurements were conducted by keeping the scattering vector (S) parallel ($\chi = 0°$) and perpendicular ($\chi = 90°$) to orientation direction[11,69,70]. Further, by rotating any two of X-ray source, sample, and detector; along out-of-plane of the film (considering the Bragg diffraction conditions), macromolecular arrangement along the film thickness is obtained.

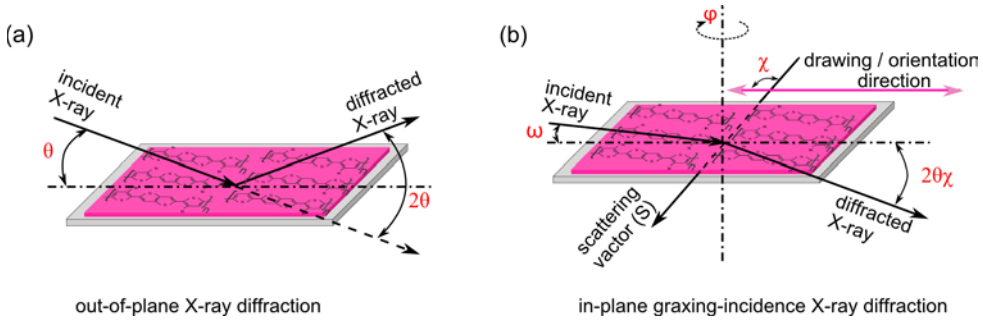

Figure 2.12 Scheme for out-of-plane XRD (a) and in-plane GIXD (b) measurements. Reprinted with permission from[70]. Copyright 2020 American Chemical Society.

2.4.3 Atomic Force Microscopy (AFM)

AFM is a sophisticated measurement technique which can characterize the atomic level distribution on the film, also known as the surface topography. The working principle of AFM is, in this technique the differential analysis of the atomic level interaction between the AFM tip and the sample surface reveals the surface morphology. Through this technique, any type of sample (conducting film, semiconducting film, and insulating film) can be efficiently characterized. The AFM tip gets deflected due to force between the tip and the sample when the cantilever is brought closer to the surface of the sample. The interaction between the tip and the surface can be of various types such as van der walls, chemical, capillary, mechanical, or electrostatic, etc. Generally for characterizing the soft films like that of semiconducting polymers, the tapping mode AFM measurement is preferred, which decreases the chance of sample damage or frequent tip contamination. During AFM measurement, the bending of the cantilever is recorded by focusing a laser beam on its back (opposite to the tip side), which further is reflected. The reflected beam is

detected by a position-sensitive photodetector, which subsequently converts it into an electrical signal. Hence the bending in the cantilever (due to tip-surface interaction) is finally converted into the electrical signal. In this thesis work, AFM measurements were conducted through a JEOL SPM5200 with Olympus probe (OMCL- AC200TS-C3) setup (digital image is shown in **Figure 2.13**) which was operated in the tapping mode.

Figure 2.13 Digital image of the AFM measurement setup

Chapter 3. 2D Positional Mapping for Swift Microstructural Characterization of Large Area Thin-films

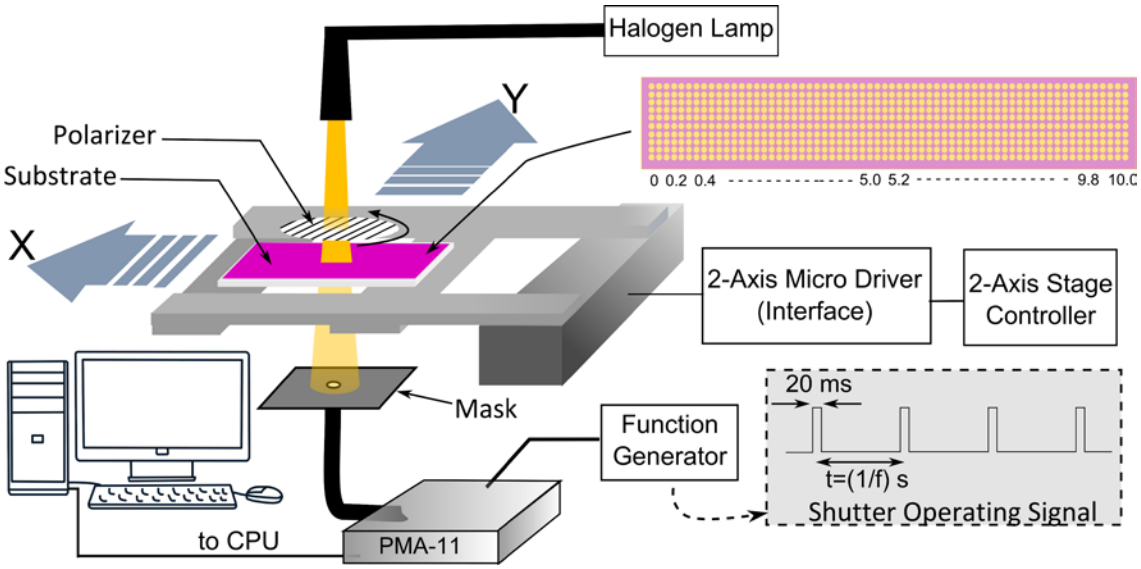

- **N. Kumari**, M. Pandey, S. Nagamatsu, S. S. Pandey "2D Positional Mapping of Casting Condition Driven Microstructural Distribution in Organic Thin Films" *Japanese Journal of Applied Physics* 59(SC) (2019), SCCA06.

- **N. Kumari**, A. Tripathi, S. Sadakata, M. Pandey, S. Nagamatsu, S. Hayase, S. S. Pandey "2D positional profiling of orientation and thickness uniformity in the semiconducting polymers thin films" *Organic Electronics* 68 (2019), 221–229.

3.1. Introduction

Organic semiconductors have drawn widespread attention in the recent past due to their vital application in diverse areas of flexible, wearable, and transparent electronics[71–73]. Inexpensive and uncomplicated solution based techniques for fabricating organic electronic device makes it a potential candidate for large scale fabrication of flexible electronics[55,74,75]. In this regard, SPs with their better solution rheology and high solubility in common organic solvents became more desirable for printed electronics[14]. Charge carrier transport in organic semiconductors occurs through π–electron clouds along the conjugated backbone or overlapped between adjacent molecules, assisted inter and intra-chain as well as inter-domain hopping[76,77]. The recent past has witnessed a huge improvement in transport characteristics of OSCs by enhancing thin-films crystallinity and macromolecular ordering through various casting techniques[11]. The quasi-one-dimensional nature of SPs plays a significant role in deciding the device performance. Especially, dramatic enhancement in μ of the SPs is expected while orienting the polymer backbone along the OEFTs′ channel direction[11,26]. For instance, significant enhancement in the μ of SPs, reaching beyond 10 $cm^2/V{\cdot}s$, has been reported by orienting the SP backbone[78–80]. However, morphologically uniform thin-film fabrication and their reliable characterization at large is one of the existing challenges to be addressed before the anticipated commercialization of organic electronics. Various technologies have been developed to fabricate large area thin films, such as FTM[81], solution shearing[55], dynamic-template-directed orientation[33], etc. However, for large area solution processed thin films, their thickness and morphological variations are should be controlled in order to obtain device reproducibility, which instigates the need for swift and precise characterization of distribution in microstructural characteristics of the thin films. There are various sophisticated techniques for microstructural characterization of the thin-films, for instance, XRD,

GIXD, AFM, atomic force microscopy, near edge x-ray absorption fine structure spectroscopy, variable angle spectroscopic ellipsometry, polarized absorption spectroscopy etc.[69,70,82,83]; however, it may be a troublesome job to utilize them for large scale characterization. Considering the inevitability of swift and economical scale characterization of the thin films, a new technique for two-dimensional (2D) positional mapping of thickness and macromolecular ordering in large area thin films was developed. In this mapping technique, the point-areas of thin-film coated on glass substrate were illuminated with a white light beam, and the transmitted light was collected by a multichannel detector. Due to simultaneous illumination and detection in the whole wavelength region for each point, a complete absorption spectrum was generated instantaneously. Using the mobile stage whole sample was characterized in no time. Since the absorbance corresponding to different wavelength depends on the material characteristics as well as thin-film morphology[84], therefore, by integrating measured absorption spectra the microstructural distribution throughout the sample was obtained.

3.2. Experimental Details

PBTTT-C14, P3HT, dehydrated chloroform, 1,2-dichlorobenzene, were purchased from Sigma Aldrich. Two types of spin-coated samples were fabricated on glass substrates (25 mm × 10 mm). For one the casting solution was prepared by dissolving PBTTT-C14 in 1,2-dichlorobenzene in concentration 0.25% (w/w), which was spun at 1500 rpm for 120 s. The other solution was made with P3HT by dissolving it in super dehydrated chloroform in concentration 1% (w/w), which was spun at 2500 rpm for 40 s. For FTM film fabrication PBTTT-C14 was dissolved in hot chloroform in the concentration 1% (w/w). Further large area floating-films were prepared by placing one drop (~15 μL) of the solution on the orthogonal liquid substrate. As the liquid substrate, a mixture of ethylene glycol and glycerol in 3:1 ration was properly stirred and kept at temperature ~ 55 ℃. The

unidirectional film growth was guided by the inclined surface of the custom made slider as schematically shown in **Figure 2.3**. Samples were stamped on 25 mm × 10 mm glass substrates from three different locations of ribbon-shaped thin-film. The samples were characterized by a conventional double beam UV–Vis spectrophotometer (JASCO V-570) and 2D positional mapping technique, system details are provided in the next section.

3.3. Results and Discussion

3.3.1. Setup and Operating Principle of 2D Positional Mapping:

Photonic multichannel analyzer (PMA), (C7473-36, Hamamatsu Photonics, Japan) is the central part of the mapping system. The other internal components are a halogen lamp (Megalight 100, Schott, IBE SMT Equipment, Magnolia) coupled with optical fiber and focus lens, a 2D mobile stage (Stepping motor-drive SGSP stage/TSDM series, Sigma Koki, Japan) interfaced with a 2D stage controller (Mark-12, Sigma Koki, Japan), a sample holder fixed to the mobile stage, a digital function generator (DF1906, NF Corporation, Japan), a polarizer fixed on a rotation motorized stage, SGSP-40YAW, Tamagawa Seiki, Japan, and a 4-axis stage controller (SHOT-304GS: 4 axes, Sigma Koki Co., Ltd., Japan) coupled with controller pad (CJ-200, Sigma Koki Co., Ltd., Japan) for controlled rotation of the polarizer. All the components were assembled as the schematic diagram shown in **Figure 3.1**. PMA which consists of a Czerny-Turner type spectrograph and thermoelectrically cooled back-thinned charge-coupled devices (BT-CCDs) as photodetectors with electronic shutter function. An array of 1024 photosensitive BT-CCDs is there inside the PMA to accomplish multichannel spectroscopy. The multi-channel detector and the diffraction grating are rigidly fixed to get reproducible results. The shutter connected to the photodetector unit was controlled through a pulsed signal produced by the function generator. An illustrative schematic for the mechanism of multichannel spectral detection inside the PMA has

been schematically shown in **Figure 3.2.** The 2D mobile stage with a sample holder was fixed at ~10 cm distance from the focus lens to get optimum illumination intensity and for easy handling.

The effective aperture of the optical fiber of the PMA has a diameter of 1 mm, which limits the least possible area to be scanned, to a diameter of 1 mm. In the present setup, a mask with an orifice in the range of 0.1 mm - 0.9 mm was placed before the detector optical fiber to control the light-receiving area. In the present system, the possible range of stage speed was between 1 mm/s to 10 mm/s. The rate of signal detection was controlled by tuning the shutter opening frequency rectangular pulsed signal (between 0.1 mHz to 2 MHz). Since the sample stage is mobile, so the ON state of the pulsed signal should be such that the PMA can receive the transmitted beam corresponding to each point area without any interference from the neighboring point area. To avoid the interference, the ON state duration of the rectangular pulse signal was fixed to 20 ms (**Figure 3.1**), it is also the lowest limit of exposer time for the detector of PMA.

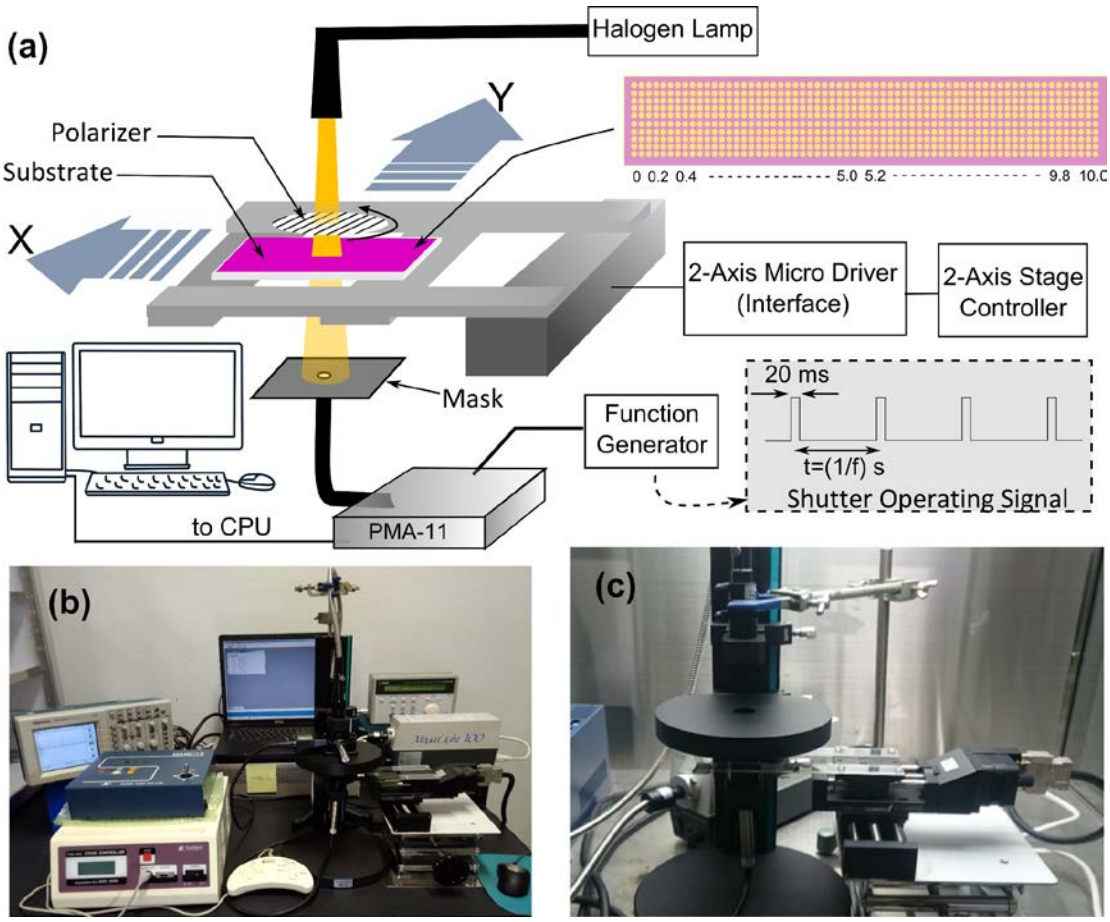

Figure 3.1 (a) Schematic illustration and (b) Digital image of 2D positional mapping set-up. (c) The magnified image to show adjustment of stage, illumination source, and detector. Reprinted with permission[85]. Copyright: 2019, Elsevier.

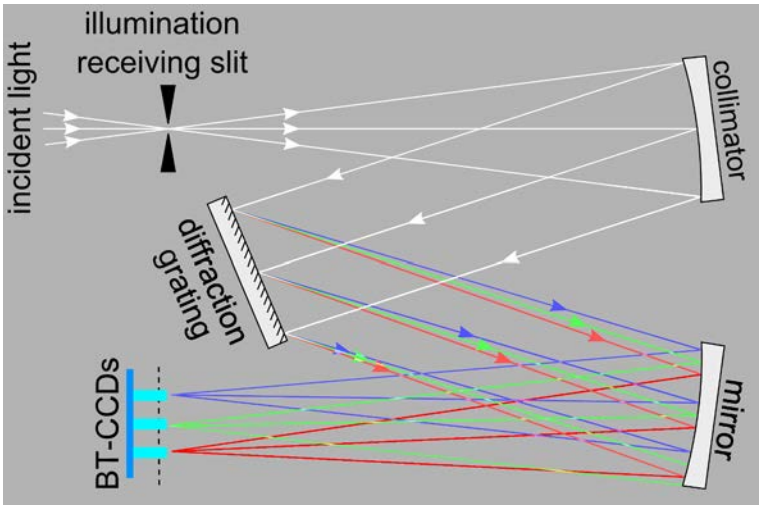

Figure 3.2 Schematic illustration for the working mechanism of spectrograph inside Photonic Multi-channel Analyzer. Reprinted with permission[85]. Copyright: 2019, Elsevier.

White light coming from the halogen lamp with a beam width of 5 mm was focused at a point area on the sample and the transmitted beam was collected by the aligned optical fiber connected to PMA. Inside PMA, the beam was collimated and dispersed by the spectrograph in constituent wavelengths. The dispersed optical signal was received by the array of photodetector leading to the formation of a complete absorption spectrum for the point area. For integration and analysis of the absorption spectra, PMA was interfaced with a computer. To improve the signal to noise ratio five consecutive absorbance data of the absorption spectrum were averaged out and such spectra corresponding to each point areas were further integrated. For more accurate mapping of the thin-film the area of the point and the gap between two points was kept as minimum as possible by optimizing measurement parameters such as i) mask diameter, ii) stage speed, and iii) shutter operating frequency with the following correlation:

$$\text{Mask diameter} = \frac{\text{Stage speed}}{\text{Shutter operaing frequency}} \qquad \text{Eq. (3.1)}$$

3.3.2. Thin-film Characterization:

In order to map the thickness and/or molecular orientation, thin-film cast on a glass substrate was mounted on the substrate holder attached to the mobile stage. The absorbance of the bare substrate was measured as a baseline before characterizing the thin film cast on the same substrate. Further, the variation in peak-absorbance of the absorption spectra was correlated with the corresponding thickness of the thin-films using Beer-Lambert law[85,86]. Position dependent absorption spectra were measured at continuous point areas along multiple lines through aligned light source and detector and by the controlled movement of the sample stage. Non-polarized and polarized electronic absorption spectra of the point areas were measured probe the variation of thickness and molecular orientation (if present), respectively.

3.3.2.1 Mapping of thickness variation:

Uniform and pinhole-free thin films are essential for the fabrication of high-performance devices; however, but there are fewer reports about the uniformity of spin-coated films. To explore the thickness uniformity, 2D positional mapping of spin-coated PBTTT-C14 films was performed with measurement parameters as stage speed of 1 mm/s, mask diameter of 0.2 mm, and shutter operating frequency of 5 Hz with 10% duty cycle. Though spin-coated films seem to be uniform by the naked eye (**Figure 3.3**), the mapped thickness profile reveals that films are not that much uniform and films in the center region are thinner as compared to that towards edges. In **Figure 3.3**, the projection of the sample's thickness profile in a horizontal plane, depicted by pink closed circles, represents the location of the corresponding mapped point-area on the sample. A partly magnified image shows the continuous arrangement of 25 point-areas (with a diameter of 0.2 mm) within 5mm width. The whole sample was mapped point by point and the discrete thicknesses were integrated to visualize its thickness variation map. The increasing trend of thickness from the center towards the edges. Therefore, it can be claimed that small area spin coating might be good at the laboratory level but not much suitable for large area applications. Further to validate the reliability of this mapping technique, absorption spectra at a point area near the center measured by this technique and the absorption spectra obtained through conventional spectrophotometer were compared. From the perusal of **Figure 3.3** it is clear that peak-absorbance, λ_{max}, and vibronic features are almost similar in both cases.

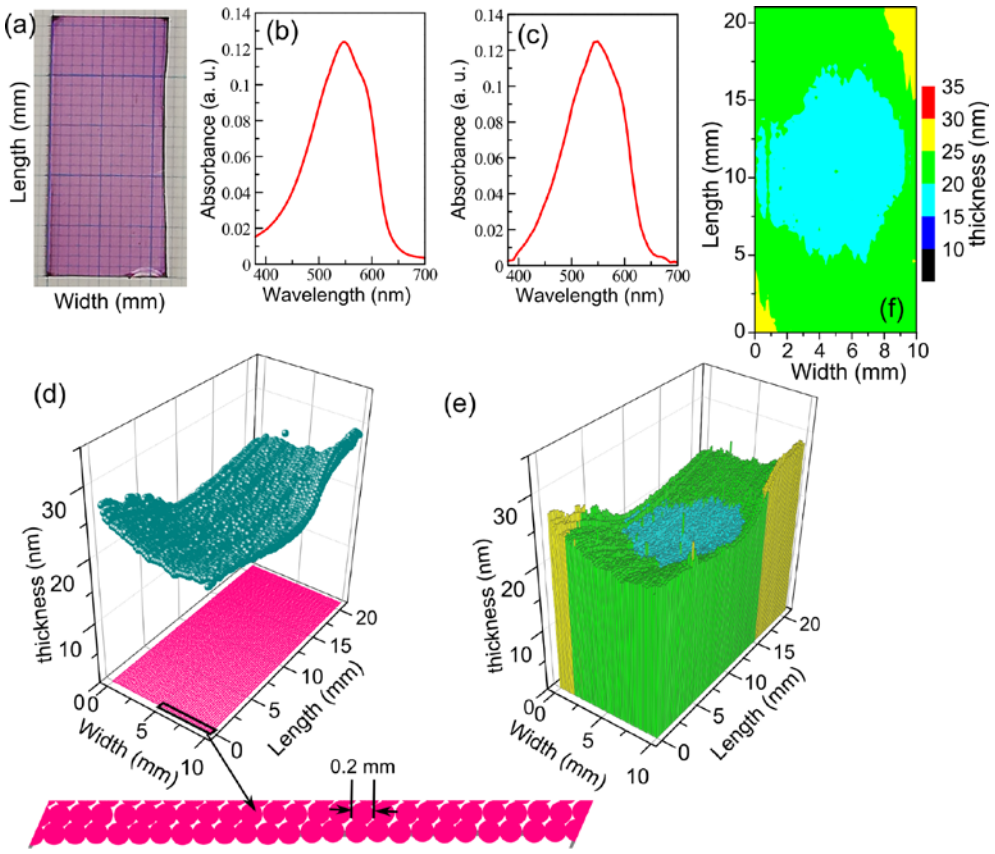

Figure 3.3 2D positional profile of thickness (a-c) in the spin-coated thin films of PBTTT-C14 (d). (a) Arrangement of point area (with diameter = 0.2 mm) on the sample and corresponding thickness. Discrete (b) and integrated (c) thickness profile of the spin-coated film (d). Electronic absorption spectra of the films obtained through the mapping system (near center) (e) and conventional spectrophotometer (f). Output curve (g) and transfer characteristics (h) for OFETs fabricated using spin-coated films. Inset in (g) is the device architecture of the OFET, where OTS treated substrates were utilized and samples were annealed similarly to the earlier cases. Reprinted with permission[85]. Copyright: 2019, Elsevier**.**

3.3.2.2 Mapping of variation in backbone orientation:

In order to map SP orientation, ribbon-shaped FTM tin-film of PBTTT-C14 was taken into consideration. When a drop of SP solution is placed at the interface of the slider and orthogonal liquid substrate, walls at both edges of the slider assist the unidirectional expansion of the SP solution leading to the formation of large area ribbon-shaped thin films, as schematically shown in **Figure 2.3**. Quick solvent evaporation and simultaneous action of opposing viscous force during film expansion result in solid oriented thin-film floating on the liquid substrate. In this work floating films of length >15 cm long along the expansion direction were fabricated on a hydrophilic

liquid substrate. To probe the variation in molecular orientation and thickness, three substrates (10 mm × 10 mm) were used to stamp samples from the floating films. Each sample was taken at 5 cm gap from the film at different positions i.e. 1) far, 2) middle, and 3) near, from the slider side as shown in **Figure 3.4**. Thickness mapping of the samples was done similarly as the above-discussed case of spin-coated PBTTT-C14 samples. From the perusal of **Figure 3.4**, It can be seen that there is uniform thickness distribution in the far-end region of the film which can be attributed to higher freedom for the film expansion. For orientation mapping polarizer was placed between the illumination source and the sample and absorption spectra along (∥) and orthogonal (⊥) to ribbon width direction were me measured. The distribution of orientation (in terms of DR = $A_{\parallel}/A_{\perp}$) shown the opposite trend to that of thickness, as thinner films exhibited higher DR values and vice versa is also true. A close observation of the map of all three samples reveals that films are relatively uniform in the central area as compared to the peripheral region of the sample specimens. This can be explained considering the fact that film expands in the forward direction from the slider end but it tends to expand along the width direction too and viscous force along the width will be more prevalent. To verify the mapped orientation of the thin films, the same samples were also characterized through the conventional spectrophotometer, corresponding polarized absorption spectra are shown **Figure 3.3**, which match very well with results obtained through 2D positional mapping system.

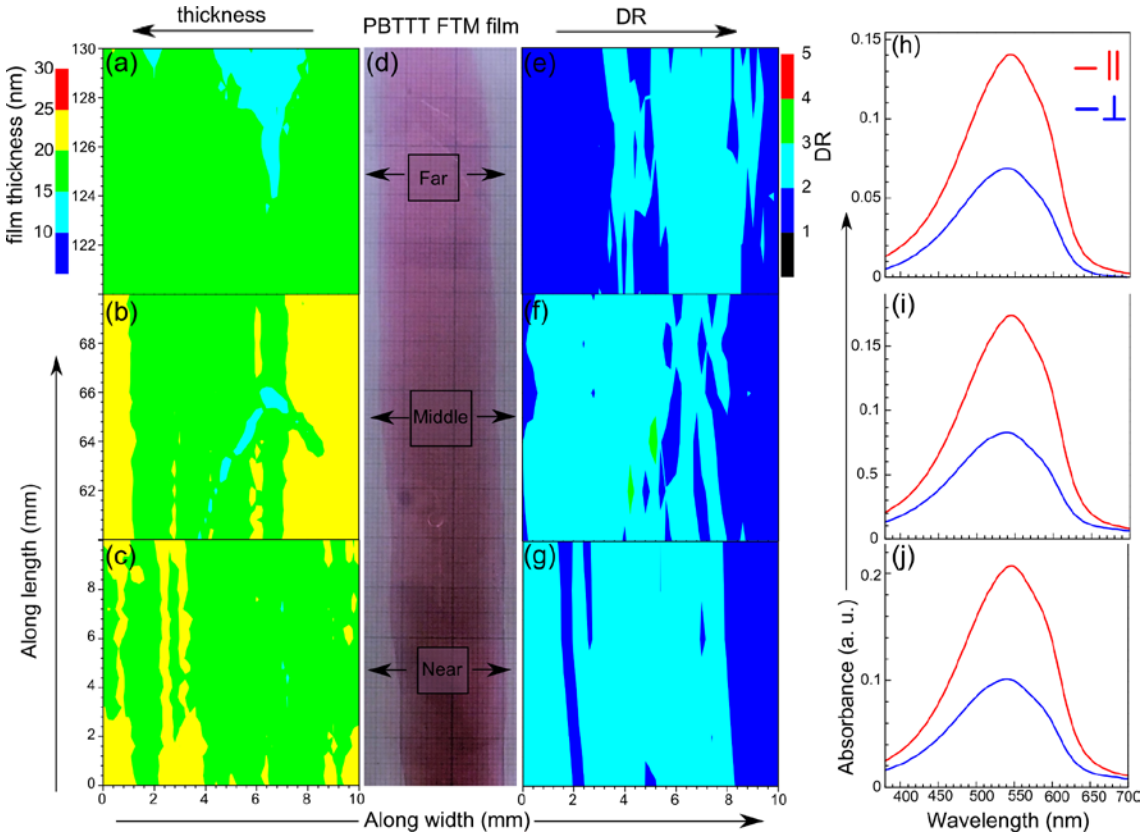

Figure 3.4 Mapped profiles of the thickness (a-c) and orientation intensity (e-g) for the PBTTT-C14 thin films fabricated by FTM (d). Corresponding polarized electronic absorption spectra (h-j) measured by conventional spectrophotometer is shown in the extreme right. Reprinted with permission[85]. Copyright: 2019, Elsevier.

3.3.2.3 Mapping of Intermolecular Ordering:

As discussed above, the peak absorbance was utilized to map thickness and SP orientation in the thin films. Besides, variation in the intensity, spectral width, and position of vibronic peaks can be utilized to map intermolecular interaction in the thin film[87,88]. To demonstrate it the spin-coated sample of a highly soluble SP, RR-P3HT was characterized through 2D positional mapping technique. In this case more volatile casting solvent, chloroform was chosen for film fabrication. Since rapid evaporation of the solvent can lead to higher morphological variations, which would be suitable to observe spectroscopic differences with more accuracy. The integrated peak absorbance of the whole sample reveals that the sample is non-uniform and the thinner region exists

near the center. To visualize the distribution in macromolecular assembly throughout the sample, the vibronic peaks of positional absorption spectra obtained through the mapping technique were analyzed in the light of Spano's model. From the perusal **Figure 3.5** variation in the vibronic shoulder in the absorption of spectra, measured at different locations along the diagonal, is clear. This is the evidence of variation in the P3HT thin-film crystallinity, which is known to promote the appearance of lower vibronic modes and arises due to the fibrous crystalline domain formation[89–91]. Especially, the growth of 0–0 modes in P3HT is discussed by Spano in detail correlating with the electronic structure of excitonic bandwidth (W) with intermolecular coupling transition energy, E_p, by Eq. (3.2) as shown below[84]. where $A_{0\text{-}0}$ and $A_{0\text{-}}1$ refer to respective intensities of 0–0 and 0–1 transition. Spano's model was applied for the detailed and quantitate analysis of inter and intramolecular ordering[84].

$$\frac{A_{0-0}}{A_{0-1}} \approx \left(\frac{1 - 0.24\frac{W}{E_p}}{1 + 0.073\frac{W}{E_p}} \right)^2 \tag{3.2}$$

Ep denotes the vibrational energy at 0.18 eV [87,88]. The calculated values of W are summarized in Table 3.1. The lower values of W were obtained for the central region of the thin film which corresponds to higher intermolecular ordering. Moreover, as discussed above the central region was also comparatively thinner. Therefore, it can be claimed that relatively slower drying near the spinning axis led to thinner and higher macromolecular ordering in the thin film.

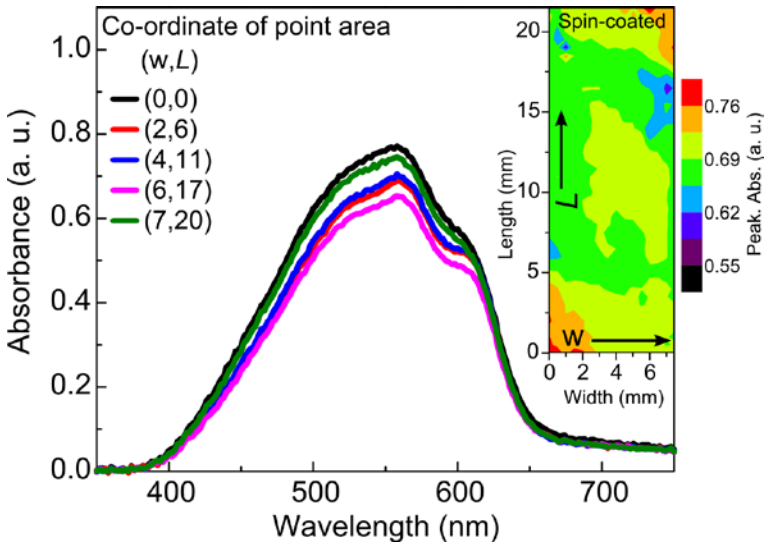

Figure 3.5 Position-dependent variation in the absorption spectra in terms of of relative vibronic peaks. Each spectrum was measured through 2D positional mapping technique on the spin-coated RR-P3HT thin-film. An integrated map of peak absorbance for continuous arrays point-areas (diameters ~0.5mm) is shown in the inset. Reprinted with permission[92].

Table 3.1 The value of excitonic bandwidth (*W*) at different locations of the spin-coated (SC) as shown in Figure 3.5. The position-dependent absorption spectrum was measured through 2D positional mapping technique. Reprinted with permission[92].

Point location	*W* (meV)
(0, 0)	556.41
(2, 6)	492.01
(4, 11)	491.83
(6, 17)	433.04
(7, 20)	537.74

3.4 Conclusion

2D positional mapping system has been developed, which is capable of swift profiling variation in thickness, macromolecular orientation, and intermolecular ordering of large-area thin films. The application of the mapping system was successfully demonstrated using various oriented as well as non-oriented thin-films of thiophene based SPs. Thin films were prepared by ribbon-shaped FTM, and spin-coating methods. Positional mapping of spin-coated thin-films of PBTTT-C14

shown a gradual increase in the thickness from the spinning center towards the edges. Similarly the mapped distribution in thickness and macromolecular ordering in spin-coated RR-P3HT shown that the central region of the thin-film exhibited lower thickness and more uniform morphology and high macromolecular ordering as well. In the case of the ribbon-shaped FTM film of PBTTT-C14, the far end region was more uniform and oriented as a consequence of higher freedom of expansion. The mapped thin-film morphologies were successfully verified by comparing them with the results obtained through conventional UV-Vis spectrophotometer. Hence, the 2D positional mapping technique can be successfully utilized to characterize the morphological distribution in the large-area organic thin-films for efficient thin-film fabrication and cost-effective utilization of the resources. Furthermore, in situ characterization during thin-films fabrication can also be explored as a further application of the mapping technique.

Chapter 4: Influence of Thin-film Morphology and Interfaces on Transport Characteristics of Organic Electronic Devices

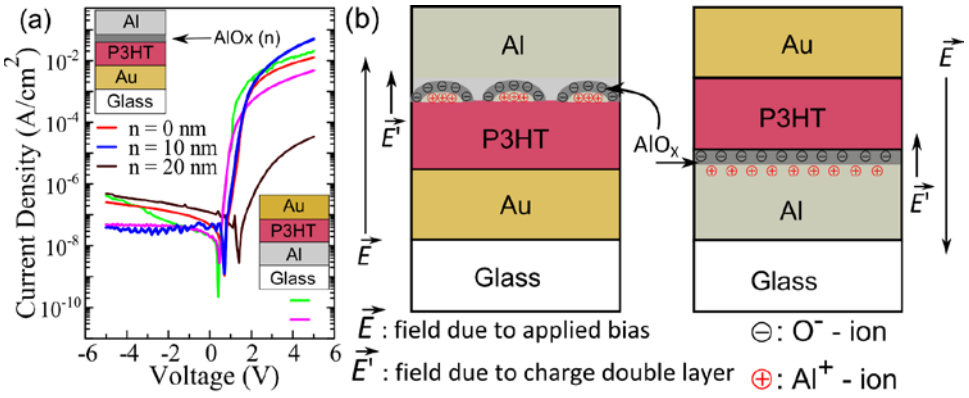

Fig. Electrical characteristics of the OSDs in the structure as shown in inset, (b) the schematic illustration regarding the effect of field due to charge double layer.

➢ **N. Kumari**, M. Pandey, K. Hamada, D. Hirotani, S. Nagamatsu, S. Hayase, S. S. Pandey "Role of Device Architecture and AlO_X Interlayer in Organic Schottky Diodes and Their Interpretation by Analytical Modeling" *Journal of Applied Physics* 126 (2019), 125501.

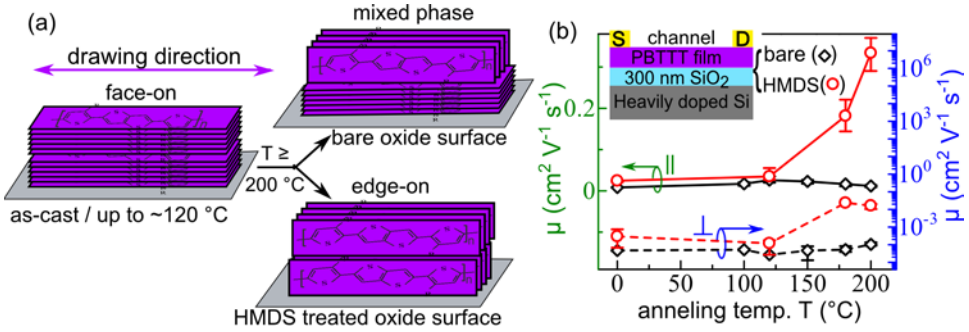

Fig. Schematic representation for conformational transformation in friction-transferred PBTTT after annealing on different surfaces (a) and its effect on corresponding charge transport anisotropy (b). Inset of (b) represents the schematic for OFET architecture

➢ **N. Kumari**, M. Pandey, S. Nagamatsu, M. Nakamura, S. S. Pandey "Investigation and control of charge transport anisotropy in highly oriented friction transferred polythiophene thin films" ACS Appl. Mater. Interfaces 12 (2020) 11876- 11883.

4.1. Introduction

The electrical performance of the semiconducting polymer (SP) based devices are highly sensitive to the bulk morphology of the semiconductor layer as well as the interfacial morphology. The interfaces can be divided into three categories, i) conductor/semiconductor (conductor/SC) interface which mainly influences the charge injection to and extraction from the organic thin films, ii) semiconductor/semiconductor (SC/SC) interfaces present in layer-by-layer[34] structures, and iii) semiconductor/dielectric (SC/dielectric) interfaces mainly present in planar device structures[11]. Though conductor in conductor/SC interface can be any of various organic or inorganic conducting materials, for lucid understanding only metal/SC interfaces will be considered throughout this exposition. The effective resistance encountered at the metal/SC interface is termed as contact resistance (R_C) which can be tuned by the varying the choice of metal, an organic semiconductor, and sometimes by an interlayer between them; however, the presence of trap states is well known to play a dominant role to determine the R_C[42–46]. The report by Tsukagoshi and coworkers demonstrated a valuable insight to understand the effect of trap-sites present at the metal/organic interface[43]. Despite the lower work function of copper (Cu) with a higher hole injection barrier at the Cu/pentacene interface, resultant R_C with Cu top contact was smaller than the corresponding Gold (Au) contact. Further, it can be argued that in the OFETs, if there exists a barrier for hole injection at source contact then there must not be any barrier for hole extraction where the metal/organic interface at both the contacts possesses a similar band structure. Since the magnitude of R_C was found to be of the same order, therefore, the domination of trap-states in determining R_C cannot be avoided[44]. The effective resistance inside the organic thin-film along with that at the SC/SC interface, if present, can be considered under Bulk resistance (R_B), which primarily depends on the thin-film crystallinity[31,77,93,94]. With a decrease in crystallinity of the thin-film effective carrier mobility decreases[95] leading to the formation of space-charge inside the thin film[96–101]. The

effective resistance due to SC/dielectric interface primarily hampers the charge transport in planar device structure like OFETs[102]. The presence of dipoles at the dielectric interface acts as trap-sites for the induced charge carriers near the SC/dielectric interface[102–104]. Moreover, the interaction between the SP backbone and dielectric layers also affects the morphology of the organic-thin film near interface[105]. Therefore to understand the transport properties of the OEDs, exhaustive analysis of the effect of thin-film morphology and interfaces is crucial.

In this chapter, the effect of the interfacial layer and the thin-film morphology on in-plane and out-of-plane charge transport have been discussed. To analyze the effects on out-of-plane/vertical charge transport, Organic Schottky diodes (OSDs) were fabricated with varying metal/SC interfacial properties, and the morphology of the SP thin film was also varied by opting different casting techniques. Though there are previous reports which deal with the physical phenomena of the organic diodes by analyzing the experimental observations through theoretical models. These models were developed by considering the bulk phenomena, the charge injection/extraction phenomena at the interface, or by their combined effect, as a function of the applied voltage.[96–101] However, the architecture-dependent deviation of the physical model from practical electrical characteristics remains a challenge.[99,106,107] Herein we report a robust model incorporating both interface and bulk phenomena of the organic Schottky diode (OSDs) as a function of current. OSDs were fabricated with varying metal/SC interface at Schottky contact and the morphology of the active layer was also varied. Through the comparative analysis of their current density – voltage ($J - V$) characteristics, the influence of bulk and interface on vertical charge transport was demonstrated. A Schottky diode consists of a SC layer placed between an Ohmic and an Schottky contact, for injection and blocking of current flow in forward and reverse bias, respectively[108]. Resultant rectification ratio (RR) of the diode depends on the quality of Schottky contact, high RR can be obtained with a large Schottky barrier. Most of the SPs in pristine

state show p-type behavior, therefore, low work-function cathode such as calcium, magnesium, etc. is recommended for efficient Schottky contact. Though with lower work-function they provide larger Schottky barrier, rapid device deterioration due to their less air-stability cannot be avoided[109]. Hence for optimum device performance, Al was selected as the electrode for Schottky contact with P3HT and Ohmic contact was realized with Au[65]. Besides the unique property of Al, a decrease in work-function after oxidation was utilized to improve RR of the OSDs[40,110,111]. A thin AlO_X interlayer was placed between P3HT and Al to investigate their influence on the transport properties of the OSDs. The interfacial AlO_X layer was also characterized through AFM, XPS, and UPS for better interpretation of its effect on the overall device performance. Further, to see the influence of bulk on transport characteristics, the crystallinity of the active layer was varied by changing the thin-film fabrication technique, such as spin-coating and drop-casting. The crystallinity of the thin-films was verified through GIXD measurements. Finally, implications of the interface and semiconductor layer on charge transport were analyzed various modeling equations. The modeling equations were designed by combining possible physical phenomena taking place at the metal/SC interfaces and inside the SP thin-film.

For the analysis of in-plane transport properties, OFETs, in bottom-gated top contact device architecture, were fabricated. Since of dielectric's surface energy and the presence of dipoles on it significantly affect the thin-film morphology[102–104], therefore, for comparative analysis, the OFETs were fabricated on a bare and self-assembled monolayer (SAM) treated substrates (Si/SiO_2). Highly oriented thin-films of PBTTT-C14, fabricated by friction transfer technique, were selected as a model to fabricate channel of OFETs. The thin-films were annealed at 100 – 200 ℃ on both types of substrates and corresponding morphological variations were investigated through grazing incident X-ray diffraction (GIXD) and X-ray diffraction (XRD). Further, the effect of thin-film morphology on transport properties was examined by fabricating OFETs and comparing their field-

effect mobility and mobility anisotropy. It was observed that on the bare substrate $\mu_{\parallel}$ and $\mu_{\parallel}/\mu_{\perp}$ increased with annealing at the lower temperature (up to ~120 ℃) and decreased beyond this temperature. On the other hand, on SAM treated substrates, $\mu_{\parallel}$ consistently increased with annealing temperature and $\mu_{\parallel}/\mu_{\perp}$ followed the opposite trend. Besides, increased backbone-orientation in the thin film was observed after annealing at a higher temperature (~180 ℃) as characterized through polarized UV-Vis absorption spectroscopy. Since absorption spectra can reveal the extent of macromolecular orientation only but not the film crystallinity, which is crucial for a clear understanding of the transport characteristics. Therefore, interface and annealing condition-dependent variations in the $\mu_{\parallel}$ and $\mu_{\parallel}/\mu_{\perp}$ of the thin-films were analyzed by considering their XRD and GIXD patterns. Ultimately a pertinent model regarding macromolecular arrangement was proposed in light of the obtained results from temperature and interface dependent electrical and optical characterization of the thin-film.

4.2. Experimental Section

4.2.1 Materials and Methods of OFETs

4.2.1.1 Materials and Thin-film fabrication:

PBTTT with M_W > 50 kDa (product code: 753971-250MG) was purchased from Sigma Aldrich. Dehydrated hexamethyldisilazane (HMDS) was supplied by Sigma Aldrich. The other solvents were purchased from Wako Chemicals. The substrates (glass, Si, and Si/SiO_2) were cleaned by following the procedure discussed in chapter 2. They were ultrasonicated in acetone, isopropanol, and ultrapure water for 10 minutes each. Further, the substrates were annealed for 1 h by keeping them on a hot plate with temperature fixed at 150 ℃. For SAM treatment using HMDS, cleaned and dried substrates were covered with HMDS droplets and placed in a closed glass petri dish and

kept at 50 ℃ for 1 h followed by sonication in dehydrated chloroform for 5 min and annealing at 150 ℃ for 1 h. The polymer pellet was prepared according to the method reported earlier.[62] Thin films of PBTTT-C14 were cast using friction transfer technique on the desired substrates by drawing the polymer pellet on it at a constant speed of 50 mm/min with a fixed squeezing load of 3 kgf/cm^2, as schematically shown in **Figure 2.4**.

4.2.1.2 OFET fabrication and characterization:

OFETs were fabricated in the bottom gate top contact device architecture on heavily p-doped silicon substrates with 300 nm thick thermally grown SiO_2 at top which acted as the dielectric layer. For OFET fabrication and optical measurements, the thin-films were annealed at various temperatures for 3 – 5 min in Argon-atmosphere and subsequently cooled slowly to room temperature. Further, to complete the OFETs, Gold electrodes were thermally evaporated on the friction transferred PBTTT thin film (deposition rate ~ 1.5 Å/s under the pressure of ~ 10^{-6} Torr). A nickel shadow mask with channel length and width of 20 μm and 2 mm, respectively, was utilized to pattern the source and drain electrodes, digital image for masking is shown in Figure 2.6. For electrical characterization, the OFETs were kept under vacuum (pressure ~10^{-2} Torr) and the transfer and output characteristics were measured with Keithley 2612 two-channel source-meter.

4.2.1.3 Thin Film Characterization:

The electronic absorption spectra of thin films coated on glass substrate were measured by dual-beam spectrophotometer (JASCO V-570). A Glan-Thompson prism was placed between sample and the illumination source in order to measure polarized absorption spectra. The out-of-plane XRD (θ-2θ) measurements were performed with Rigaku X-ray diffractometer whereas the in-plane GIXD (φ-2θχ) measurements were conducted through Rigaku smart lab diffractometer. For both the XRD and GIXD measurements, the samples were coated on Si substrates and some of them. It is to be noted that for the absorption spectroscopy, XRD, and GIXD measurements

corresponding to the OFETs fabricated on HMDS treated substrates, the corresponding glass or the Si substrates were also treated with HMDS.

4.2.2 Materials and Methods of OSDs

4.2.2.1 Materials

Regioregular P3HT, super dehydrated chloroform, and super dehydrated chlorobenzene were purchased from Sigma Aldrich, Japan, and were used as received. Other cleaning solvents acetone, isopropanol was supplied by Wako Chemicals, Japan.

4.2.2.2 Fabrication of Thin Film and OSDs

The solution of P3HT in chloroform (with concentration1.5% w/w) and in chlorobenzene (with concentration 0.2% w/w) were prepared to fabricate the spin-coated and drop-casted films respectively. Glass substrates patterned with bottom electrode were utilized for the device fabrication. Drop-cast films were prepared by placing the P3HT solution on the substrates and they were covered with petri-dish for slow solvent evaporation. The spin-coated films were prepared by placing the solution on the substrate fixed on the chuck of the spin-coater, followed by spinning it at 800 rpm for 5 s and then 1500 rpm for 40 s. The film fabrication step was conducted under ambient conditions and then they were dried by keeping them under vacuum. Further, the films were annealed at 150 ℃ for 20 min in the argon atmosphere. Then the films coated on the substrate were masked such that the top electrode can be deposited orthogonal to the bottom electrode. The top electrode was thermally evaporated under high vacuum (pressure ~10-6 Torr). OSDs were fabricated with the cross-sectional area of 4 mm^2. Thermally evaporated Al and Au electrodes were utilized for making Schottky and Ohmic contacts, respectively. In some OSDs AlO_X interlayer (**Figure 4.1**) was deposited before depositing a thick Al electrode at top. In such cases, at first a thin (of desired thickness, where the thickness value shown by the thickness monitor was taken

into consideration) Al layer was thermally evaporated on the P3HT layer, under high-vacuum followed by exposing them to ambient condition for ~ 1 hour to the oxidation of Al. Further, ~60 nm thick Al was thermally evaporated above AlO_X layer to complete the OSD fabrication.

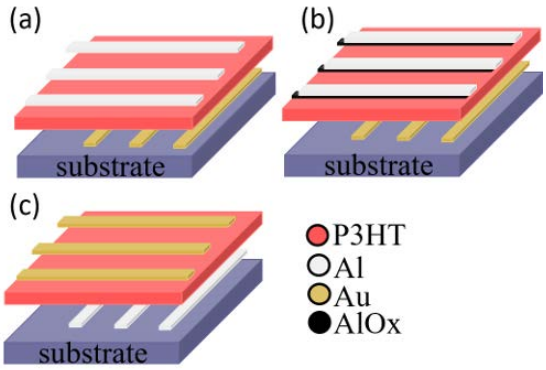

Figure 4.1 Schematic representation for architectures of Schottky diodes fabricated with Al as top-contact pristine (a) and with AlO_X interlayer (b) and with Al as bottom-contact. Reproduced with permission[68]. Copyright (2019) American Institute of Physics.

4.2.2.3 Device and Thin Film Characterization

Current versus voltage measurements of OSDs were conducted under vacuum through the same source-meter (Keithley 2612) as discussed above but in this case, only one channel was utilized. Out-of-plane XRD and in-plane GIXD measurements of the spin-coated and drop-casted films were carried by Rigaku X-ray diffractometer and Rigaku smart Lab respectively. Photoelectron spectroscopy (XPS and UPS) measurements were conducted through the Shimadzu Kratos Axis-Nova spectrometer. Al Kα excitation source was used at pass energy of 80 eV with the energy resolution of 1000 meV. For the XPS and UPS characterization, 10 nm thermally evaporated Al on top of the P3HT layer was utilized as the sample, which was also kept in an ambient atmosphere for 1 h before the measurement. The samples were etched by Ar^+ ions (for different intervals between 0-60 s) in order to obtain the depth profiling in XPS and UPS measurements. The AFM measurement of similarly prepared films on Si substrates was performed through a scanning probe microscope (JSPM5200, Shimadzu, Japan).

4.3. Results and Discussion

4.3.1. Role of Bulk and Interfacial Morphology on Vertical Charge Transport

4.3.1.1 Electrical Performance of OSDs with Varying Architecture

The electrical measurements of OSDs fabricated in different architectures shown asymmetric J –V characteristics, **Figure 4.2**. The J –V characteristics clearly reveal the higher current flow in forward bias and around four orders of lower current in reverse bias which can be attributed to the formation of Schottky barrier at the Al/P3HT interface. The thermionic emission model as given in Eq. (2.3) was proposed for inorganic Schottky diodes but and has been widely accepted for organic semiconductors as well[64–67]. η and J_0 are device parameters representing ideality factor and reverse saturation current density respectively. J_0 and η were calculated from the intercept and slope of ln$J$ –V plot and the RR was calculated from the ratio of current flowing through the device under forward and reverse bias at the same applied potential. All of the calculated parameters for different device structures are summarized in Table 4.1. A perusal of **Figure 4.2** and Table 4.1 clearly corroborates that RR of the OSDs having pristine Al as top-contact is similar to that of devices in Al as bottom-contact.

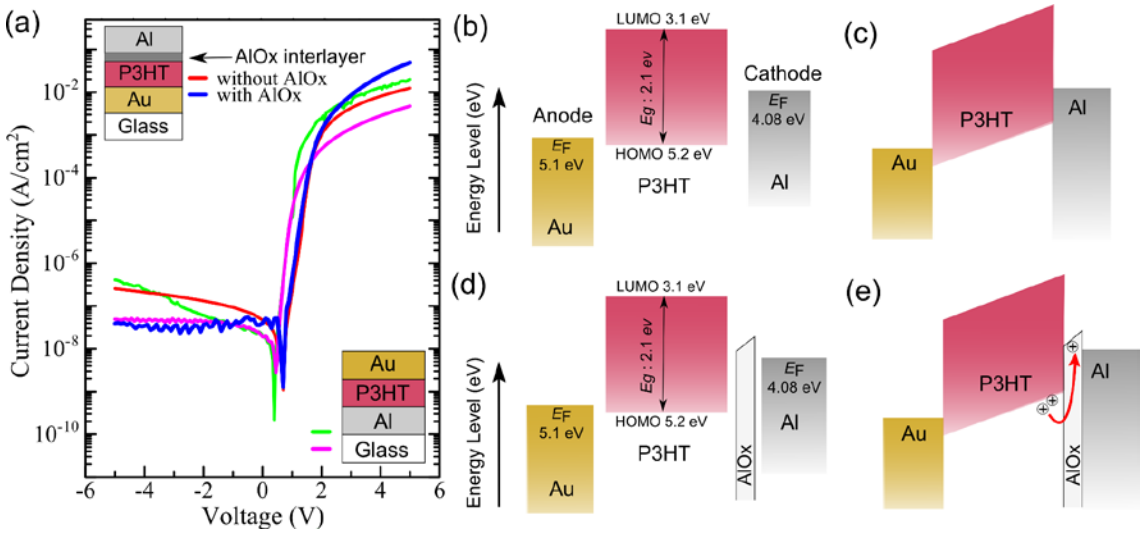

Figure 4.2 J – V characteristics of the Schottky diodes (a) along with the device architectures shown in the inset. Energy band diagram for the different layers in the OSD with pristine Al and AlO_X interlayer (nano-

structures of AlO_X with 10 nm thick Al) at the Schottky contact (b, d) and Energy band diagram of the corresponding OSDs in forward bias ($V_a > V_{bi}$) (c, e). Energy levels are shown with respect to the vacuum level. Reproduced with permission[68]. Copyright (2019) American Institute of Physics.

Table 4.1 Average electronic parameters calculated for the OSDs fabricated in different device architectures (Figure 4.1). More than three independent devices were fabricated and analyzed in each case. All the OSDs were fabricated with spin-coated P3HT films except when it is mentioned. Reproduced with permission[68]. Copyright (2019) American Institute of Physics.

Diode configuration	**Ideality Factor (η)**	J_0 (A/cm^2)
Al-top contact (without AlO_X)	3.56 ± 10.80%	(2.57 ± 1.7)×10^{-12}
Al-top contact (with 10 nm AlO_X)	3.19 ± 12.29%	(5.99 ± 3.1)×10^{-12}
Al-bottom contact	2.29 ± 18.85%	(5.33 ± 1.6)×10^{-12}
Al-top contact (with 10 nm AlO_X) (P3HT drop-casted)	7.19 ± 7.86%	(9.27 ± 5.79)×10^{-9}

Significant improvement in the rectification ratio was obtained in the case of 10 nm AlO_X layer at top, clearly visible in **Figure 4.3**. This enhancement in RR can be attributed to the optimal interfacial band structure at the Schottky contact. Upon oxidation, the work function of Al decreases at the Schottky interface,[110] which favors the holes transport under forward bias but blocks in the reverse direction leading to enhancement in the ON-current (I_{on}), while OFF-current (I_{off}) is reduced more effectively. Low RR was evidenced with Al at bottom, where the formation of a thin oxide layer at the interface in ambient condition naturally occurs. Therefore, the effect of device architecture on the performance of OSDs was also probed in detail. Since the pristine Al surface cannot oxidize fully, therefore, an arbitrary state 'x' is considered to represent the oxidized Al layer (AlO_X) and its corresponding work-function was drawn less than that of pristine Al in **Figure 4.2** (d,e). The oxide growth saturates towards depth due to limited penetration of aerial oxygen irrespective of the exposer time and for Al it has been reported to be ~2 nm. Nonetheless, the work-function of AlO_X also starts to increase with aging.[110] Considering both of these points, the interfacial Al layer was exposed to the ambient condition for 1 h. Schematic representation of

the energy band structure of the OSDs with and without AlO_X layer has been shown in Figure 2(b-e). The increasing trend of the work-function of AlO_X towards the depth of the interfacial layer represents the lesser oxidized region. To construct the energy band diagram, the work functions of Au and Al, along with the energy of the highest occupied molecular orbital (HOMO) and lowest unoccupied molecular orbital (LUMO) of P3HT was taken from the values reported in the literature.[112,113] After the inception of SPs and demonstration of their semiconducting behavior, Schottky model based on thermionic emission developed for the silicon has been quite frequently used straightway for the organic diodes to deduce electronic parameters like ideality factor.[114] Standard Schottky model predicts that the depletion region should be confined to the small part of the film thickness. However, in OSDs, low carrier concentration leads to the extension of the depletion region throughout the film thickness (≈100 – 200 nm). This poses a limitation to the straightforward use of the thermionic emission model for OSDs leading to the proposal of other models like metal-insulator-metal (MIM) without having a partial depletion region.[100,115–117] This was further validated through the small value of experimentally calculated Richardson constant (2×10^{-9} $Acm^{-2}K^{-2}$) obtained by temperature-dependent J –V characteristics of OSDs, which is far from the typical value of Richardson contestant (120 $Acm^{-2}K^{-2}$) used for inorganic semiconductors.[65,118] Keeping these arguments in mind, energy band diagram for the OSD as shown in **Figure 4.2** (c, e) was constructed taking the MIM model into consideration. Contrary to OSDs fabricated with Al top contact as shown in **Figure 4.1**, J –V characteristics were noisy and suffered reproducibility issues with Au top contact as shown in **Figure 4.2** (a). The non-repetitive J –V curves in combination with pronounced leakage current for OSDs with Au top contact could be attributed to the diffusion of heavy and hot Au atoms into the soft polymeric semiconductor film. Which is supposed to cause large Au–thiol chemical interaction and damaged Au/P3HT interface.[119,120]

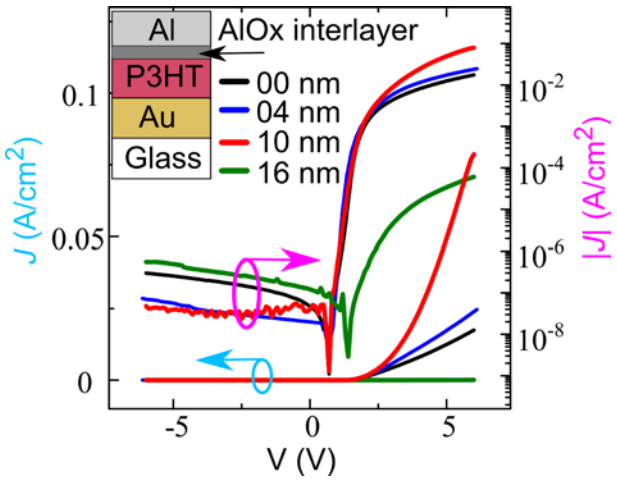

Figure 4.3 Comparative representation of *J–V* characteristics for the OSDs with varying thickness of interfacial AlO_X layer, the corresponding device architecture is shown in the inset.

4.3.1.2 Characterization of AlO_X Interfacial Layer

In order to visualize the surface morphology of the optimized AlO_X interlayer (10 nm), AFM measurement was conducted and the obtained images are shown in **Figure 4.4**. From the perusal of **Figure 4.4** (a, b), small islands of Al (≈ 100 nm wide) was clearly observed from the height image with root mean square (RMS) surface roughness of ≈ 2.61 nm. Minimization of surface energy might have assisted this formation of islands during thermal evaporation since the metal deposition occurs as a tiny cluster of atoms. Moreover, less freedom to rearrange themselves on the polymer surface could also have assisted the formation of such a nanostructured interface. This can be understood by the fact that when a similar or even lower thickness of Al was coated on bare Si/SiO_2 substrate in the same deposition condition, continuous Al film was observed as shown in **Figure 4.5.** Despite the fact that the islands partially cover the underneath polymer layer (≈30%), the RR for the OSDs with AlO_X interlayer was found to be dramatically improved compared to that of devices without AlO_X interlayer with Al at top (**Figure 4.2** (a)). As already stated, oxidation of the exposed surface of Al continues up to around 2 nm along depth, but the nano-islands of AlO_X play a dominant role in the device performance due to an increase in their effective surface area.

When the Al surface is exposed to air, a large amount of oxygen is also expected to be trapped on the oxide surface. The empty levels of the adsorbed oxygen are filled by the electron tunneling from the underlying Al atom, concomitantly a charge double layer is formed with a negative charge on the external surface as schematically shown in **Figure 4.4** (c). It can also be noticed that the resultant electric field due to this charge double layer assists the hole transport in the forward direction; however, it hinders the hole transport with Al at bottom contact as shown in **Figure 4.4** (c). Thus it can be said that the optimum thickness of AlO_X interlayer is controlled by three parameters, which are the optimum coverage of the underlying polymer layer, the presence of pristine Al below the AlO_X layer for charge double layer formation, and the distance of the charged double layer from the underlying polymer layer for optimum effect on the charge transport. It is worth to note here that during optimization, the thickness shown by the Quartz crystal monitor was considered without commenting on its continuity but considering its effect on the *J –V* characteristics. Therefore, from now on, this thickness value will be used for the device nomenclature.

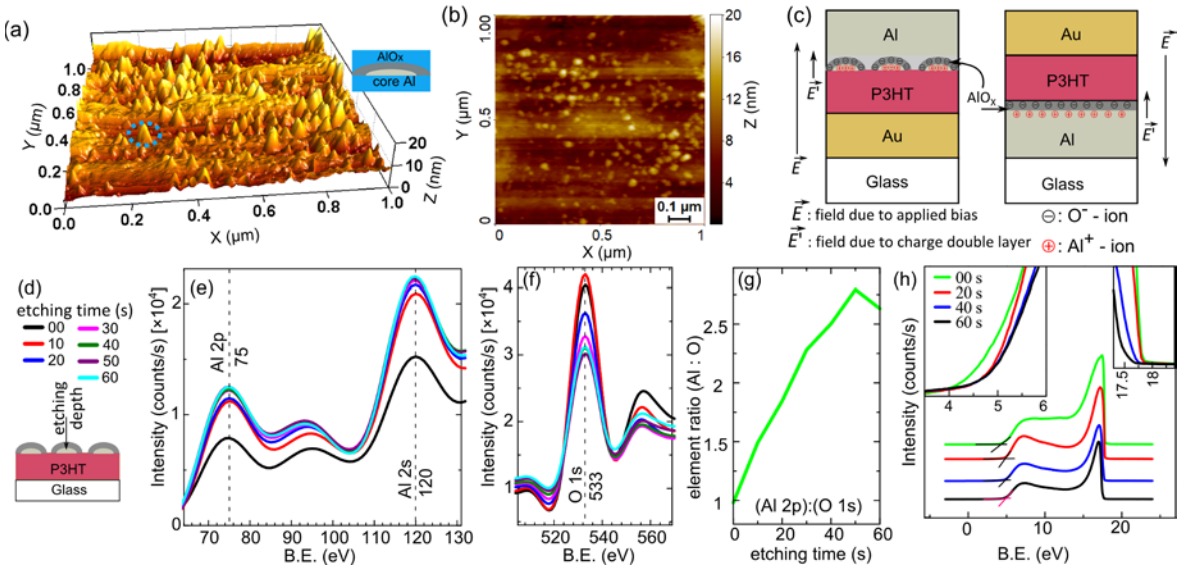

Figure 4.4 AFM images of the 10 nm oxidized Al deposited on top of the spin-coated P3HT film exhibiting height (a) and phase (b) images. Inset of (a) depicts the schematic for partially oxidized Al-island. (c) Schematic representation for the formation of charge double layer due to adsorbed oxygen on AlO_X layer. (d) Schematic representation of sample geometry used for the depth profiling of AlO_X interlayer by XPS

and UPS and the inset shows the set of ligands corresponding to graphs in (e , f). Narrow scan elemental XPS spectra before etching and with Ar^+ ion etching from top for (e) Aluminum and (f) Oxygen. (g) Probing AlO_X interlayer represented in terms of ratio of percentage contribution in XPS spectrum corresponding to Al 2p and O 1s as a function of etching time. (h) UPS spectral profile for AlO_X island layer on P3HT before and after Ar^+ ion etching (Incident beam energy (He–I) = 21.2 eV). Sample geometry for this was also the same as shown in the (d). Reproduced with permission[68]. Copyright (2019) American Institute of Physics.

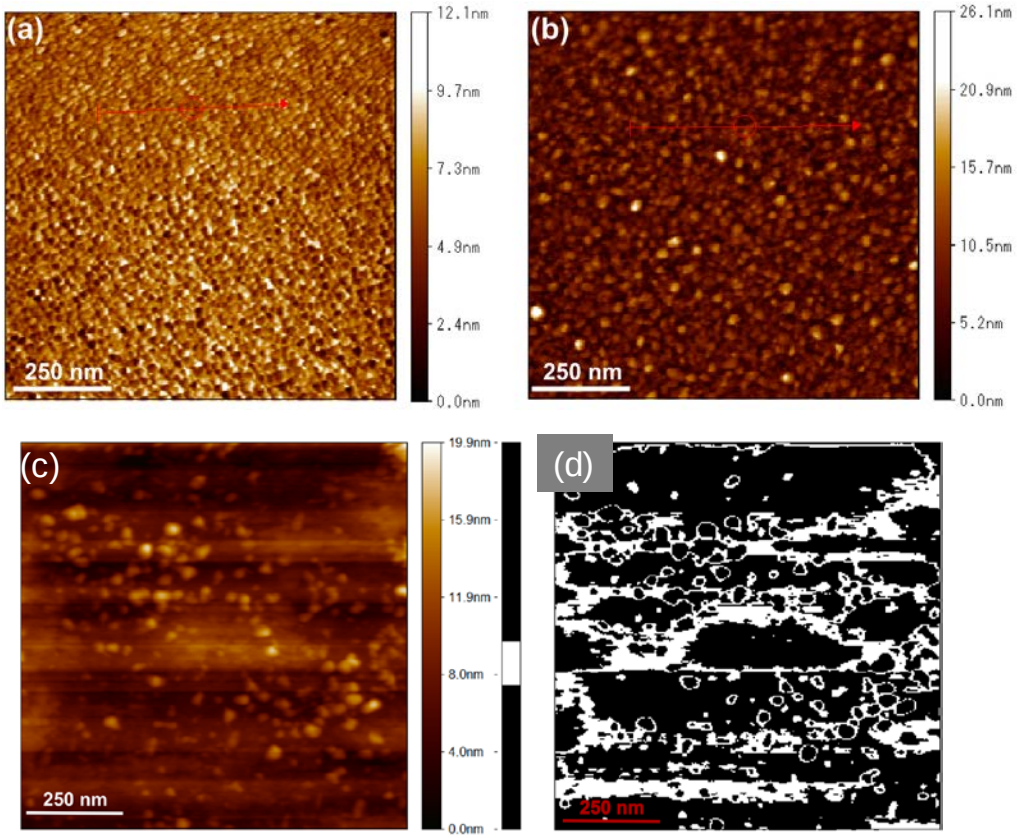

Figure 4.5 AFM topography of the 4 nm (a) and 10 nm (b) Al deposited on the SiO2 substrates and oxidized in air. AFM images of the 10 nm oxidized Al deposited on top of the spin-coated P3HT film (c) and the corresponding distribution map (d). From (d) the coverage of P3HT film by interfacial AlO_X layer was estimated to be ≈30%.

To have in-depth insight into the interfacial chemical composition and electronic band structure of AlO_X on P3HT; XPS and UPS depth profiling was conducted with the sample schematic shown in **Figure 4.4** (d). XPS spectrum for the sample is shown in **Figure 4.4** (e, f) exhibiting peaks corresponding to Al 2p, Al 2s, and O 1s at binding energy of 75 eV, 120 eV, and 533 eV, respectively. A similar XPS profile for the wide scan of AlO_X layer generated upon various

oxidized and pure Al surface has also been reported by Gupta et al.[121] Presence of the weak XPS peak corresponding to C 1s along with peaks corresponding to O 1s and Al 2p is attributed to the presence of hydrocarbon impurity at the surface of oxidized Aluminum (AlO_X).[122] Complete disappearance of C 1s peaks just after 10 s of Ar^+ ion etching from top further supports the presence of hydrocarbon impurity.

It can be seen in **Figure 4.4** (e, f) that as a function of etching time (i.e. sample depth), there is an increase in the counts of Al 2p and concomitantly decrease in the O 1s atomic peak indicating a relative reduction in the extent of AlO_X. In XPS measurement, the incident source was of very high energy (1486.6 eV), therefore, the obtained signal contains the corresponding peaks of elements present up to ~ 5 – 10 nm depth.[40] Since the height of Al-islands are also of the same order (rms surface roughness ≈ 2.61 nm as observed in AFM measurement), therefore, change in the ratio of the XPS signal corresponding to Al 2p and O 1s was considered for probing the AlO_X layer formed after the aerial oxidation of Al. A perusal of **Figure 4.4** (g) clearly corroborates that initially, Al 2p to O 1s ratio was increasing, which corresponds to a decrease in oxygen contents with depth followed by a decrease after 50 sec of etching. Although only limited penetration of oxygen is possible inside the Al islands, some amount of oxygen is always present in the underlying polymer film due to its processing under ambient conditions, therefore, Al 2p peak intensity decreases after a certain depth but that of O 1s saturates which might be the reason for the decrease in Al to O ratio (**Figure 4.4** (g)).

The sample was further subjected to UPS measurement before and after consecutive Ar^+ ion etching from the top and the obtained results are shown in **Figure 4.4** (h). In the UPS spectra at the secondary electron cutoff position (corresponding spectra magnified in right inset), the binding energy of the sample decreases with depth. They were found at the binding energy of 17.81 eV, 17.81 eV, 17.65 eV, and 17.45 eV for 0 s, 20 s, 40 s, and 60 s of sample etching, respectively.

The valence band edge (represented by the intersecting lines) shifts towards higher energy with an increase in sample etching and was found to be 4.24 eV, 4.83 eV, 4.90 eV, and 4.90 eV for samples before and after 20 s, 40 s, and 60 s of etching, respectively. These shifts correspond to an increase in work-function of the AlO_X interlayer, which has been shown schematically in the band diagram after inserting the AlO_X layer in **Figure 4.2** (e).[40]

4.3.1.3 Characterization of semiconducting polymer Thin-film

Encouraged by the implication of device architecture on the performance of OSDs, where bottom Au and top Al contacts having 10 nm of nanostructured AlO_X layer gave the best device performance, the effort was directed to examine the influence of film crystallinity and macromolecular conformation on the performance of OSDs. To accomplish this, OSDs were fabricated in the optimized device architecture using thin films of P3HT prepared by spin-coat and drop-cast methods as described in the experimental section. The obtained $J-V$ characteristics along with device architecture used are shown in **Figure 4.6** (a) and the device parameters obtained by fitting the linear region of $\ln J-V$ characteristics are summarized in **Table 4.1**. It can be clearly seen that in spite of having similar device architecture and fabrication conditions, OSDs having spin-coated thin films exhibited improved device performance as compared to the case of drop-casted thin films.

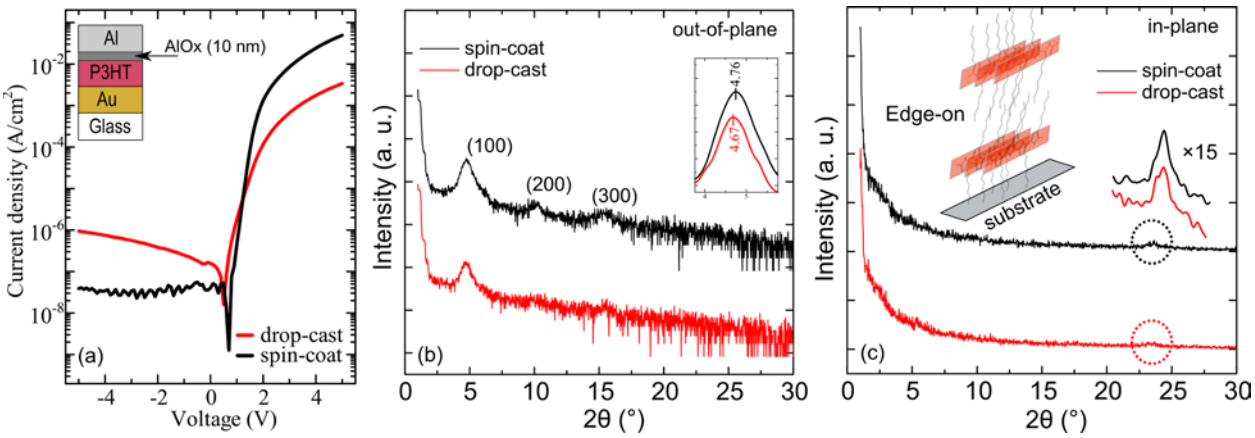

Figure 4.6 *J -V* characteristics of OSDs fabricated using thin films of P3HT prepared by spin-coated and drop-casted films along with the device structures shown in the insets. (b) Out-of-plane and (c) in-plane GIXD pattern for spin-coated and drop-casted films of P3HT. Inset of (b) shows the enlarged view of (100) peak in both the cases. Inset of (c) shows 15 times resolved peak of the in-plane GIXD pattern and schematic representation for edge-on conformation of P3HT molecules. Reproduced with permission[68]. Copyright (2019) American Institute of Physics.

In order to understand such a marked difference in the device performance for the P3HT thin films fabricated by spin-coat and drop-cast methods, these films were subjected to out-of-plane and in-plane GIXD measurements. As can be seen in **Figure 4.6** (b) that in out-of-plane mode GIXD spectra, all the peaks corresponding to the lamellar-stacking of the alkyl side-chains appeared at 4.75°, 9.97° , and 15.29°. The *d*-spacing calculated from the difference between *100* and *200* peak positions was found to at 16.95 Å and 17.34 Å for the spin-coated and drop-casted P3HT films, respectively. The relative left shift in *100* peak position ($2\theta \approx 0.1°$) in drop-casted film also corresponds to an increase in *d*-spacing, i.e., the alkyl side-chains are more stretched as compared to the spin-coated one which causes hindrance in out-of-plane charge transport. From **Figure 4.6**(b), it can be also be clearly seen that all the peaks corresponding to the lamella formation via alkyl side-chain stacking were more pronounced up to higher orders for the films prepared using spin-coating compared to the drop-casting method. In general, the position of the peak represents the lamellar stacking distance, whereas the sharpness of the peak is associated with

the crystallinity and grain size. Therefore, it can be concluded that in the present case the spin-coated films possessed a higher degree of crystallinity as compared to that of the drop-casted films. Moreover, in the in-plane GIXD pattern, the presence of peak corresponding to π-π stacking at $2\theta = 23.17°$ and absence of any (*h00*) peaks related to alkyl-stacking in both of the films clearly suggest the edge-on conformations of the polymeric backbones on the substrate as schematically shown in the inset of **Figure 4.6**(c). Since the thickness of the films prepared by both the methods were of the same order (≈ 200 nm), it is worth mentioning here that films prepared by spin coating by two-successive spin speed were of high crystallinity as compared to the drop-casted method. The edge-on conformation and high-crystallinity of the spin-coated samples prepared here is attributed to the low spin-speed (800 rpm) in combination with relatively higher polymer concentration (2% w/w), which gave enough time to the macromolecules to obtain thermodynamically favored conformation as reported earlier.[22,23,31,123] At the same time, spin-coated films possess high film uniformity with minimum surface roughness due to the absence of the coffee ring effect, the drop-casted film possesses non-uniform thickness distribution. Due to presence of coffee ring effect, the dissolved polymer molecules move towards the edges of the drop-casted area, which leads to inhomogeneity in the dried film.[124,125] When the top electrode is deposited, diffusion of metal in the pinholes leads to a short resistive path resulting in increased I_{OFF} as depicted in **Figure 4.6** (a). Since devices were processed in ambient conditions, therefore, due to high surface roughness at the metal/organic interface, the effective surface area for gas-adsorption would increase leading to an increase in interfacial trap states.[126] These effects could have played a dominant role in the relatively hampered device performance of OSDs with drop-casted film. Other than these, the bulk resistance due to SCLC, which depends on film crystallinity also affect the $J-V$ characteristics. It is also worth mentioning here that unlike planar devices such as OFET, charge transport in the vertical devices like diodes and solar cells ideally takes place in

the out-of-plane direction, therefore, a good crystallinity in the transverse direction is required. Otherwise, when the charge carrier enters the bulk of semiconducting thin film it has to spend a larger amount of time inside the film due to an increase in intermolecular hopping and scattering centers at grain boundaries before being collected at the other electrode.[93] The charge carriers residing in the organic film creates space charge, applying repulsive force for further charge injection, and with an increase in charge carrier inside the film the resultant repulsive force increases, interpreted as SCLC.

4.3.1.4 Analytical Modeling

In the ideal OSDs, under forward bias there should not be any injection barrier but practically it is present due to the formation of charge accumulation region in the organic thin-film near Ohmic contact and the charge carriers overcome this barrier through thermionic emission effect.[101,116] Therefore, under forward bias, $J-V$ characteristics of an OSD is analyzed through comparing it with the approximated thermionic emission model as written in Eq. (4.1) (approximation of Eq. 2.3 for $V > (3kT/q)$).[64–67]

$$J = J_0 \left[\exp\left(\frac{qV}{\eta kT}\right)\right] \tag{4.1}$$

Using Eq. (4.1), J_0 is obtained by extrapolating the linear part of the ln$J-V$ plot to $V = 0$ V, where the value of η is obtained from its slope with the help of Eq. (4.2). The deviation of η from the ideal value (= 1) can be attributed to the occurrence of tunneling phenomena or scattering of the charge carriers due to presence of trap states in the devices, and the interfacial non-uniformity also contributes in it.[64,97]

$$\eta = \frac{q}{kT}\frac{\mathrm{d}V}{\mathrm{d}(\ln J)} \tag{4.2}$$

The above discussed model was originally proposed for inorganic devices, thus before generalizing it for organic devices, it should be scrutinized extensively. In this regard, calculation of η is an appropriate example which can be calculated from either of the two linear regions with distinguishable slopes present in the ln$J-V$ plots as shown in Figure 2.9. The higher slope value (present at lower voltage region) can be considered to obtain lesser value of η. To verify the calculated physical parameters, corresponding regions on linear scale $J-V$ plot were analyzed as shown in the inset of Figure 2.9. It is clear that in higher voltage region, the thermionic emission phenomena is reflected through non-linear region in $J-V$ plot (red color segment in the inset of Figure 2.9), the device parameters obtained from this region are summarized in Table 4.1. Furthermore, to understand the correlation between the device parameter and whole electrical characteristic, a thorough analysis of $J-V$ curve has to be done through a general physical equation, which can incorporate all physical phenomena occurring in the device.

In OSDs, various types of physical phenomena occur in different regions of the OSD as discussed in the earlier section, and their contribution in overall $J-V$ characteristic is also a function of voltage. Therefore, modeling of whole $J-V$ characteristic will be more reliable compared to considering the linear part of ln$J-V$ plot, only. As discussed above, in this regard, there are some reports where the overall $J-V$ analysis has been done by integrating the sectional analysis using different physical phenomena or by considering one phenomenon and neglecting other.[96–101] For instance, in one of the analytical model proposed by Blom and coworkers, the effects of bulk and injection contact were combined as drift (bulk effect) and diffusion (interface effect) contributions as a function of the applied voltage.[101] The clear demarcation between the contributions of bulk and interface at certain applied voltage can lead to underestimation of their relative effect in some cases. Moreover, the device structure-dependent deviation of the physical model from practical

electrical characteristics still remains a challenge.[99,106,107] However, being an implicit function of voltage, the effective contribution of the physical phenomena in overall $J-V$ characteristic varies with applied bias. Which is also non-uniformly distributed in the whole device architecture as a function of regional/local non-linear resistances such as R_C and R_B. Thus, drawing a boundary between the effects of physical phenomena on voltage-scale/device-architecture seems improper since they can occur simultaneously. To address this issue, $J-V$ characteristic of any two-terminal device can be interpreted through the following relation Eq. (4.3),

$$J = \frac{V}{R_{\text{total}} \times a} \tag{4.3}$$

$$\text{Where, } R_{\text{total}} = R_C + R_B$$

Here a is the cross-sectional area of the device and R_{total} is the total resistance present in the device at any point of time and it consists of two parts, R_C and R_B. R_C and R_B are not simply Ohmic but they are also generated due to various non-Ohmic physical phenomena occurring in the device, such as band-bending due to charge accumulation, SCLS, trap states, etc.[101] At lower forward bias ($V_a < V_{bi}$), the injection barrier at the Ohmic contact (here it is Au-P3HT contact) and at higher bias ($V_a > V_{bi}$) mainly SCLC governs the device $J-V$ characteristics. Scattering center present at grain boundaries and trap states are exponentially distributed from contact towards the bulk and they contribute in both R_C and R_B, as shown in **Figure 4.7** (a – c). Thus, all the phenomena should be combined to frame an analytical model equation where Ohmic and non-Ohmic part of R_{total} can be divided into three parts i.e. resistance due to nonlinear injection barrier, resistance due to SCLC, and R_{series} (Ohmic loss throughout the device). Since trap states and scattering centers hamper the overall hole mobility thus their effect can be considered as R_{series} and the effect of charge double layer can also be accounted in the same. The R_C and R_B are nonlinear function of voltage drops across contact and bulk of the OSD and in-situ measurement of these voltage distributions are not

possible but macroscopic current density is same at any bias. Henceforth, interpreting their effect with current as a forcing function would provide an ease to interpret the effect of bulk and contact in one simple equation. Following the previous report, the analytical modeling equation is written with current as forcing function as Eq. 4.4.[127] For comparative study, some of the other equations as listed in **Table 4.2,** were also used to analyze the $J-V$ characteristics.[64,127]

$$V = \frac{\eta kT}{q}\ln\left(\frac{J}{J_0}+1\right) + \sqrt{\frac{8L^3J}{9\epsilon\epsilon_0\mu}} + JR_{\text{series}} \tag{4.4}$$

Where, R_{series} is taken in the unit of 'Ωcm^2'.

L is the effective channel length which is the film thickness in the present case (≈ 200 nm). ϵ and μ are relative permittivity and effective hole mobility with approximate values of 3 and 3×10^{-4} $cm^2V^{-1}s^{-1}$, respectively were taken from previous reports.[128,129]

The experimental $J-V$ characteristics and the simulated models with different modeling equations (Table IV) are depicted in **Figure 4.7**. The constant/s J_0/(and η when kept constant) was/were obtained from the linear region (with the lower slope as shown in Figure 2.9) of the $\ln J-V$ plot. The best fit of the experimental characteristics in different device architecture were analyzed through the simulated model based on Eq. 4.4 and the corresponding obtained device parameters are summarized in **Table 4.2**. Hence Eq. 4.4 can be considered as general model equation for the OSDs. As already discussed, J_0 and η should be calculated from the low slope region of $J-V$ plot.

Table 4.2 The set of equations[64,127] followed for the comparative analysis of the experimental J –V characteristics. Reproduced with permission[68]. Copyright (2019) American Institute of Physics.

Equation type	Equation in mathematical form with J as forcing function; V(J)	Fitting Parameters
Thermionic Emission (Th. Em.)	$V = \frac{\eta kT}{q}\ln\left(\frac{J}{J_0}+1\right)$	η
Th. Em. + SCLC + Ohmic Loss(R_{series}); (constant η)	$V = \frac{\eta kT}{q}\ln\left(\frac{J}{J_0}+1\right) + \sqrt{\frac{8L^3J}{9\epsilon\epsilon_0\mu}} + JR_{series}$	R_{series}
Th. Em. + SCLC	$V = \frac{\eta kT}{q}\ln\left(\frac{J}{J_0}+1\right) + \sqrt{\frac{8L^3J}{9\epsilon\epsilon_0\mu}}$	η
Th. Em. + SCLC + Ohmic Loss(R_{series}); [Eq. 6]	$V = \frac{\eta kT}{q}\ln\left(\frac{J}{J_0}+1\right) + \sqrt{\frac{8L^3J}{9\epsilon\epsilon_0\mu}} + JR_{series}$	η, R_{series}

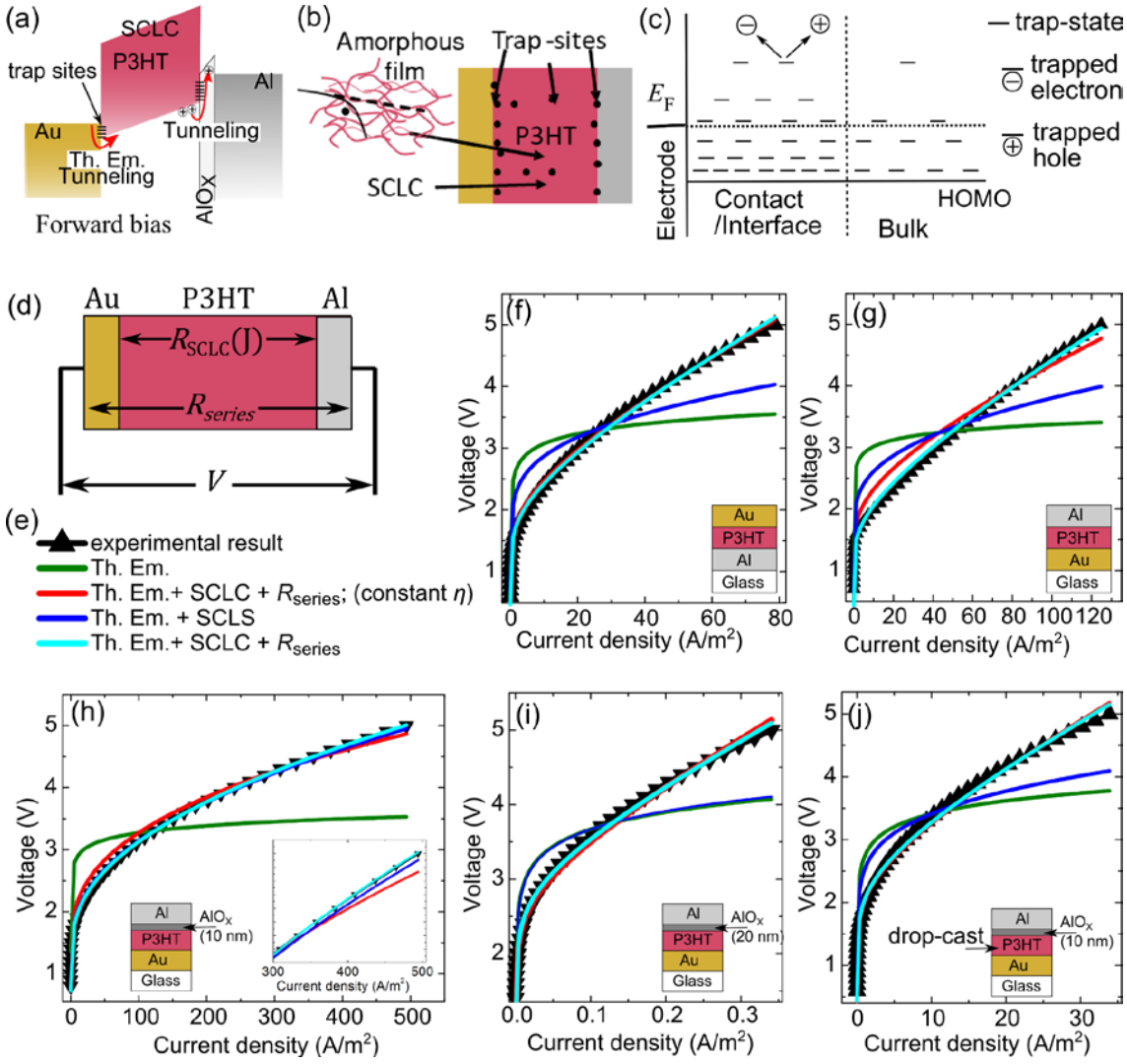

Figure 4.7 (a) Energy band structure of the OSD (Al/P3HT/Au) in forward bias ($V_a > V_{bi}$) along with the physical different phenomena occurring in its different parts, (b) schematic representation for effect of trap sites in charge-scattering (the broken line represents the actual path of charge flow in absence of scattering center or trap sites) and (c) Schematic illustration for exponential distribution of trap states in the device. (d) Schematic representation for occurrence of linear and nonlinear (function of J) resistance in different parts of the OSD (Al/P3HT/Au) and (e) set ligands for the experimental and fitted $J-V$ characteristics (f - j) the corresponding equations are written in Table 4.2. Inset of (h) represents the magnified part of fitted data at higher voltage. The device structures are shown in the corresponding insets and all the OSDs were fabricated with spin-coated P3HT films except when it is mentioned. Reproduced with permission[68]. Copyright (2019) American Institute of Physics.

Table V gives the understanding about the influence of metal/organic interfaces on the overall device resistance. The calculated value of R_{series} decreased by one order of magnitude in the case of 10 nm AlO_X interlayer as compared to that having only Al to make Schottky contact. On the other hand, it was of the same order in case of the bottom Al electrode and top Al electrode without AlO_X layer. In forward bias, at $V_a > V_{bi}$, space charge is being formed in the organic layer, which triggers tunneling of the charge carriers through the AlO_X layer. In addition to this, when charge double layer is closer to the film, tunneling will be speedup due to favorable Coulombic interaction. At the same time, modified interfacial band structure due to AlO_X layer will be improving the charge transport when it is near to the organic layer. The nanostructured AlO_X island layer also improves the effective contribution of the charge-double layer, however, with an increase in its thickness (for instance 16 nm), R_{series} increases due to the buried oxide layer which is ineffective to support forward charge transport. This is also reflected in the obtained device parameters from fitted plot R_{series} (Table V) and the corresponding RR (Table 4.1, 4.3). Precise observation in the case of 10 nm AlO_X interlayer shows that the experimental data is well fitted by the model without the inclusion of R_{series}, however, the inclusion of R_{series} provides better fit (Figure 4.7(i)), unlike other cases where the deviation is distinguishable due to the presence of comparatively lower R_{series}. This reduction can be attributed to the favoring effective field due to the charge double layer (Figure 4.3 (c)) and vice-versa is true for the case of Al as bottom contact. Therefore, the effect of device architecture on the physical phenomena occurring inside is justified.

Table 4.3 Set of device parameters (η and R_{series}) obtained by fitting the experimental J –V characteristics of different devices using Equation 4.6. All the OSDs were fabricated with spin-coated P3HT films except when it is mentioned. Reproduced with permission[68]. Copyright (2019) American Institute of Physics.

Device Structure	Ideality factor (η)	R_{series} ($\Omega.cm^2$)
Al (bottom contact)	2.84 ± 3.6%	844.6 ± 31.5%
Al (top contact) 0 nm AlO_X	2.95 ± 4.2%	113.6 ± 42.8%
Al (top contact) 10 nm AlO_X	3.54 ± 18.2%	32.7± 32.7%
Al (top contact) 16 nm AlO_X	15.63 ± 36.7%	3.39×10^5 ± 42.8%
Al (top contact) 10 nm AlO_X (P3HT drop-casted)	5.85 ± 24.5%	728.7 ± 30.0%

4.3.2 Role of Interface and Thin-film Morphology to In-plane Charge Transport

4.3.2.1 Characterization of Orientation in Friction Transferred PBTTT

To fabricate a highly oriented thin film of PBTTT by friction transfer method, the film casting parameters such as drawing speed, squeezing load, and substrate temperature, play dominant roles and they were optimized. It was found that low squeezing load and slow drawing speed resulted in high orientation, therefore, they were fixed to the be 3 kgf/cm^2 and 5 cm/min, respectively, while optimum substrate temperature was found to be 80 ℃ as shown in **Figure 4.8** (a). Polymer orientation of the fabricated thin films was characterized by polarized electronic absorption spectroscopy and the results are shown in **Figure 4.8** (b, c). Since the transition dipole moment for the optically induced π-π* transition is aligned along the polymer backbone, therefore, linearly polarized light is absorbed maximum, when the polarization direction was aligned parallel (∥) to the polymer backbone orientation resulting in the highest value of absorbance (maximum absorption value at λ_{max}), which decreases by moving the polarization direction away from the backbone orientation direction and reaches to the minimum, when they were orthogonal (⊥) to each other. The optical anisotropy was calculated in terms of the dichroic ratio (DR) = $A_{\parallel}/A_{\perp}$,

where $A_{\parallel}$ and $A_{\perp}$ are maximum absorbances of the respective absorption spectra with polarized light ∥ and ⊥ to the polymer orientation direction. The maximum absorbance along the drawing direction confirmed the orientation of polymers to be along the drawing direction. THE average DR of the as-prepared films was found to be 10.95 ± 0.89. The DR further increases and reaches up to 27.62 ± 2.46 upon annealing above LC temperature 180 °C.[31,130] Annealing temperature-dependent DR is summarized in **Table 4.4**. It is worth noting that DR values were not significantly affected by the surface energy of the substrate. Such high DR values correspond to the highly anisotropic and unidirectional arrangement of the PBTTT backbones in the thin film with the order parameter (OP) of ~ 0.9, where $OP = (DR - 1)/(DR + 2)$. The OP signifies the extent of orientation and its minimum (0) and maximum (1) values correspond to the ideal isotropic and ideal anisotropic films, respectively. It can be clearly seen that absorption spectra in ⊥ direction do not have any vibronic shoulders (featureless) as shown in **Figure 4.8** (b), which clearly reflects that ⊥-spectrum is originated from the randomly lying polymeric chains, withstanding chain twisting/folding or entanglement, having large distribution in conjugation lengths. A similar observation was also reported by Brinkmann group for highly oriented thin films of poly(3-hexylthiophene). [131] The absorption peak (λ_{max} for ⊥-absorption spectrum) of the as-cast film appeared at 508 nm, which was blue-shifted by 52 nm after annealing to 180 °C because ordered polymeric chains serve as a template for remaining randomly lying polymers in the film when alkyl side chains recrystallize during the cooling process, leading to a simultaneous increase in $A_{\parallel}$ and decrease in $A_{\perp}$.[31,105,132] Consequently upon annealing the DR increased. Moreover, it was also observed that annealing beyond 180 °C the magnitude of increment in DR was smaller.

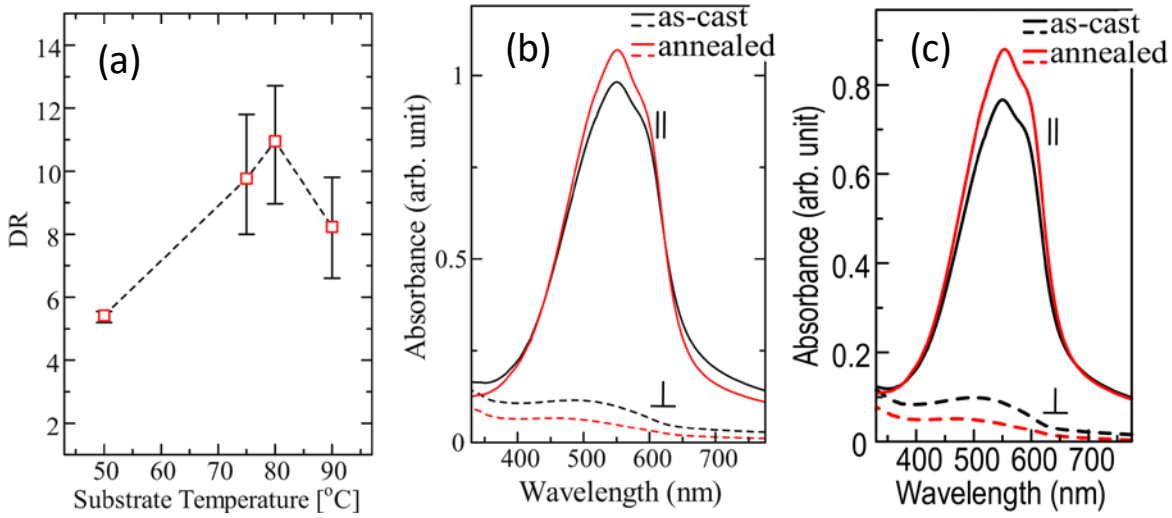

Figure 4.8 (a) Effect of substrate temperature on orientation, when the stage speed and load were kept constant to 50 mm/min and 3 kgf/cm^2, respectively. Polarized absorption spectra of the as-cast and annealed (180 °C) friction transferred PBTTT film and cast on (b) bare glass substrate and (c) HMDS treated substrate. Reprinted with permission from[70]. Copyright 2020 American Chemical Society

Table 4.4. The values of charge transport parameters and optical anisotropy obtained for friction transferred PBTTT films cast on different substrates and annealed at different temperatures with $V_{DD} = -80$ V; $V_{GS} = -40$ to + 40 V (for bare SiO_2) or − 80 to + 40V (for HMDS treated SiO_2)). The thin films were cast with optimized coating parameters as shown in Figure 1. All the statistics were calculated with three or more separate films. Reprinted with permission from[70]. Copyright 2020 American Chemical Society.

Annealing temperature (°C)	$\mu_{\parallel}$ (cm^2 V^{-1} s^{-1})	$\mu_{\perp}$ (cm^2 V^{-1} s^{-1})	$\mu_{\parallel}/\mu_{\perp}$	$I_{on}/I_{off} \approx$ (along backbone orientation)	**DR**
		bare SiO_2			**bare glass**
as-cast	0.008 ± 0.0003	(4.68 ± 0.2) × 10^{-5}	< 200	10^3	10.95 ± 0.89
120	0.026 ± 0.04	(2.70 ± 0.16) × 10^{-5}	~ 10^3	10^5	15.96 ± 1.25
150	0.023 ± 0.002	(4.64 ± 2.9) × 10^{-5}	~ 500	10^5	19.37 ± 0.71
180	0.017 ± 0.005	(5.24 ± 1.3) × 10^{-5}	> 200	10^4	27.62 ± 2.46
200	0.012 ± 0.003	(1.04 ± 0.23) × 10^{-5}	~ 200	10^4	24.17 ± 2.85
					HMDS treated
		HMDS treated SiO_2			**glass**
200	0.334 ± 0.03	0.016 ± 0.004	> 20	10^6	22.6 ± 1.66
					22.7

In general, orientation techniques using shear force, DR is susceptible to molecular weight (M_W) of the SPs and falls with an increase in M_W due to chain folding and entanglement.[11,32,133,134] Using high temperature mechanical rubbing technique, high DR was obtained for lower M_W

PBTTT samples but with increase in M_W > 45 kDa the orientation decreased below 10.[134] Whereas the present study was conducted with commercially available high M_W PBTTT (M_W > 50 kDa, Sigma Aldrich), which resulted in high DR, thereby suggesting that this technique can efficiently orient high M_W polymers too, which is one of the important requirements for the facile charge transport.

4.3.2.2 Characterization of Interface Driven Conformational Changes

To analyze the macromolecular arrangement, in-plane GIXD and out-of-plane XRD measurements were performed as per the geometry shown in **Figure 2.12**. It can be seen from **Figure 4.9** (a – c) that in case of the samples as-prepared and annealed below LC temperature for friction transferred PBTTT-C14 thin-film on bare oxide substrate, series of diffraction peaks (*h00*) corresponding to alkyl-stacking is observed for in-plane GIXD and are absent in the out-of-plane GIXD. This clearly reflects that macromolecules in the as-prepared thin films adopted face-on orientation and upon annealing above the LC temperature (130-140 °C),[31] where side chain melts to reorganize the crystalline domains leading to the observed conformational change in the thin film. A closer look at XRD patterns reveals that peak intensity of (*h00*) decreases in the in-plane and increases in out-of-plane mode with the increase in the annealing temperature ≥ 150 °C, while just opposite trend was observed for the (*010*) diffraction peak corresponding to π- π stacking. These results clearly suggest that there is a gradual change in the conformation of PBTTT-C14 from face-on dominated to edge-on dominated depending on the annealing temperature. It is worth to note here that at 200 °C, the intensity of the (*h00*) diffraction peak is observable in both of the in-plane and out-of-plane modes, therefore, partly the PBTTT macromolecules can be considered to recrystallize in edge-on conformation. Moreover, since (*010*) diffraction peak did also not diminish completely in the out-of-plane mode at 200 °C, it suggests that some face-on oriented crystallites also remained in the film.[135] Results of in-plane GIXD and out-of-plane XRD of as-cast and annealed films of

friction transferred PBTTT on HMDS treated substrate as shown in **Figure 4.9**(d – f), clearly revealed the almost complete transformations from the face-on to edge-on after annealing the thin-films ~ 200 °C. The diffraction peaks (h00) of lamellar stacking of alkyl side chain were observed in the out-of-plane mode and diffraction peak (0k0) related to π-π stacking was observed in the in-plane mode.

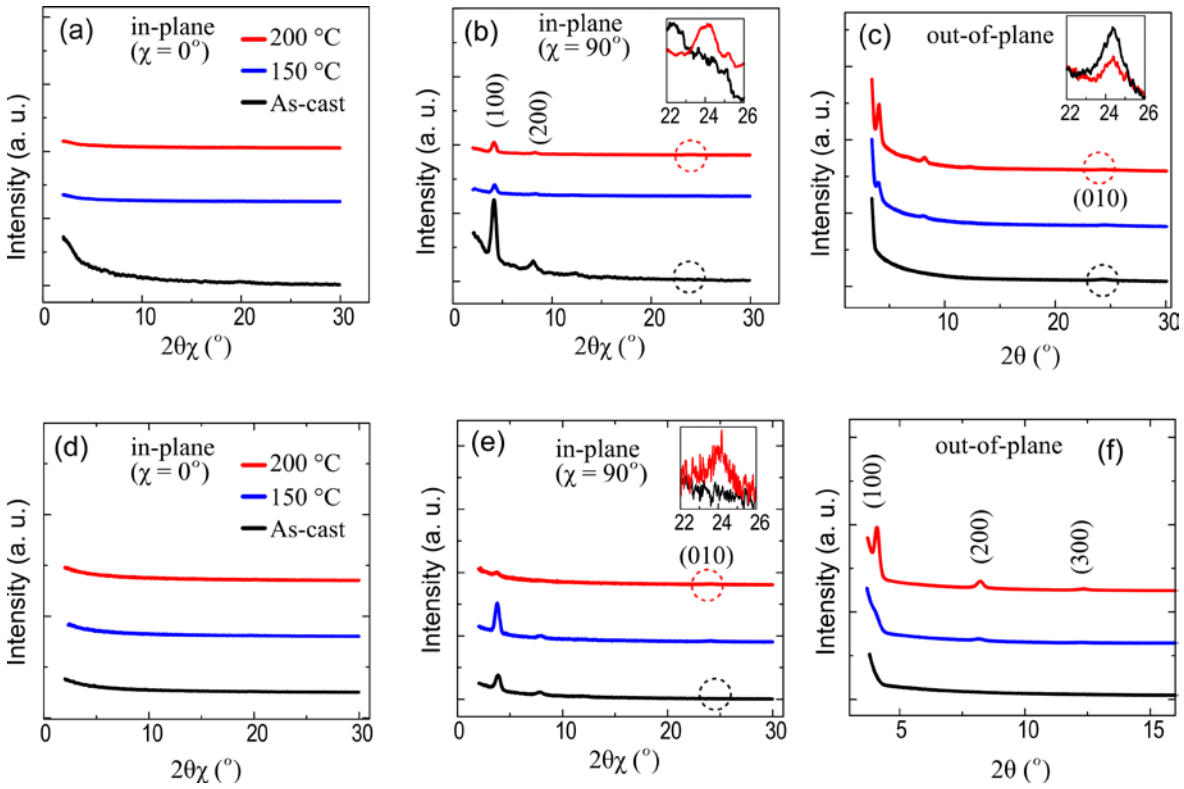

Figure 4.9 The in-plane GIXD profile of the friction transferred PBTTT film as-cast and annealed at different temperatures on the bare oxide substrate with the scattering vector (a) parallel (χ = 0°) and (b) orthogonal (χ = 90°) to the drawing direction. (c) Out-of-plane XRD pattern of the films. In-plane GIXD profile of friction-transferred PBTTT films on HMDS-treated Si substrates as-cast and annealed at different temperatures with a scattering vector (d) parallel and (e) orthogonal to the drawing direction and (f) their out-of-plane XRD pattern. Reprinted with permission from[70]. Copyright 2020 American Chemical Society.

4.3.2.3 Comparative Analysis of Interface Driven Electrical Performance

To examine the impact of these highly oriented thin films of PBTTT on the charge transport, OFETs were fabricated on bare SiO_2 substrates in the bottom gate top contact geometry as schematically shown in the inset of **Figure 4.10** (a). The saturation μ and other electronic

parameters were extracted from the transfer curves ($I_{DS} - V_{GS}$) as described earlier.[123] The OFETs were fabricated with the thin films as-cast and annealed at different temperatures (100 °C to 200 °C) and their transport characteristics are shown in **Figures 4.10** (a – b) along with summarization of the device parameters in Table 4.4. A perusal of the anisotropic optical and electrical characteristics clearly reveals that the μ did not increase consequently with the increase in DR. In spite of exhibiting the maximum DR for the films annealed to 180 °C, the $\mu_{\parallel}$ was lower compared to films annealed at lower temperatures (Table 4.4). Consistent increment in the $\mu_{\perp}$ was also observed with annealing beyond LC temperature, which can be attributed to increase in edge-on oriented macromolecules in the thin film as shown in **Figure 4.10** (c). However, more than two orders of $\mu_{\parallel}/\mu_{\perp}$ was maintained even after annealing to 200 °C, which confirms the presence of face-on oriented crystallites near the dielectric interface as this has been well examined that in edge-on oriented PBTTT thin-films, $\mu_{\parallel}/\mu_{\perp}$ lies within one order of magnitude,[11,136] and these results are consistent with the observation made by XRD measurements. Therefore, we anticipate that during annealing, the evolution of edge-on conformation starts from the top surface of the film and the templating process to be similar to the case of orientation templating in the ribbon-phase of PBTTT,[137,138].

PBTTT is a well-known material to exhibit high μ on SAM treated substrates because of low surface energy.[38,130] However, because of the high contact angle of the octadecyltrichlorosilane (OTS) treated surface,[139,140] it was difficult to have uniformly adhered film while squeezing the PBTTT pellet. Therefore, to examine the origin of this low μ and reasons behind the incomplete transformations of macromolecular conformation from face-on to edge-on, treatment of SiO_2 surface was performed using a mild SAM agent, HMDS that results into relatively lower contact angle in comparison to OTS treated surfaces. Such a difference in surface energy between SAM treated SiO_2 substrates affects the interplay between molecule–substrate and molecule–molecule

interactions in their own way. However, following the assumptions and results by Kline et al.,[38] we believed if this behavior was originated because of the oxide surface, HMDS treated surface would be a suitable model for the investigation pertaining to the nature of macromolecular conformation adopted as a function of the annealing temperature. At the same time, average $\mu_{\parallel}$ of PBTTT films on HMDS treated SiO_2 reaches up to 0.33 $cm^2V^{-1}s^{-1}$ and $\mu_{\perp}$ to 0.016 $cm^2V^{-1}s^{-1}$ (see Table 4.4 and **Figure 4.10** (d, e)), which is comparable to other reported mobility values for PBTTT on OTS substrates and it has also been well demonstrated by Umeda et al. that decreasing surface energy of the substrates resulted in an increase in the μ of PBTTT based OFETs.[11,141]

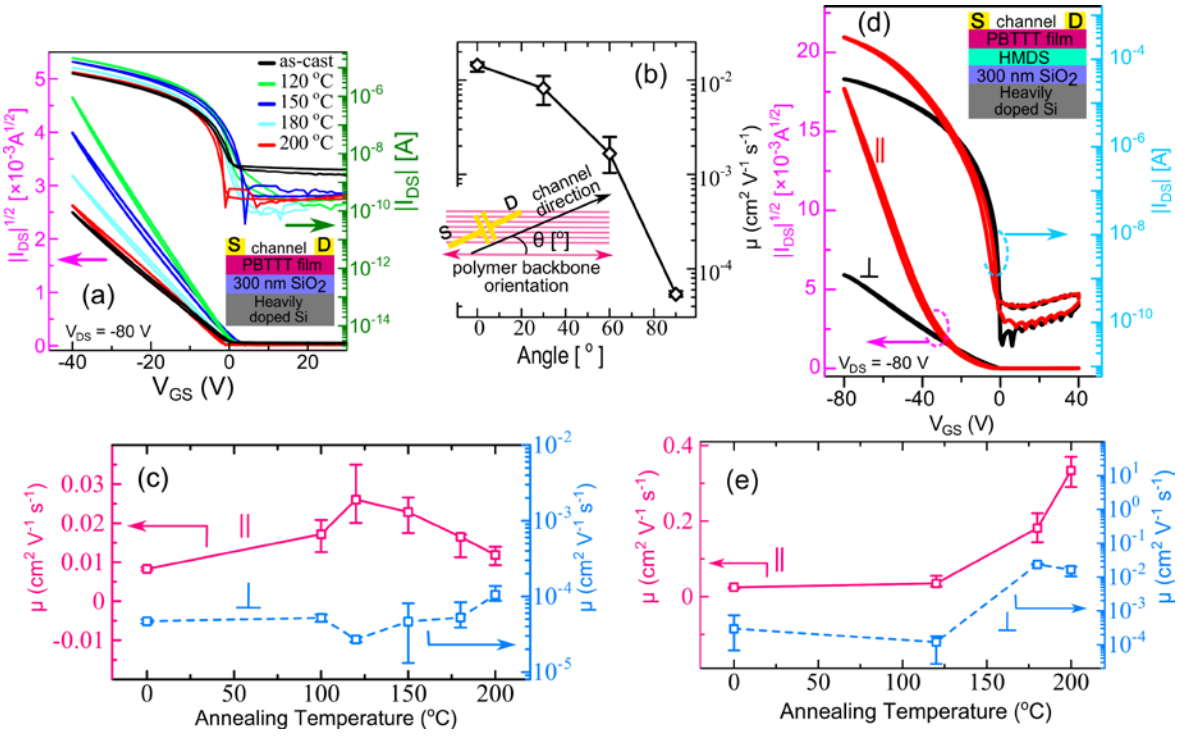

Figure 4.10 For friction transferred PBTTT-C14 cast on base oxide substrates: (a) representative transfer curves of OFETs fabricated with films annealed at different temperatures, (b) trend of μ for thin films annealed at 180 °C with varying orientation of channel relative to backbone orientation direction, and (c) variation in μ for friction-transferred PBTTT-C14 on the bare oxide substrate and annealed at different temperatures; all the OFETs were fabricated with device structure as shown in the inset (a). For friction transferred PBTTT-C14 cast on HMDS treated substrates: (d) representative transfer curves for OFETs with channels parallel and perpendicular to the backbone orientation direction fabricated with the thin films annealed at 200 °C, (e) statistical variation in μ for the thin films cast on HMDS-treated SiO_2 and annealed at different temperatures; the OFETs were fabricated with the device architecture as shown in the inset (d). Reprinted with permission from[70]. Copyright 2020 American Chemical Society

4.3.2.4 Modeling Variation in Interface and Annealing driven macromolecular arrangement

Results obtained pertaining to the differential nature of macromolecular conformations attained depending on the nature of surface and annealing temperature along with evidences from anisotropic charge transport of OFETs, a plausible charge transport mechanism for the friction transferred PBTTT thin films have been proposed, which is schematically shown in the **Figure 4.11**. Structure of the friction transferred thin film was compared to slipped stacks or brickwork like film structure.[142] In such structure, complete face-on orientation may lead to high $\mu_{\parallel}$ compared to mixed-phase of face-on and edge-on. In the former case, the charge carriers traverse through the inter-layer of π-π stacking, when a high resistance path (between polymer chains or domains) is encountered. However, in the latter case, the charge carriers face additional high resistance path due to presence of alkyl chains between two layers. Hence, for the efficient charge transport, the thin films should possess an optimum macromolecular orientation and conformation.

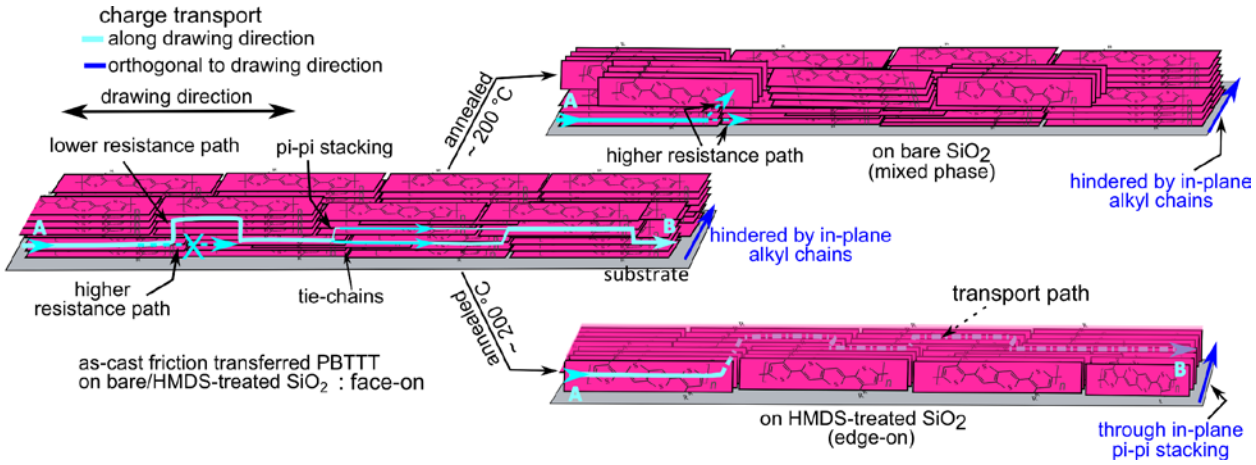

Figure 4.11 Schematic representation for the cross-sectional view of the charge transport mechanism in as-cast and annealed friction-transferred PBTTT-C14 thin films and substrate's surface energy-dependent macromolecular conformation possessed by the thin films. In the bottom right part of the figure, only the bottom layer of the film is represented for better understanding. Reprinted with permission from[70]. Copyright 2020 American Chemical Society

This agrees well with the films annealed to 120 °C (on bare SiO_2), which possessed higher orientation compared to as-cast thin films and complete face-on conformation of macromolecules. In the case of HMDS treated SiO_2, annealing the film beyond LC temperature (~ 200 °C) led to almost complete edge-on oriented thin film, resulting into higher in-plane $\mu_{\parallel}$. Along with conformational transformation at 200 °C, increment in domain size, extensively reported as intrinsic nature of PBTTT to form large domains, when the thin-films annealed beyond LC temperature on SAM treated substrate, should also be taken into consideration to interpret the increase in $\mu_{\parallel}$.[38,130] Interestingly, in the optimized conditions for films annealed to 120 °C on bare silicon oxide, $\mu_{\parallel}$ and $\mu_{\parallel}/\mu_{\perp}$ exceeded some previous reports for the same material in which the thin films possessed edge-on conformation and the dielectric substrates were given SAM treatment.[81,143] Therefore, the improved $\mu_{\parallel}$ and $\mu_{\parallel}/\mu_{\perp}$, in this case, can solely be attributed to the higher orientation.

4.4. Conclusion

In this chapter, the effect of interfacial layer and the thin-film morphology on in-plane and out-of-plane charge transport have been discussed. To analyze the effects on out-of-plane/vertical charge transport, Organic Schottky diodes (OSDs) were fabricated with varying metal/SC interfacial properties, and the morphology of the SP thin film was also varied by opting different casting techniques. Though there are previous reports which deal with the physical phenomena of the organic diodes by analyzing the experimental observations through theoretical models. For the analysis of in-plane transport properties, OFETs, in bottom-gated top contact device architecture, were fabricated. Since of dielectric's surface energy and the presence of dipoles on it significantly affect the thin-film morphology, therefore, for comparative analysis, the OFETs were fabricated on bare and self assembled mono-layer (SAM) treated substrates (Si/SiO_2). Highly oriented thin-

films of PBTTT-C14, fabricated by friction transfer technique, were selected as a model to fabricate channel of OFETs. Ultimately a pertinent carrier-transport mechanism was proposed in light of the obtained results from temperature and interface dependent electrical and optical characterization of the thin-film.

Chapter 5: Environmentally Sustainable Approaches for Fabricating Organic Electronic Devices

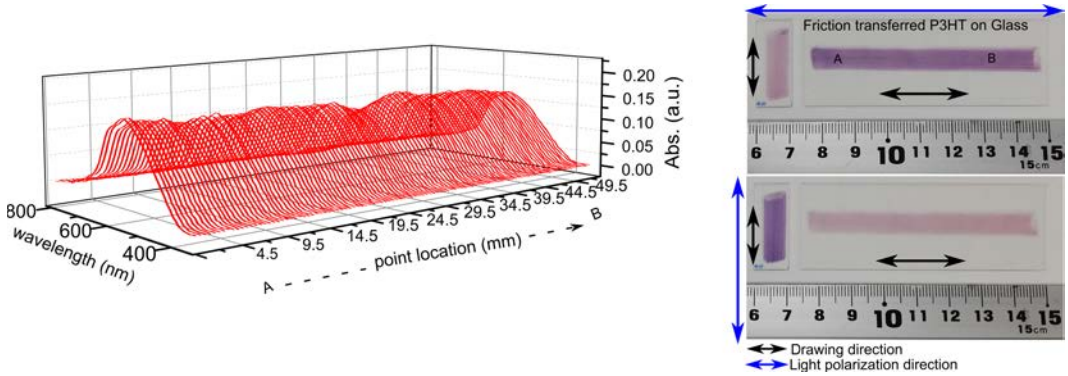

➢ **N. Kumari**, M. Pandey, S. Nagamatsu, S. S. Pandey "Orientation of Semiconducting Polymers via Swift Printing and Drawing Techniques for High Performance Organic Electronic Devices". (in preparation for *Organic Electronics*)

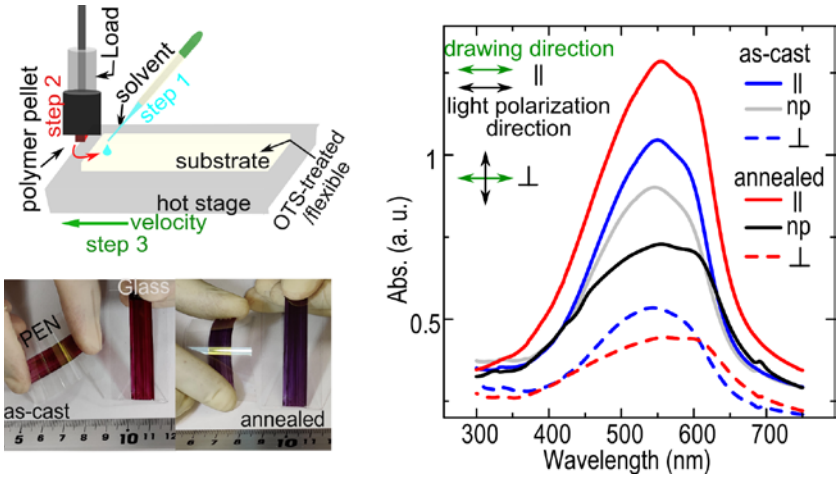

➢ **N. Kumari**, M. Pandey, S. Nagamatsu, M. Nakamura, S. S. Pandey "Solvent assisted Friction Transferred edge-on Oriented Polymer Thin-film Organic Field Effect Transistors". (Submitted to ACS Appl. Mater. Interfaces)

5.1 Introduction

Inexpensive and simple processing techniques have made the organic semiconductors a promising contender for electronic device applications. The past decade has witnessed significant scientific efforts to improve the charge transport characteristics of the organic semiconductors by tuning their chemical structure or by varying the film fabrication techniques in order to enhance the macromolecular ordering. Since SPs offer better solution rheology and compatibility with solvent-free drawing techniques compared to small molecular organic semiconductors, they may be more suitable for large scale fabrication. Besides, due to quasi-one-dimensional nature of SPs, their backbone orientation and self-assembly in the thin films through various techniques were extensively explored to improve the optoelectronic characteristics of the devices [11]. Although good solubility of SPs in common halogenated solvents led to the low-cost research and development at laboratory scale, the serious health and environment hazards cannot be avoided at large scale roll-to-roll fabrication. Apart from this, controlling device to device variation, at large scale, is also essential. Therefore, to overcome these challenges, efficient solution processes or solvent-free techniques need to be explored[11,70,81].

Herein comparative study of two such techniques, floating-film transfer method (FTM) and friction transfer (FT), for large area thin film fabrication and their various applications is being reported. In FTM, by placing one drop (~10 – 15 μL) of SP solution on an orthogonal liquid substrate solid floating film is obtained which can be stamped on any desired substrate without causing chemical or mechanical damage to the underlying layers if present[34,60]. Recently, facile fabrication of large area ribbon-shaped SP thin-film was demonstrated by controlling the film expansion direction through a custom made slider, as shown in **Figure 2.3**[144]. Utilizing friction transfer technique, considerable macromolecular orientation anisotropy and its impact on charge transport characteristics of the SP thin-films have been demonstrated[11]. In Chapter 4, almost one

order of increment in field effect mobility (μ) of friction transferred PBTTT thin film has been demonstrated, by tuning the surface energy of the dielectric interface[70]. In this chapter, both the techniques, FTM and FT, have been considered to demonstrate environmentally sustainable and economical ways for large area polymer-film fabrication, and the uniformity in their charge transport characteristics was also analyzed by fabricating organic field effect transistors (OFETs) with different parts of the film. By exploiting the advent of FTM, OSDs and organic memristors were also fabricated in the layer by layer structure, which further may lead to the fabrication of high-density 3D integrated circuits via horizontal and vertical stacking on the same substrate. The uniformity in both planer and vertical device performance for large area thin-films cast through both techniques validates their feasibility towards large scale application. For the FTM based thin-films one order enhancement in μ (up to 0.03 $cm^2V^{-1}s^{-1}$) was also obtained compared to conventional spin-coated thin films (~ 0.004 $cm^2V^{-1}s^{-1}$). On the other hand, FT thin-films exhibited a lower value of μ; however, a considerable increase in it was observed by optimizing the channel length. Generally, friction transfer technique is not suitable for thin-film fabrication on SAM-treated/smooth surfaces, and mostly the fabricated thin-film possess face-on conformation and through very high temperature annealing edge-on conformation can be obtained which is not compatible with low temperature fabrication processes[63,70]. Therefore, with some improvisations in the existing friction transfer technique, an adequate solution was provided to this challenge. In the improvised friction transfer technique, a drop (~10 µl) of chlorobenzene was put at the interface of PBTTT-C14 pellet and OTS-treated substrate. The as-cast thin-film possessed edge-on conformation and even on low temperature annealing (~150 °C) the stacking improved significantly as characterized through GIXD, XRD. The thin films were also subjected to polarized absorption and polarized Raman spectroscopies and the obtained results pointed out towards increase in conjugation length which was attributed to the probability of backbone straitening of

less soluble PBTTT-C14. Under optimum conditions, $\mu \sim 0.5$ cm^2 V^{-1} s^{-1} was obtained. Although the little amount of chlorobenzene is less hazardous, less toxic solvents like toluene and different other polymer-solvent combinations were also explored to show the generality of this technique.

5.2 Experimental Details

5.2.1 Materials and Substrate Preparation:

Regioregular poly(3-hexylthiophene) P3HT and PBTTT-C14 were purchased from Sigma Aldrich and used without any further purification. Anhydrous chloroform and chlorobenzene were also supplied by Sigma Aldrich. OFETs were fabricated in bottom gated top contact architecture on heavily p-doped Si (as gate) having thermally grown SiO_2 (100 nm / 300 nm) at top as dielectric. For substrate cleaning and/or SAM treatment the procedure as discussed in Chapter 2 was followed. OSDs were fabricated on ITO coated glass, which was etched to obtain 1 mm wide ITO strips as the bottom electrode, following the procedure as mentioned in Chapter 2. Memristors were fabricated on the glass substrate patterned with 2 mm wide thermally evaporated Al strips as bottom contact.

5.2.2 Thin-film fabrication:

To fabricate ribbon-shaped thin films by FTM, a drop of P3HT solution in anhydrous chloroform (2% w/w) was placed at the interface of slider and liquid substrate (pure ethylene glycol at room temperature ~ 27 ℃). For friction transfer, the pellet of P3HT or PBTTT-C14 were fabricated following the steps as described in Chapter 2, and for film fabrication, they were squeezed and drawn against the hot substrates. Friction transferred thin-films of P3HT were fabricated with an optimized stage speed of 50 mm/min, squeezing load of 15 kgf/cm^2, and substrate temperature of 80 ℃, Figure 2.4 can be looked at to recognize these casting parameters. The thin-films of PBTTT-C14 were fabricated by solvent assisted friction transfer technique at

optimized stage speed of 1000 mm/min, squeezing load of 3 kgf/cm^2, and substrate temperature of 85 ℃. The thin films were fabricated, using the conventional friction transfer setup (Figure 2.4), while a little drop (~ 3 µl) of anhydrous chlorobenzene was placed at the interface of polymer pellet and the OTS-treated substrates.

5.2.3 Device fabrication:

OFETs were fabricated in three structure i) one layer ribbon shaped P3HT film, fabricated by FTM, was stamped on OTS treated Si/SiO_2 (100 nm) substrate and for solvent evaporation, they were annealed at 120 ℃ for 15 min under Argon atmosphere, ii) friction transferred P3HT films were coated on bare Si/SiO_2 (100 nm) substrates and were utilized as-cast, and iii) solvent-assisted PBTTT-C14 thin films were fabricated on OTS treated Si/SiO_2 (300 nm) substrates and annealed at ~ 140 ℃ for 30 min under Argon atmosphere followed by slow cooling. OFETs' fabrication was completed by evaporating ~50 nm thick Au layer under high vacuum, which was patterned as the source and drain electrodes using Ni shadow masks with 2 mm channel width and varying channel length.

OSDs were fabricated on ITO patterned glass substrate in three structures by i) stamping 5 layers of ribbon-shaped P3HT FTM films followed by annealing at 120 ℃ for 15 min, ii) casting one layer of friction transferred P3HT and used as-cast, and iii) casting one layer of friction transferred P3HT then stamping one layer of P3HT FTM films above it followed by annealing at 70 ℃ for 15 min. Above these thin films 10 nm AlO_X interlayer (as discussed in Section 4.2.2) followed by ~70 nm Al as top contact was deposited, orthogonal to the bottom electrode. All the experiments were performed in ambient conditions except thin-film annealing and device characterization.

Organic memristors were fabricated in layer-by-layer structure of three different SPs. On glass substrate patterned with 2 mm wide Al stripes as the bottom electrode. At first thin films were spin-

coated with SP solution (1% w/w P3HT or PTB7 in anhydrous chloroform, or 1.5% w/w PBTTT in anhydrous 1,2-dichlorobenzene) was spun at 800 rpm for 5 s followed by 2000 rpm for 40 s. The as-prepared films were vacuum dried for 2 h and then annealed at 120 ℃ for 15 min in Argon filled glub-box. Further 10 nm AlO_X was deposited on the polymer films following the steps as discussed in Section 4.2.2. Subsequently, the top polymer layers were stamped from ribbon-shaped FTM film which was fabricated with SP solution in anhydrous chloroform (3% w/w P3HT or PTB7, or 0.5% w/w PBTTT) on the liquid substrate (consisted of ethylene glycol at room temperature for P3HT and PTB7 and the mixture of ethylene glycol and glycerol in 1:1 ratio kept at temperature ~ 40 ^oC for PBTTT). These semi-completed samples were again vacuum-dried and annealing the same as above and finally 2 mm wide Al top-electrodes having thickness ~ 70 nm was deposited, under high vacuum, to complete the device. For clarity, positive bias was considered when the positive voltage was applied to the top electrode.

5.2.4 Device and Thin-film Characterization:

DC electrical characterization of the devices was performed utilizing a Keithley 2612 source-meter. AC response of the OSDs was measured by placing them in series with a 2 kΩ resistor and a variable frequency voltage signal (produced by Multi-Function Generator, WF1974). The ripple voltage was measured across the resistor by connecting an oscilloscope (Agilent MSO-X2004A) across it. For the electrical characterization, the devices were kept under mild vacuum (~10^{-2} Torr).

5.3 Results and Discussions

5.3.1 Efficient Utilization of Existing Technique towards Large Scale Application

5.3.1.1 Controlled Morphology of Ribbon Shaped FTM Films for in-plane Charge Transport

Reproducibility and uniformity of the thin film characteristics are highly desirable towards large scale fabrication. Therefore, in order to demonstrate uniformity in the thickness of the P3HT

ribbon-shaped thin films cast by FTM (**Figure 5.1**(a)), a large section of the film was stamped on a glass slide (26 mm * 75 mm) and was characterized through 2D positional mapping, the details of the measurement setup and its operation is described in Chapter 3[85]. The absorption spectra corresponding to each point areas with diameter 0.5 mm were mapped by moving the sample with a speed of 1 mm/s in the plane orthogonal to the aligned white light source and detector as shown in **Figure 3.1**. Here the detector implies to the photonic multi-channel analyzer (PMA-11, C7473-36, Hamamatsu Photonics, Japan), which consists of the rigidly fixed diffraction grating and 1024 photosensitive back-thinned charge-coupled devices with electronic shutter function which was controlled through an external pulsed signal. Through this system whole absorption spectrum was simultaneously measured for any point and a mask was placed between the sample and the detector to control the scanned area. In this work the mapping system parameters like, mask diameter 0.5 mm, stage speed of 1 mm/s, and shutter operating frequency of 2 Hz with 4% duty cycle were utilized for swift characterization of the large area samples. From the perusal of **Figure 5.1**, it is clear that the peak absorbance for the array of point areas from point A to point B are approximately equal, which also corroborates the uniformity in the thin-film's thickness following Beer-Lamberts law [86]. Further, in order to verify the macromolecular orientation and its variation at a large scale, the sample stamped on 26 mm × 75 mm glass substrate was cut in seven equal pieces (26 mm × 10 mm) samples and their polarized absorption were measured through a UV-Vis spectrophotometer (JASCO V-570) equipped with Glan-Thompson prism. The polarized spectra obtained for the middle section of the sample is shown in **Figure 5.1**. Since the transition dipole moment as a result of optically induced π-π^* transition is aligned along the SP backbone, therefore, linearly polarized light is absorbed maximum when the light polarization direction is kept along the polymer backbone direction. Hence, variation in peak absorbance value, when the light polarization direction is changed, corresponds to oriented polymer backbone in the thin film. From the perusal

of **Figure 5.1**, it is clear that the peak absorbance was higher when the light polarization direction was kept along the width of the P3HT ribbon (FTM). The optical anisotropy of the samples was calculated as the dichroic ratio (DR) = $A_{\parallel}/A_{\perp}$, where $A_{\parallel}$ represents the peak absorbance absorption spectra (wavelength corresponding to $A_{\parallel}$ is $\lambda_{max\text{-}\parallel}$) with the polarized light along the ribbon-width and $A_{\perp}$ is the absorbance value (at $\lambda_{max\text{-}\parallel}$) of the spectra with polarized light orthogonal to the ribbon-width. The DR values for all the seven samples were lying between 1.84 and 2.08. For the whole 26 mm × 70mm sample, the average DR = 1.95 ± 0.1 with a low standard deviation confirms the uniformity in the macromolecular arrangement throughout the P3HT ribbon-FTM film. The maximum absorbance along ribbon width confirmed the SP backbone orientation to be orthogonal to the film expansion direction. The obtained orientation direction is in good agreement with the proposed mechanism of orientation in FTM[11]. When a drop of the polymer solution is placed at the junction of the slider and viscous liquid substrate, unidirectional expansion of the SP solution is assisted by walls at both edge and slant surface of the slider. During film expansion, the action of opposing viscous force imparted by the liquid substrate and quick solvent evaporation lead to solid oriented film floating on the liquid substrate.

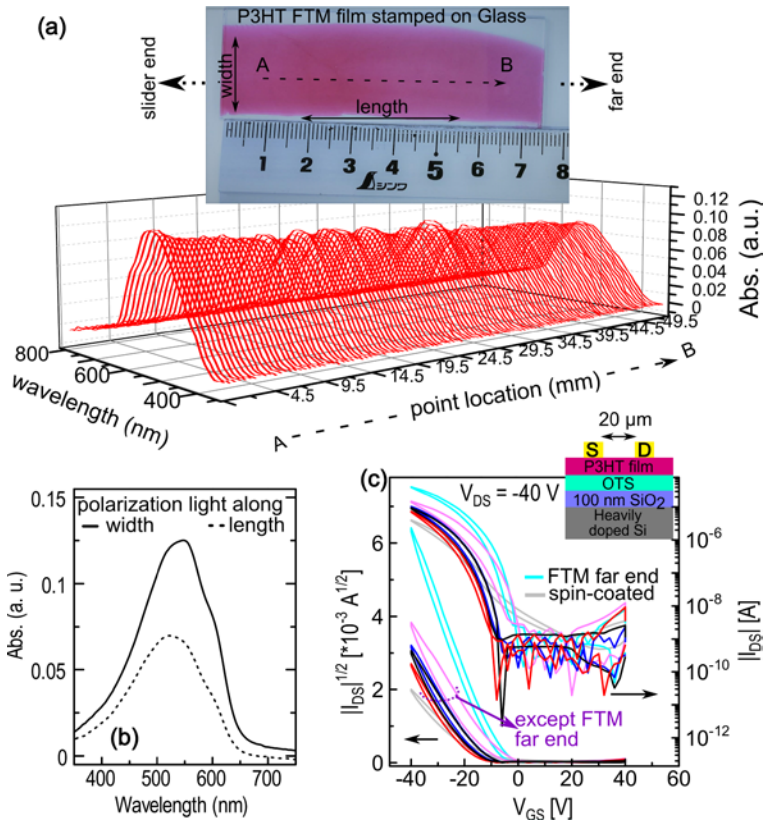

Figure 5.1 (a) Digital image of the P3HT ribbon (FTM) stamped on a glass substrate and the absorption spectra of array of point areas (with diameter of 0.5 mm) across line AB along ribbon length, measured through 2-dimensional positional mapping technique, and (b) representative polarized absorption spectra of the film measured through conventional UV-Vis spectrophotometer. (c) Representative transfer characteristics of the OFETs fabricated with FTM or spin-coated P3HT thin films. The OFETs architecture is shown in the inset (c) and the channel direction was kept along the ribbon width.

Further, in order to demonstrate uniformity in transport property of the ribbon shaped P3HT thin film, OFETs were fabricated with different portions of the thin film and their μ were compared, results are shown in **Figure 5.1** and summarized in Table 5.1. Since polarized absorption spectroscopy confirmed the SP backbone orientation along the ribbon width, therefore, the channels of the OFETs were fabricated along the width direction in order to obtain optimum transport property. In spite of low DR value obtained in FTM cast P3HT film, significant improvement in the field effect mobility was noticed compared to the spin-coated films, Table 5.1.

Table 5.1. The average field effect mobility ($\mu_{average}$) for the OFETs (with channel length and width of 20 μm and 2 mm respectively) fabricated with P3HT-thin films cast through various techniques.

Casting technique	$\mu_{average}$ ($cm^2V^{-1}s^{-1}$)
Spin-coat	0.0047
FTM	0.012
Friction Transfer	0.0015

5.3.1.2 Optimum Performance in Friction Transferred Based OFETs by Balanced Contact and Channel Resistance

Further, in order to demonstrate uniformity in transport property of the friction transferred thin-film, OFETs were also fabricated with different portions of the large area (7 cm × 1 cm) FT P3HT thin-films fabricated on the same substrates as shown in **Figure 5.2**. For friction transferred thin films the orientation of SP backbones is reported to be along the drawing direction and in this work also it was verified through polarized UV-Vis spectroscopy[11,70], therefore, the channels of OFETs were kept along the drawing direction. Since on OTS treated SiO_2, it was difficult to draw P3HT thin-film, therefore, bare SiO_2 substrates were utilized for OFET fabrication, the representative transport characteristics and the device structure are shown in **Figure 5.2**. The OFETs, with channel length and width of 20 μm and 2 mm respectively, fabricated using different regions of the thin film exhibited almost uniform $\mu \sim 0.0015$ $cm^2V^{-1}s^{-1}$. It is worth noting here that friction transfer thin films possessed comparatively rougher surface and of higher thickness compared to the FTM thin-films, as visually observed during the experiment. Although still exhaustive study is required to completely understand and quantify the role of contact resistance and access resistance originated due to the non-uniform metal/SP interface and thicker active layer, the channel length were varied in order to overcome these effects [145–147]. It was observed that for higher channel length ($\gtrsim$100 μm), the μ improved and it became comparable to that obtained in

the case of FTM film. Hence it indicated that by optimizing the OFET architecture, friction transferred SP thin-films can be utilized for large-sale applications.

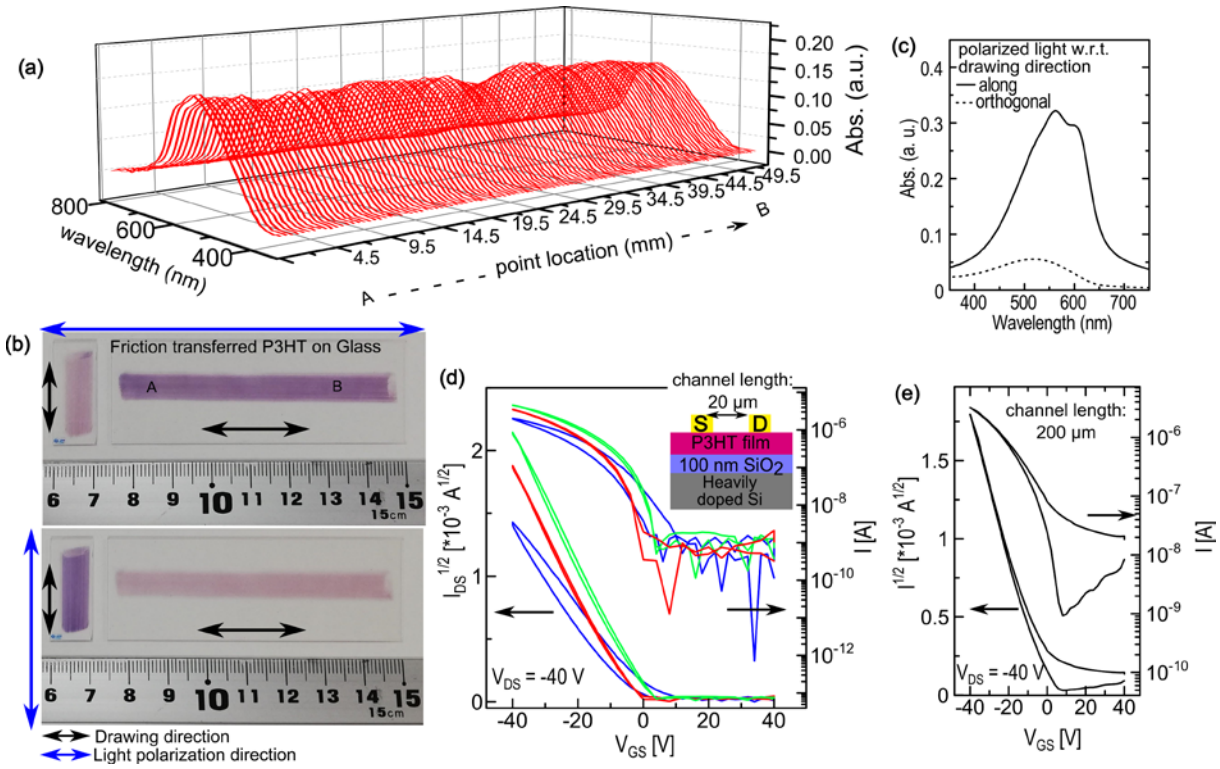

Figure 5.2 The absorption spectra of continuous point areas (with diameter = 0.5 mm) across line AB on friction transferred P3HT thin-film (a) and its digital image captured in presence of polarizing film (b). Representative polarized absorption spectra of the film measured through conventional UV-Vis spectrophotometer. Representative transfer characteristics of the thin film at different locations with channel length 20 μm (d) and 200 μm (e). The OFETs architecture is shown in the inset (d) and the channel direction was kept along the drawing direction.

5.3.1.3 Effect of Edge-on and Face-on Backbone-Conformation on Vertical Charge Transport

Carrier transport in the polymer thin films primarily occurs through π-electron cloud delocalized across the conjugated backbone which is also responsible for improved in-plane charge transport by orienting them along the channel direction, as discussed above. In order to reflect the exclusive role of polymer backbone in vertical charge transport, their end-on orientation, are desirable. Though there are few reports to impart partial end-on orientation into the thin film to orient the SP backbone perpendicular to the substrate, they are not compatible with common SPs

and also for large area uniform thin film fabrication[25,148]. In the remaining conformations edge-on, with pi-stacking parallel to substrate plane, is most commonly attained by solution coating due to lower surface energy of alkyl chains and/or their hydrophobic interaction with the substrate. However, polymer chains possessing face-on conformation, with alkyl stacking parallel to the substrate plane would result in improved vertical transport. Face-on conformantion has primarily been demonstrated by employing mechanical force like friction transfer of SP pellet on the substrate or by mechanically rubbing the SP thin film [11]. However their application for vertical charge transport has not been explored much. Therefore, in this section implications of friction transferred P3HT films on vertical transport characteristics has been descried. Besides, to demonstrate environmentally sustainable, inexpensive, and scalable fabrication of vertical device structure, FTM was also utilized along with friction transfer technique. Through these techniques, thin film of P3HT were cast for fabricating OSDs and their transport characteristics were analyzed. As explained in Chapter 4, SP thin film morphology plays crucial role in deciding the overall charge transport, therefore, the comparative analysis of FTM and friction transfer based OSDs would be an adequate tool for judicious selection of a device fabrication technique.

For the OSDs fabricated with only friction transferred P3HT films, considerable amount of leakage current and high device to device variation was observed which can be attributed to rough surface of the polymer film, besides, complete elimination of pinholes is not at all an easy task [62]. that which can be attributed to presence of tiny pin holes in the film and/or higher roughness. Though the pinholes or rough topography may not hamper the in-plane transport much, they can be highly detrimental to the vertical transport due to formation of short paths between the two electrodes as a consequence of metal diffusion during top contact deposition. Since single layer FTM P3HT films are too thin (~10 - 12 nm) to create considerable hindrance to the vertical carrier transport, therefore, to passivate the pinholes in the friction trancferred P3HT based OSDs, one

layer of FTM P3HT film was stamped above it as shown in **Figure 5.3**. Further, for the comparative analysis, the OSDs were also fabricated by sandwiching 5 layers of FTM P3HT films between two orthogonal electrodes (**Figure 5.3**). From the perusal of the representative *J*-*V* characteristic of the FTM based OSD, as shown in **Figure 5.3** (a), it is clear that devices possess clear rectifying property. As a signature of Schottky junction fabricated at P3HT/Al interface, OSDs allowed facile flow of current in positive bias (+ve bias applied to ITO electrode) and highly blocked in the reverse bias. The physical parameters for the OSDs were calculate using the thermionic equation model (Eq. (1.11)) and are listed in Table 5.2. The frequency response of the diodes was also measured and the measurement circuit and results are shown in **Figure 5.3** (b, c). The trend of ripple voltage across the load resistance (R_{Load}) at a different frequency of the input-voltage signal was compared and it was observed that the rectification due to OSDs was distinguishable up to 10 kHz. Further, friction transferred P3HT along with one FTM layer based OSD was analyzed, as shown in **Figure 5.3** (d). These device structures exhibited a higher forward current and rectification ratio as well as improved frequency response compared to that fabricated with only FTM based films, as listed in Table 5.2.

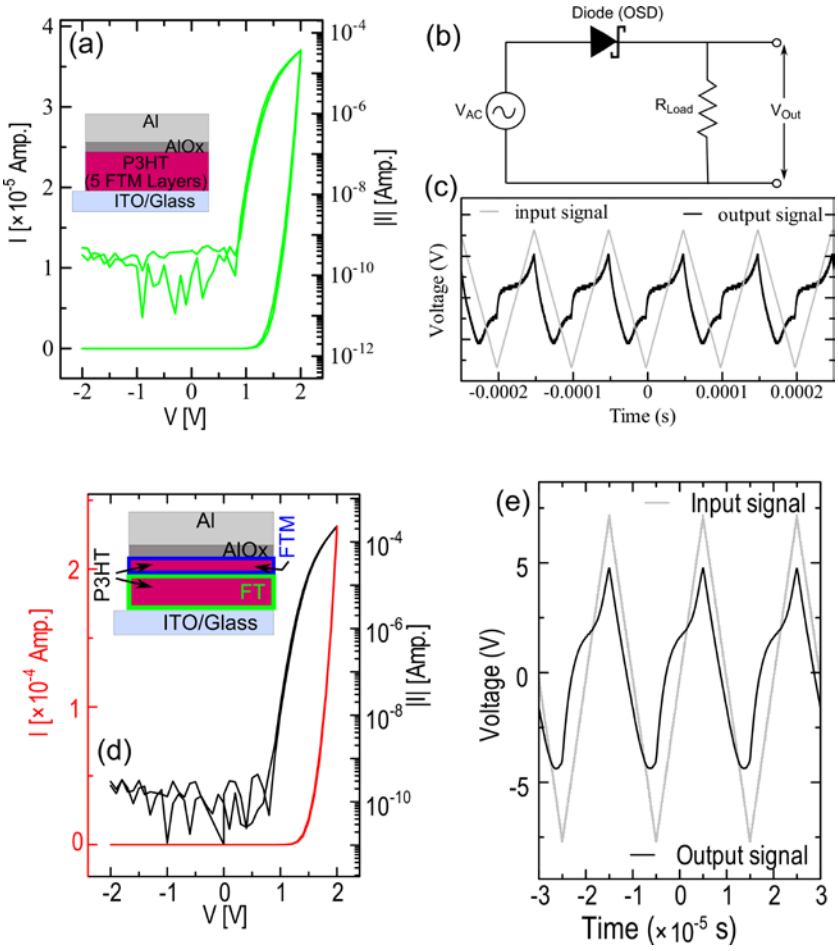

Figure 5.3 (a) J-V characteristics of the OSDs fabricated with 5 layers of P3HT film fabricated by FTM, device architecture is shown in the inset. (b) Circuit utilized to measure speed of the OSD R_{Load} was taken of 2 kOhms, and (c) AC response of the OSD at frequency 10 kHz. J-V characteristics of the OSDs fabricated with one layer of layers of friction transferred P3HT and one layer of P3HT film fabricated by FTM, device architecture is shown in the inset. (b) AC response of the OSD at frequency 50 kHz.

Table 5.2 Set of device parameters (η and *RR*) obtained by fitting the experimental *J –V* characteristics of different devices using thermionic emission model, Eq. (1.11).

Device Structure	Ideality factor (η)	Rectification Ratio (RR)	Switching Speed
5 layers of P3HT (FTM)	~ 1.9	~ 10^5	~ 10 kHz
1 layers of P3HT (friction transfer) + 1 layers of P3HT (FTM)	~ 1.8	~ 10^6	~50 kHz

From the perusal of Table 5.2, it is clear that the OSDs fabricated with a combination of friction transferred and FTM layers of P3HT possessed better transport characteristics compared

to that fabricated with only FTM coated P3HT layers. Higher rectification ration in the former case can be attributed to a reduced hindrance to carrier transport through the semiconducting polymer layer. The morphology of friction transferred and FTM coated P3HT thin films has been well reported by our group[62,149]. Due to complete face-on conformation of P3HT macromolecules in friction transferred films intermolecular electronic coupling (as a consequence of π-π stacking in the vertical direction) is much larger than that in edge-on oriented FTM coated multilayered P3HT film in which insulating alkyl-chains' stacking occur in the vertical direction. In the FTM based OSDs, the layers of P3HT thin film was coated in the open laboratory condition, therefore, the presence of trap states between cannot be avoided. Besides, at abrupt termination between the FTM coated P3HT layers larger lamellar distance (due to the absence of interdigitation between the separate FTM layers) is anticipated which may also be accounted for the corresponding hampered transport properties. Finally, it can be concluded that for highly reliable and repeatable efficient vertical charge transport can be fabricated by passivating the pinholes of friction transferred SP with a thin FTM coated polymer layer stamped at top.

5.3.1.4 Layer-by-Layer Printing of Conjugated Polymers for Bistable Resistive Memories

The advantages like less expensive and easy fabrication processes, mechanical flexibility, and freedom of tuning conjugated polyers' physical properties through appropriate structural engineering have drawn huge scientific interest towards the development of next-generation printed electronics [71–73,150]. Along with various circuit elements[151], the increasing interest in simple two-terminal memory elements as an alternative to solid-state memories triggered significant research activity in the recent past[152–154]. They are fabricated as an array of cross-point elements (as storage medium) sandwiched between two orthogonal electrodes. Huge efforts have been directed towards the development of the storage medium in which chemical or physical changes occur due to applied bias leading to the memory effect. Organic bistable resistive switches are one

of such elements initially reported by Ma and coworkers [155–157].

The common device structure utilized for organic non-volatile and rewritable memories are metal/organic semiconductor/metal junctions, field-effect transistors with charge trapping, and electromechanical switches, etc.[158–161]. Memory effect in the metal/organic/metal sandwiched architecture has been explored extensively using thin films of different SP, organic molecular semiconductors, and their blends with metal nanoparticles, etc. Moreover, layer-by-layer (LbL) structure of organic semiconductors with/without metal-nanostructures, sandwiched between two metal electrodes were also demonstrated, which exhibited better switching characteristics and operational stability compared to their blends[159,162]. The improved device characteristics in LbL structures manifest the better charge transport/hold through/at the well-defined interface between different layers. On the other hand, although the thin films of blend of two or more constituents are commercially viable, intrinsic problems pertaining to phase segregation is unavoidable.

Resistive switches fabricated by LbL coating of organic semiconductors have been mainly demonstrated using vacuum evaporation, spray coating, coating via crosslinking polymers and implementation of orthogonal solvents[159,162,163]. However, high fabrication costs, difficulty in fabrication and non-uniformity for large area implementation in thin films are the main challenging with vacuum evaporation of organic molecular semiconductors. On the other hand, in solution-based approaches for thin-film fabrication, intriguing issues like the need for compatible orthogonal solvents, chemical damage at the interface of consecutive solution coated films are yet to be addressed. Although crosslinking polymers can be coated in LbL architecture[162], there are limited choices for such materials and additional steps of crosslinking may increase the fabrication complexity and cost.

In order to provide an amicable solution for issues on multilayer coating via solution-based approaches Floating-film transfer method (FTM) was developed and extensively explored for

various SPs by our group[11,31,60,94]. FTM not only provides homogeneous oriented thin films but also is highly suitable for the LbL multilayer coating without having any detrimental effect on the underlying layers[34,164]. In order to make this technique more cost-effective, recently it was improvised, in which a drop (≈15 µl) of SP solution resulted in large-area thin films (>20 cm^2), as show in **Figure 2.3**, and the film morphology can be also tuned by changing the casting parameters[144,165]. In this work, LbL structure of SP with an interlayer of Al-islands was sandwiched between two metal electrodes to realize the bistable resistive switches. Different SPs were utilized to show the versatility of this technique.

Regioregular P3HT, PBTTT, super-dehydrated chloroform (Ch.), and 1,2-dichlorobenzene (DCB) were purchased from Sigma Aldrich and Poly[4,8-bis[(2-ethylhexyl)oxy] benzo [1,2-b:4,5-b']dithiophene-2,6-diyl][3-fluoro-2-[(2-ethylhexyl)carbonyl]thieno[3,4-b]thiophenediyl] (PTB7) from 1-Material. The thin-films were fabricated by two different techniques: (i) Spin-coating: SP solution (1% w/w RR-P3HT or PTB7 in Ch., or 1.5% w/w PBTTT in DCB) was spun at 800 rpm for 5 s followed by 2000 rpm for 40 s, (ii) FTM: a drop of SP dissolved in Ch. (3% w/w RR-P3HT or PTB7, or 0.5% w/w PBTTT-C14) was placed on the liquid substrate consisted of ethylene glycol at room temperature for RR-P3HT and PTB7 and mixture of ethylene glycol and glycerol (1:1) at temperature ~ 40 ^oC for PBTTT-C14. The devices were fabricated with LbL structure as schematically shown in **Figure 5.4**. At first, on a clean glass substrate patterned with 2 mm wide Al electrodes, the polymer solution was spun followed by vacuum drying for 2 h and annealing at 120 ^oC for 15 min in Ar atmosphere. Then ~10 nm Al (thickness was obtained through calibrated crystal oscillator) was deposited on it through thermal-evaporation under high vacuum (~10^{-6} Torr). This 10 nm Al layer sandwiched between the SP thin-films was indeed not continuous and its morphological characteristics have been extensively reported by us in our recent report[68]. In this work also the interfacial Al layer was deposited in similar experimental conditions, therefore, it

was considered as a layer of ~100 nm wide Al-islands. For the low thickness of thermally evaporated metal on the organic layer, the formation of islands due to terminated deposition before they fuse and make a continuous layer has been reported by other groups also [156,162]. Further, the top polymer layers were coated through FTM followed by vacuum drying and annealing. Finally, under high vacuum 2 mm wide orthogonal Al electrodes having thickness ~ 70 nm were deposited on top to complete the memory device. The electrical characterization of the devices was done using a Keithley 2612 source-meter in vacuum (~10^{-3} Torr). For clarity, only DC characterization is discussed here considering positive bias when the positive voltage was applied to the top electrode.

The current-voltage (*I*-*V*) response for different SP based devices are shown in **Figure 5.4**, with pinched hysteresis loop as the signature of resistive switching memories[166]. Since all the three SPs utilized in this work have similar energy band structure, therefore, analytical discussion with anyone might be helpful to understand the charge transport characteristics of others. RR-P3HT based devices without interfacial Al-islands did not show any resistive switching (Figure 5.4) and corresponding current density was also negligible (~10^{-8} A/cm^2). For such device structure, the poor charge injection can be attributed to the work-function mismatch between the SP and the electrode. In the other device structure, the Al-island was deposited by thermal evaporation (~0.1-0.4 Å/s) and due to residual oxygen in the evaporation chamber, the Al-islands can be represented as multilayered Al clusters with thin oxide layers between the layers. Therefore, the energy diagram of the Al-island was considered a series of energy wells next to each other. With these considerations, the switching mechanism can be explained in terms of the amount of charge stored or trapped at the Al-islands. The effect of stored charge can be explained by the model proposed by Ma et al. [156]. After biasing, the free electron in core-Al tunnel through the oxide barrier opposite to the field direction, making the Al-island layer polarized. The charge is stored at either side of

the middle Al layer. Subsequently, the stored charge leads to conductance change in adjacent SPP layers by inducing a charge similar to the conducting channel formation in the field-effect transistors, which can be considered as the low resistance state (LRS). The LRS state is retained even after the removal of bias because the polarized charge cannot recombine due to a huge barrier imparted by interfacial oxide layers. However, by reverting the bias the stored charges would recombine and lead to reinstallation of the device in its high resistance state (HRS). The concept and effect of trap state are well-explored [68,162], therefore, only a short discussion is provided here. At the oxide interfaces, large trap states lead to charge trapping resulting in space charge build-up, which also contributes to switching, by hindering further charge injection. Through this transport mechanism, the *I-V* response of all the device structures can be elucidated. To see the effect of bulk resistance, top P3HT film (FTM layers) were varied. Higher current observed for devices with 3-layers compared to that of 5-layers can be attributed to the decrease in the bulk resistance as shown in **Figure 5.4**. Since for the devices fabricated with P3HT, the current was low and also affected by noise, therefore, to explore the effect of the active layer further other SPs of the thiophene family, PTB7 with higher time of flight (TOF) hole mobility[167] and PBTTT-C14 with higher crystallinity but low TOF hole mobility[168] were utilized, the results are shown in Figure 5.4. Consequently, in comparison to RR-P3HT based devices, the current obtained for different devices fabricated with PTB7 and PBTTT was around one order of magnitude higher, and signal to noise ratio was also improved. Multiple cyclic scans of a typical PTB7 based device represent repeatable device performance as shown in. From the precise observation of **Figure 5.4**, it is clear that resistance switching characteristics of PTB7 based devices possessed optimum on/off and signal to noise ratios, compared to the other two, which was attributed to optimum TOF mobility, therefore, it can be a better choice for further study and application. Although for the ease of fabrication the devices were fabricated by casting the bottom layer by spin-coating, the devices can be fabricated by

depositing all the SP layers by only FTM. The future research is also focused in this direction and will be reported separately. Further, in order to show the advantage of the present device architecture, a comparative analysis merits and limitations of different techniques are summarized in Table 5.3.

Table 5.3. The merits and limitations of different device structures utilized for fabricating memory cells in sandwich structure.

Device structure (sandwiched between electrodes)	3D integration possible	Compatible for common SPs	Process	Cost at large scale	Ref.
Organic Small molecules' bilayer with metal nano-structure	Yes	No	Vacuum deposition	high	[156,163]
Bilayer Organic Polymers[a]	No	Yes	Spray-coating	Low	[159]
Blend of Organic polymers	No	No	Spin-coat	Low	[160], [169]
Crosslinking polymers' bilayer with metal nano-structures	Yes	No	Spin-coat	High	[162]
SP bilayers with metal nano-structure	Yes	Yes	FTM	Low	This work

[a] the organic polymers refer to either insulating polymers or semiconducting polymers, depending on the context of the cited works.

The bistable resistive switches were demonstrated with solution-processed LbL polymer films having Al-islands in the middle. The LbL fabrication of the SPs was performed utilizing a highly cost-effective solution based technique. To the best of our knowledge, this is the first report demonstrating bistable resistive switches fabricated via LbL using solution processable SPs. The presence of oxide covered Al islands play a crucial role in imparting the switching phenomena. Further, FTM can be exploited for scaling down the size of printed electronics by fabricating high-density three-dimensional structures, through horizontal and vertical integration on the same

substrate.

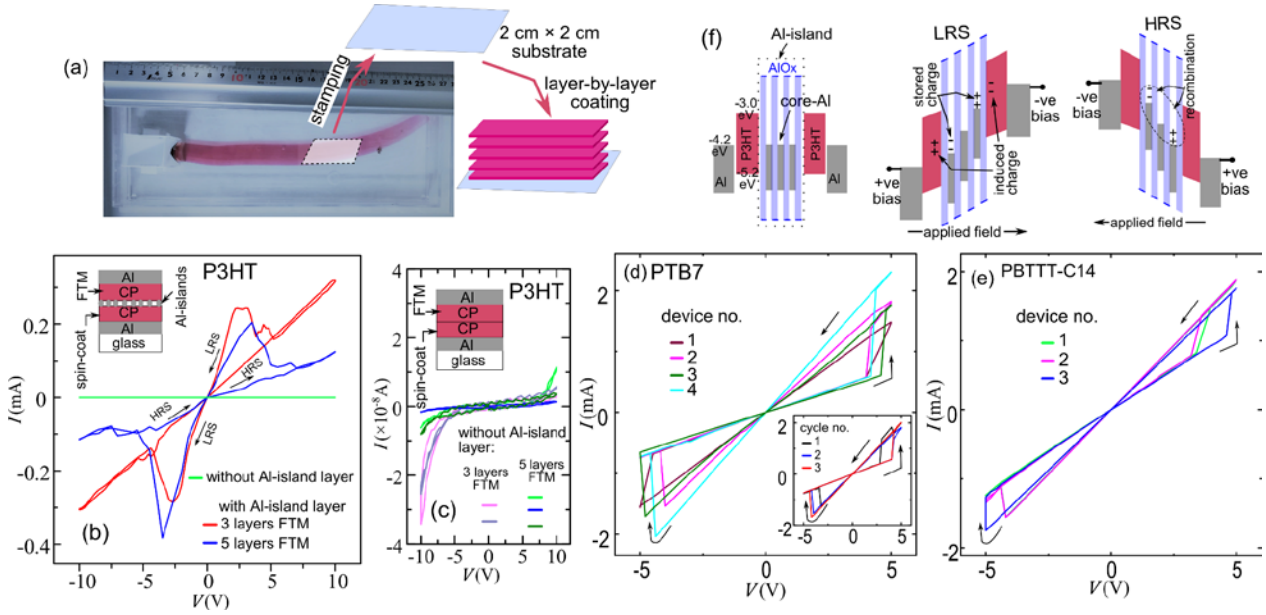

Figure 5.4 (a) Digital image of ribbon-shaped FTM thin-film of P3HT and illustrative schematic for layer-by-layer film casting on a substrate, (b) representative *I-V* plot for P3HT based devices device for which schematic is shown in the inset, (b) *I-V* plot for P3HT layers sandwiched between two Al-electrodes, without interfacial Al-nanostructures, (c) *I-V* plot for P3HT layers sandwiched between two Al-electrodes, without interfacial Al-nanostructures. Representative *I-V* plot for separate (d) PTB7 and (b) PBTTT-C14 based devices, devices schematic is shown in inset (a). Multiple cyclic scans for one PTB7 based device is shown in the inset (d). (f) Typical energy diagram of the device and effect of applied bias.

5.3.2 Development of Solvent Assisted Friction Transfer Technique

Due to the innate quasi-one-dimensional nature of conjugated polymers, in-plane charge transport i.e. field effect mobility (μ) of the OFETs, can be significantly increased by orienting the conjugated backbone in thin films. Huge scientific efforts have been dedicated in this direction and considerable improvement has been reported by various research groups[11,170,171]. Besides, the crucial role of macromolecular conformation and semiconductor/dielectric interface has also been investigated exhaustively [38,63]. To demonstrate the state-of-art μ of OFETs generally Si/SiO_2 substrates are utilized. Further hydrophobic treatment of the SiO_2 dielectric surface by depositing self-assembled monolayer proved to be an effective approach to attain orders of increment in μ [172].

Although improvement μ through the unidirectional orientation of backbone has been demonstrated through various approaches, many challenges such as device-to-device variation, serious health, and environmental hazard, etc. still need to be addressed. A brief analysis of the state of art orientation-techniques would be helpful to understand the strengths and shortcomings of the existing techniques. In the recent past, by orientating conjugated polymers, significant improvement in μ has been demonstrated through and for orientation, some of the techniques utilized and their demerits are as follows: solution shearing technique was introduced for large area crystalline thin film fabrication of organic molecular semiconductors [173,174]; however noticeable improvement in μ in conjugated polymer thin films could be not achieved until aggregation in solution was utilized [143,175,176]. Besides, using doctor blade technique orientation in P3HT fibrils (in solution) and effective increment in μ was also obtained along fiber axis demonstrated [177]. Along with them, for many other solution based techniques also the inevitability of aggregation in solution for orientation in conjugated polymer thin films and consequential increment in μ was confirmed [133,178–181]. Generally, conjugated polymer backbone gets disentangled during slow solvent evaporation and crystalline microstructures are formed due to their self-assembly, this property was exploited for orientation and increment in μ by Heeger group; however, this is an extremely slow process and effective [30,78,182]. Mohammadi et al. have introduced dynamic-template-directed orientation techniques through which swift orientation of conjugated polymer was attained but the μ was hampered due to mechanical damage in the film occurred during transfer from dynamic template to the substrate [33]. Apart from above-discussed issues, the need for a large amount of solvents may lead to serious health hazards if one gets exposed for a longer time [56]. Our group has also developed and extensively explored an orientation technique called floating-film transfer technique to orient various conjugated polymers with significant improvement in μ [31,60,183]. In this technique one drop of polymer solution is placed on the hydrophilic viscous liquid substrate

In this method, the viscosity of the hydrophilic liquid substrate which applies compressive force to the spreading solution, and through the simultaneous action of opposing forces polymer backbone gets oriented [31,91,165]. Through recent advancement, by incorporating a custom made slider, large area ribbon-shaped oriented thin films were demonstrated by the controlled expansion of the thin film. Although through this technique one drop of solvent led to the fabrication of long polymer thin films (area >20 cm^2), the attainment of uniform orientation throughout the thin film remains [85,144]. Further using friction transfer technique highly oriented polymer thin films have been reported[62,63]. No need for solvent for film fabrication qualifies it for sustainable green technology. Large area thin films with considerable uniform orientation and thickness also led to nearly similar device performance throughout the film as discussed in Section 5.3.1.2. It is also reported that in the as-cast friction transferred thin films the effective μ is lower due to face-on conformation of the oriented macromolecules, and after very high temperature annealing it significantly increased due to transition from face-on to edge-on but it may not be compatible with low-temperature device fabrication. Further, the role of the interface in OFET performance is well explored and it has been reported that SAM treatment of widely utilized SiO_2 dielectric led to orders of enhancement in, yet the less adherence of friction transferred thin films on hydrophobic substrates is another issue [36,184,185]. Conclusively in order to harness the full potential of existing technologies, some new technologies can be developed by combining advantages of all or some of them.

In order to address the above-discussed challenges, an ingenious technique was developed by incorporating the advantages of many existing processes. Through this technique, highly oriented PBTTT-C14 thin film fabrication was demonstrated on OTS treated substrate with complete edge-on macromolecular conformation in the thin film and to fabricate the thin film the setup of the conventional friction technique was utilized. To fabricate the oriented thin films, one small drop (< 10 µL) of solvent was placed at the pellet-substrate interface and the stage was moved

rapidly. The thin films were subjected to various optical and electrical characterizations and evidences regarding improved stacking and extended chain were obtained. By varying the annealing conditions and device architecture, the μ of 0.5 $cm^2V\text{-}1s^{-1}$ along the drawing direction.

5.3.2.1 Optical Characterization of the Thin Films

By second derivative fitting of non-polarized UV-Vis absorption spectra of the as-cast thin films exhibited a peak at ~546 nm and a feeble shoulder at 594 nm wavelengths and after annealing above the LC temperature the peak shifted to 554 nm and shoulder became prominent at 600nm, as shown in **Figure 5.6** (a). For conventionally friction transferred PBTTT-C14 thin films high orientation has been demonstrated earlier, Chapter 4. When The visible difference in the color as shown in **Figure 5.5** of the annealed thin film follows the significant red shift in the absorption spectra, **Figure 5.6** (a, b). The wavelengths corresponding to maximum absorbance and the shoulder were observed at 546 nm and ~ 600 nm for as-cast films and on annealing, it shifted to 556 nm and 604 nm. Since the wavelength corresponding to maximum absorbance corresponds to 0-1 transition and the more the red shift will be the more the chain straining occurs. The shoulder near 600 nm corresponds to π-π stacking. Therefore, shifts in the absorption spectra manifests the straitening in the chain and improved stacking. Further, the non-polarized spectra were also compared with the convention friction transferred PBTTT-C14 thin films. The conventional film itself shows high backbone straitening and it further increased due to the combined effect of shearing force and solvent. The optical characterizations of the thin films revealed J-aggregate type property in the thin film which was attributed to SP backbone straitening, which consequently may lead to an increase in the intra-chain electronic coupling.

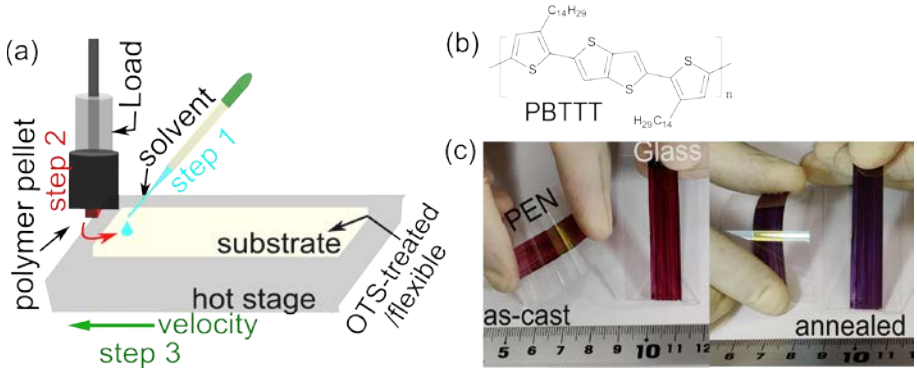

Figure 5.5 (a) Schematic representation for thin-film fabrication technique through solvent assisted Friction Transfer (FT) on OTS-treated or flexible substrates, (b) chemical structure of PBTTT, (c) representative digital images of the fabricated thin-films on different substrates.

Although a comprehensive theoretical understanding is still required to understand the spectroscopic characteristics of a highly planer conjugated polymer system, the obtained Raman/vibrational spectra can be explained by resolving the whole spectra in the peaks corresponding to fou types of bonds along the conjugated backbone, as summarized in Table 5.4. The polarized Raman spectra were deconvoluted in the constituent peaks using Gaussian function. From the perusal of polarized Raman spectra of the as-cast and annealed samples, **Figure 5.6** (c – f), it is clear that the peks′ intensity is higher along the drawing direction compared to that along the orthogonal direction, which can be attributed to the higher interaction between the incident polarized excitation and the Raman active bonds. Further the closer look into the resolved peaks it is clear that the peak at v_3 corresponding to the interring thiophene bonds are significant and almost comparable to the peak at v4 corresponding to thinothiophene bonds. The thinothiophene bond between the fused rings causes rigid rod nature to the PBTTT therefore intense peak (at v_4) has been reported previously for the solvent process and conventional friction transfer techniques. However, in those reports, very less intense c-c peak (at v_3) was observed. Therefore, the increased v_3 peak intensity can be attributed to more straitening of the SP backbone. As recently reported by Tanaka et al.[186], the inter-ring c-c bond has the freedom and the twisting and folding in the PBTTT

backbone is mainly originated by torsion in this bond. However, in this work, the combined role of mechanical force and the solvent causes higher straitening in the chain[187].

Table I. Raman peak assignment for PBTTT and relative peak intensities of parallel and orthogonal Raman spectra as shown in **Figure 5.6**.

Peak	Frequency (cm^{-1}) As-cast	Frequency (cm^{-1}) annealed	Assignment [a)]
ν_1	1342	-	thiophene C-C stretch
ν_2	1410	1410	thienothiophene C=C stretch
ν_3	1462	1458	inter-ring thiophene C-C stretch
ν_4	1492	1491	thiophene C=C stretch

[a)]Reference for peak assignments was taken from density functional theory (DFT) simulation reported by Gao et al.[188]

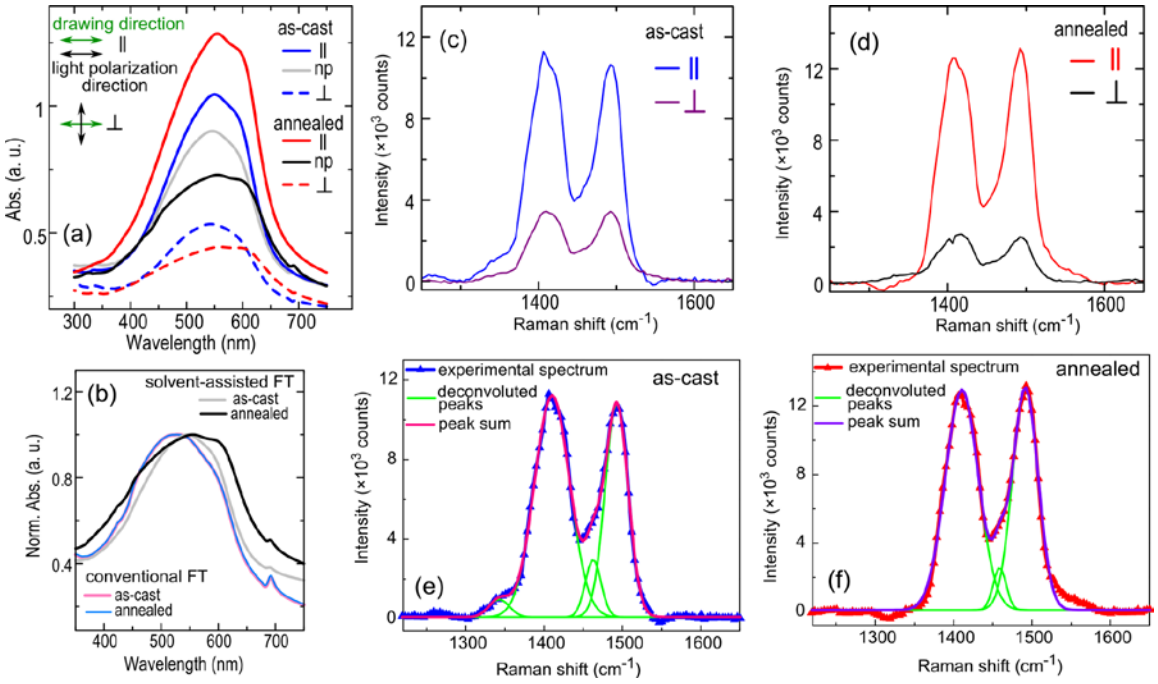

Figure 5.6 Non-polarized (np) and polarized absorption spectra (a), polarized Raman spectra of as-cast (c) and annealed (d) thin films of PBTTT fabricated on OTS treated substrates through solvent assisted Friction Transfer techniques. The exciting electric field was kept parallel (||) or perpendicular (⊥) to the drawing direction for the measurements. (b) Normalized non-polarized absorption spectra of friction transferred PBTTT-C14 through conventional or solvent assisted technique.. Deconvolution of || spectra of as-cast (d) and annealed (d) thin films using Voigt function. The films were annealed at 180 °C.

To analyze the macromolecular arrangement, in-plane GIXD and out-of-plane XRD measurements were performed as per the geometry shown in **Figure 5.7**. It can be seen that in case

of the samples as-prepared and annealed below LC temperature for friction transferred PBTTT-C14 thin-film on bare oxide substrate, series of diffraction peaks (*h00*) corresponding to alkyl-stacking is observed for in-plane GIXD and are absent in the out-of-plane GIXD. This clearly reflects that macromolecules in the as-prepared thin films adopted face-on orientation and upon annealing above the LC temperature[31], where side chain melts to reorganize the crystalline domains leading to the observed conformational change in the thin film. A closer look at XRD patterns reveals that peak intensity of (*h00*) decreases in the in-plane and increases in out-of-plane mode with the increase in the annealing temperature ≥ 150 °C, while just opposite trend was observed for the (*010*) diffraction peak corresponding to π- π stacking. These results clearly suggest that there is a gradual change in the conformation of PBTTT-C14 from face-on dominated to edge-on dominated depending on the annealing temperature. It is worth to note here that at 200 °C, the intensity of the (*h00*) diffraction peak is observable in both of the in-plane and out-of-plane modes, therefore, partly the PBTTT macromolecules can be considered to recrystallize in edge-on conformation. Moreover, since (*010*) diffraction peak did also not diminish completely in the out-of-plane mode at 200 °C, it suggests that some face-on oriented crystallites also remained in the film.[135] Whereas for the same condition almost complete edge-on conformation was obtained on silane treated oxide substrate as verified by X-ray diffraction (XRD) measurements. Since such high annealing temperature may not be compatible with many flexible substrates, therefore, drawing-technique was improvised.

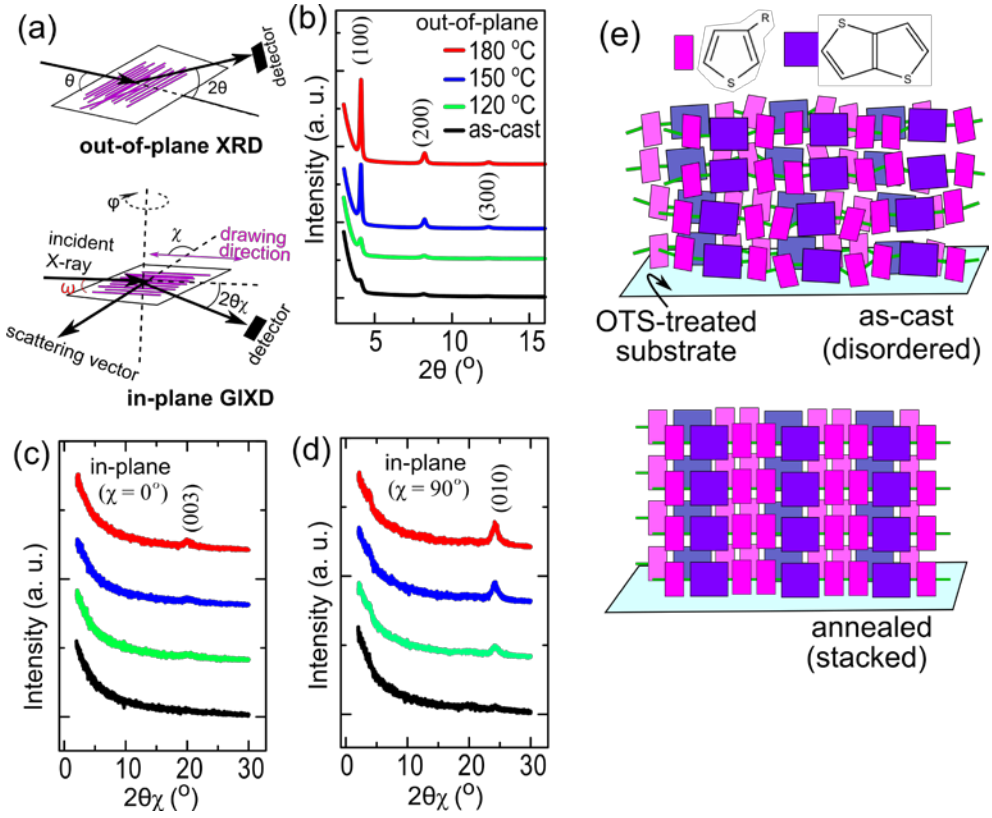

Figure 5.7. (a) Schematic diagram for the measurement technique of out-of-plane XRD and in-plane GIXD. (b) Out-of-plane XRD pattern and (b) in-plane GIXD patterns of the solvent-assisted friction transferred PBTTT thin-films, with scattering vector (c) along ($\chi = 0°$) and (d) orthogonal ($\chi = 90°$) to the drawing direction, and (e) schematic representation for the proposed macromolecular arrangement in the thin film.

To examine the impact of these highly oriented thin films of PBTTT on the charge transport, OFETs were fabricated on OTS treated SiO_2 substrates in the bottom gate top contact geometry as schematically shown in the inset of **Figure 5.8** (a). The saturation μ and other electronic parameters were extracted from the transfer curves ($I_{DS} - V_{GS}$) as described earlier[123]. The OFETs were fabricated with the thin films as-cast and annealed at 150 °C. The difference in channel length dependence of the transfer curve for the as-cast and annealed thin film was observed, which can be attributed to differences in channel resistance. Therefore, we anticipate that during annealing, the straitening and stacking of the backbone led to a decrease in overall channel resistance,[137,138]. Although few reports are there regarding the estimation of OFET's contact resistance, efforts are still required to develop a reliable model. Moreover, it is well accepted that by increasing the

channel length its resistance can be matched with contact resistance for better analysis of OFETs. In this work optimum for thin films as-cast and annealed temperature were attained by analyzing transfer characteristics of respective OFETs with varying channel lengths. The μ of 0.5cm^{2}V^{-1}/s^{-1} was obtained for thin films annealed at 140^{o}C.

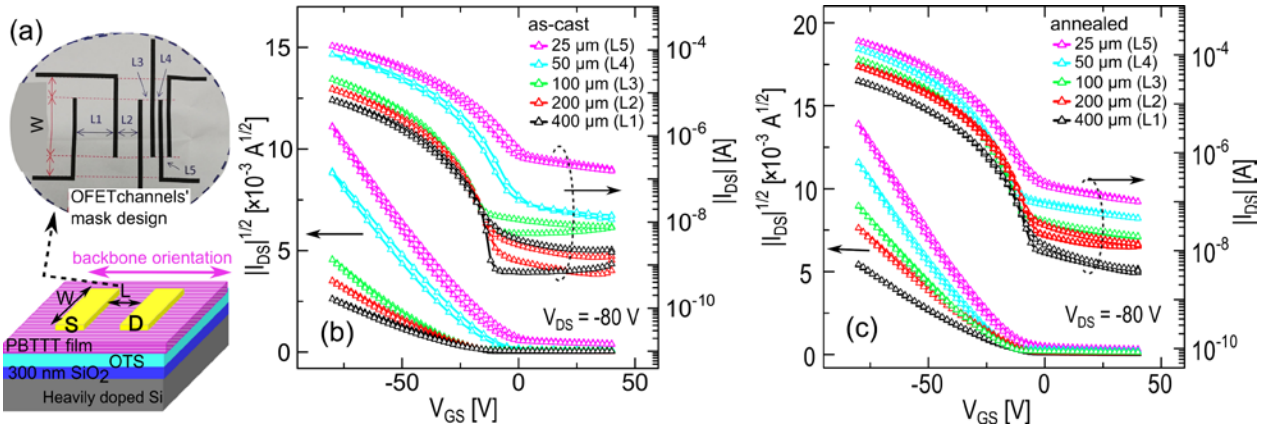

Figure 5.8 (a) Schematic illustration for OFET and the design of a Ni-mask with varying channel lengths (L) is shown in the inset. Transfer characteristics of the OFETs with different L, fabricated on (b) as-cast and (c) annealed (at 140 ℃) solvent-assisted friction transferred PBTTT thin-films.

5.4 Conclusion

The recent developments in the field of organic electronics are mainly focused towards enhancing the transport characteristics of thin-films by designing, synthesis, and increasing their crystallinity through various casting techniques. However, still some challenges need to be addressed before the commercialization of organic electronics, for instance, serious health and environment hazards due to the inevitable use of halogenated solvents, variation in large area thin-film, etc. In this work, two techniques, floating-film transfer method and friction transfer, have been utilized to demonstrate the environmentally sustainable fabrication of large area thin-films possessing adequate uniformity in physical transport characteristics. Organic field effect transistors were fabricated from using different regions of the large-area thin films (≳10 cm^2) and by optimizing casting conditions, uniformity in μ was demonstrated. Besides, one order enhancement in μ, compared to spin-coated thin films, was also achieved by tuning the device architecture. A

new technique was proposed for highly crystalline thin film fabrication with least hazards. In such a case, the as-cast thin-film exhibited complete edge-on conformation and after annealing at 140 °C, 4-order of (*h00*)-peaks and absorption maximum at 556 nm was observed, representing its highly compact and crystalline nature. Under optimum conditions, $\mu > 0.5$ $cm^2 V^{-1} s^{-1}$ was obtained which is comparable to the standard values reported for this material.

Chapter 6: Conclusion and Future Work

The charge transport characteristics of organic electronic devices (OEDs) primarily depend on the thin film morphology and interfacial qualities. In recent past semiconducting polymers (SPs) based OEDs have drawn widespread attention and significant improvement in their performance has been reported by tuning macromolecular conformation and orientation in the thin-films through inexpensive solution-processes, exploiting inherent quasi-1-dimensionality of SPs. However, the inevitability of hazardous halogenated solvents and occasionally pre-aggregation of SPs are the main challenges to attain the goal of roll-to-roll fabrication of OEDs. In order to address these issues, the comprehensive effort was dedicated, consequently, fabrication of large area polymer thin-films were demonstrated with just one drop of solvent (floating-film transfer method, FTM) or without using solvent (friction transfer technique). Further, 2D-positional mapping technique was developed for swift microstructural characterization of thin-films and fast optimization of experimental parameters resulting in charge transport uniformity at large-scale. Furthermore, the implications of interfaces, such as dielectric/SP or metal/SP, were also studied exhaustively and their diverse applications were demonstrated, for instance, to improve in-plane charge transport, to improve the rectification ratio of organic Schottky diodes. Moreover, utilizing FTM, the fabrication of organic memristors in layer-by-layer architecture was also demonstrated, which may lead to three-dimensional integration of printed electronics.

As discussed various techniques have been reported for improving the crystallinity of the thin films and many of them, like FTM, friction transfer, solution-shearing, etc., lead to the inexpensive fabrication of large-area polymer thin film. Corresponding thin film morphology, an implicit function of various casting parameters, can be optimized through a series of film fabrication by tuning the parameters and comparing their characteristics. Besides, position-

dependent morphological variation is another big issue with large area SP thin films. There are many sophisticated techniques, atomic force microscopy, X-ray diffraction, near edge x-ray absorption fine structure spectroscopy, variable angle spectroscopic ellipsometry, etc., through which precise microstructural characterization of SP thin films is performed but they are not suitable for swift characterization of large-area thin films (> several cm^2). 2D-positional mapping technique was developed for swift microstructural characterization of thin-films and fast optimization of experimental parameters resulting in charge transport uniformity at large-scale. With this mapping technique, position-dependent absorption spectra were measured at varying locations through the aligned light source and multichannel detector and by the controlled movement of the sample stage. The sample was scanned along multiple lines by comparing the intensity, broadening, and shifts of absorption spectra a map of microstructural distribution throughout the thin film was realized.

Further, as transport characteristics of OEDs primarily depend on the thin film morphology and the interfacial qualities, therefore, the effect of interface and the thin-film morphology on in-plane and out-of-plane charge transport were studied. To analyze the effects on vertical charge transport, Organic Schottky diodes were fabricated with varying metal/SP interfaces and the morphology of the SP film was also varied by opting different casting techniques. An extensive transport model was also developed for calculation and comparative analysis of their transport parameters. In-plane charge transport was studied by fabricating organic field transistors, in bottom-gated top contact device architecture on bare and self-assembled mono-layer treated substrates (Si/SiO_2). On annealing, conformational changes in the thin film were observed which also varied depending on the substrates' surface energy. Consecutive effect on in-plane charge transport was also recorded and to interpret a pertinent carrier-transport mechanism was proposed in light of the obtained results from temperature and interface dependent electrical and optical

characterization of the friction transferred PBTTT-C14 thin-films. Further efforts were also dedicated towards environmentally sustainable large scale fabrication of OEDs. In this regard, a new film fabrication technique was also developed which interestingly provided significant improvement in film crystallinity and in-plane charge transport.

References

1. Schweicher, G. *et al.* Molecular Semiconductors for Logic Operations: Dead-End or Bright Future? *Advanced Materials* **32**, (2020).
2. Sun, Y. & Rogers, J. A. Inorganic semiconductors for flexible electronics. *Advanced Materials* **19**, 1897–1916 (2007).
3. Sirringhaus, H., Tessler, N. & Friend, R. H. Integrated Optoelectronic Devices Based on Conjugated Polymers. *Science (80-.).* **280**, 1741–1744 (1998).
4. Wang, C., Dong, H., Hu, W., Liu, Y. & Zhu, D. Semiconducting π-conjugated systems in field-effect transistors: A material odyssey of organic electronics. *Chemical Reviews* **112**, 2208–2267 (2012).
5. Jacob, M. & V., M. Organic Semiconductors: Past, Present and Future. *Electronics* **3**, 594–597 (2014).
6. Mühl, S. & Beyer, B. Bio-Organic Electronics—Overview and Prospects for the Future. *Electronics* **3**, 444–461 (2014).
7. Printed, flexible electronics now breaking commercial barriers - Converting Quarterly | Greenville, SC. Available at: http://www.convertingquarterly.com/the-converting-curmudgeon/printed-flexible-electronics-now-breaking-commercial-barriers. (Accessed: 12th September 2020)
8. Organic Solar Cells - Fraunhofer ISE. Available at: https://www.ise.fraunhofer.de/en/business-areas/photovoltaics/emerging-photovoltaic-technologies/organic-solar-cells.html. (Accessed: 12th September 2020)
9. Asia-Pacific Flexible Electronics Market Size, Opportunity,. Available at: https://www.openpr.com/news/1935268/asia-pacific-flexible-electronics-market-size-opportunity. (Accessed: 12th September 2020)
10. Enabling Flexible Displays and Sensors With Organic Electronics. Available at: https://www.global-engage.com/technology/flexible-displays-sensors-organic-electronics/. (Accessed: 12th September 2020)
11. Pandey, M., Kumari, N., Nagamatsu, S. & Pandey, S. S. Recent advances in the orientation of conjugated polymers for organic field-effect transistors. *J. Mater. Chem. C* **7**, 13323–13351 (2019).
12. Rivnay, J., Mannsfeld, S. C. B., Miller, C. E., Salleo, A. & Toney, M. F. Quantitative Determination of Organic Semiconductor Microstructure from the Molecular to Device Scale. *Chem. Rev.* **112**, 5488–5519 (2012).
13. Lee, W. H., Cho, J. H. & Cho, K. Control of mesoscale and nanoscale ordering of organic semiconductors at the gate dielectric/semiconductor interface for organic transistors. *J. Mater. Chem.* **20**, 2549–2561 (2010).
14. Mcculloch, I. *et al.* Semiconducting thienothiophene copolymers: Design, synthesis, morphology, and performance in thin-film Organic transistors. *Adv. Mater.* **21**, 1091–1109 (2009).
15. Liming, D. *Intelligent Macromolecules for Smart Devices*. *Structure* (2004). doi:10.1007/b97517
16. Carlé, J. E. Website. *http://plasticphotovoltaics.org/lc/lc-materials/lc-conjugated.html* date visted 2017 May 10
17. Bredas, J. & Street, G. Polarons, bipolarons, and solitons in conducting polymers. *Acc. Chem. Res.*

1305, 309–315 (1985).

18. Chiang, C. K. *et al.* Polyacetylene, (CH)x: N-type and p-type doping and compensation. *Appl. Phys. Lett.* **33**, 18–20 (1978).

19. Chien, J. C. *Polyacetylene: Chemistry, physics, and material science*. *British Polymer Journal* **18**, (1984).

20. Heeger, A. J., Kivelson, S., Schrieffer, J. R. & Su, W. P. Solitons in conducting polymers. *Rev. Mod. Phys.* **60**, 781–850 (1988).

21. Garnier, F., Hajlaoui, R., Yassar, A. & Srivastava, P. All-polymer field-effect transistor realized by printing techniques. *Science* **265**, 1684–6 (1994).

22. Yang, H., Lefevre, S. W., Ryu, C. Y. & Bao, Z. Solubility-driven thin film structures of regioregular poly(3-hexyl thiophene) using volatile solvents. *Appl. Phys. Lett.* **90**, 172116 (2007).

23. Chang, J. F. *et al.* Enhanced Mobility of poly(3-hexylthiophene) transistors by spin-coating from high-boiling-point solvents. *Chem. Mater.* **16**, 4772–4776 (2004).

24. Jimison, L. H., Toney, M. F., McCulloch, I., Heeney, M. & Salleo, A. Charge-Transport Anisotropy Due to Grain Boundaries in Directionally Crystallized Thin Films of Regioregular Poly(3-hexylthiophene). *Adv. Mater.* **21**, 1568–1572 (2009).

25. Ma, J., Hashimoto, K., Koganezawa, T. & Tajima, K. End-on orientation of semiconducting polymers in thin films induced by surface segregation of fluoroalkyl chains. *J. Am. Chem. Soc.* **135**, 9644–9647 (2013).

26. Sirringhaus, H. *et al.* Two-dimensional charge transport in self-organized, high-mobility conjugated polymers. *Nature* **401**, 685–688 (1999).

27. Tumbleston, J. R. *et al.* The influence of molecular orientation on organic bulk heterojunction solar cells. *Nat. Photonics* **8**, 385–391 (2014).

28. Dodabalapur, A., Torsi, L. & Katz, H. E. Organic Transistors - 2-Dimensional Transport and Improved Electrical Characteristics. *Science (80-.).* **268**, 270–271 (1995).

29. Gu, X., Shaw, L., Gu, K., Toney, M. F. & Bao, Z. The meniscus-guided deposition of semiconducting polymers. *Nat. Commun.* **9**, 534 (2018).

30. Tseng, H.-R. *et al.* High Mobility Field Effect Transistors Based on Macroscopically Oriented Regioregular Copolymers. *Nano Lett.* **12**, 6353–6357 (2012).

31. Pandey, M. *et al.* Rapid Formation and Macroscopic Self-Assembly of Liquid-Crystalline, High-Mobility, Semiconducting Thienothiophene. *Adv. Mater. Interfaces* **5**, 1700875 (2018).

32. Hartmann, L. *et al.* 2D versus 3D crystalline order in thin films of regioregular poly(3-hexylthiophene) oriented by mechanical rubbing and epitaxy. *Adv. Funct. Mater.* **21**, 4047–4057 (2011).

33. Mohammadi, E. *et al.* Dynamic-template-directed multiscale assembly for large-area coating of highly-aligned conjugated polymer thin films. *Nat. Commun.* **8**, 16070 (2017).

34. Pandey, M. *et al.* Layer-by-layer coating of oriented conjugated polymer films towards anisotropic electronics. *Synth. Met.* **227**, 29–36 (2017).

35. Arca, F. *et al.* Interface trap states in organic photodiodes. *Sci. Rep.* **3**, 1–5 (2013).

36. Kline, R. J., McGehee, M. D. & Toney, M. F. Highly oriented crystals at the buried interface in polythiophene thin-film transistors. *Nat. Mater.* **5**, 222–228 (2006).

37. Chua, L. L. *et al.* General observation of n-type field-effect behaviour in organic semiconductors. *Nature* **434**, 194–199 (2005).

38. Kline, R. J. *et al.* Significant dependence of morphology and charge carrier mobility on substrate surface chemistry in high performance polythiophene semiconductor films. *Appl. Phys. Lett.* **90**, 062117 (2007).

39. Chabinyc, M. L. *et al.* Lamination method for the study of interfaces in polymeric thin film transistors. *J. Am. Chem. Soc.* **126**, 13928–13929 (2004).

40. Greiner, M. T., Chai, L., Helander, M. G., Tang, W. M. & Lu, Z. H. Transition metal oxide work functions: The influence of cation oxidation state and oxygen vacancies. *Adv. Funct. Mater.* **22**, 4557–4568 (2012).

41. Khim, D. *et al.* Electron injection enhancement by a Cs-salt interlayer in ambipolar organic field-effect transistors and complementary circuits. *J. Mater. Chem.* **22**, 16979–16985 (2012).

42. Greiner, M. T. *et al.* Universal energy-level alignment of molecules on metal oxides. *Nat. Mater.* **11**, 76–81 (2012).

43. Wang, S. D., Minari, T., Miyadera, T., Tsukagoshi, K. & Aoyagi, Y. Contact-metal dependent current injection in pentacene thin-film transistors. *Appl. Phys. Lett.* **91**, 203508 (2007).

44. Pesavento, P. V., Puntambekar, K. P., Frisbie, C. D., McKeen, J. C. & Ruden, P. P. Film and contact resistance in pentacene thin-film transistors: Dependence on film thickness, electrode geometry, and correlation with hole mobility. *J. Appl. Phys.* **99**, 094504 (2006).

45. Di, C. *et al.* High-Performance Organic Field-Effect Transistors with Low-Cost Copper Electrodes. *Adv. Mater.* **20**, 1286–1290 (2008).

46. Lilja, K. E. *et al.* Effect of dielectric barrier on rectification, injection and transport properties of printed organic diodes. *J. Phys. D. Appl. Phys.* **44**, 295301 (2011).

47. Pierret, R. F. Semiconductor Device Fundamentals. *New York* 792 (1996). doi:10.1007/BF00198606

48. Facchetti, A., Yoon, M.-H. & Marks, T. J. Gate Dielectrics for Organic Field-Effect Transistors: New Opportunities for Organic Electronics. *Adv. Mater.* **17**, 1705–1725 (2005).

49. Dimitrakopoulos, C. D. & Shaw, J. M. Low-Voltage Organic Transistors on Plastic Comprising High-Dielectric Constant Gate Insulators. *Science (80-.).* **283**, 822–824 (1999).

50. Noh, Y. Y. & Sirringhaus, H. Ultra-thin polymer gate dielectrics for top-gate polymer field-effect transistors. *Org. Electron. physics, Mater. Appl.* **10**, 174–180 (2009).

51. Liu, P., Wu, Y., Li, Y., Ong, B. S. & Zhu, S. Enabling gate dielectric design for all solution-processed, high-performance, flexible organic thin-film transistors. *J. Am. Chem. Soc.* **128**, 4554–4555 (2006).

52. Borkan, H. & Weimer, P. K. Analysis of characteristics of insulated-gate thin-film transistors. *RCA Rev.* **24**, 153–165 (1963).

53. Kang, C. M., Shin, H. & Lee, C. High-frequency organic rectifiers through interface engineering. *MRS*

Commun. **7**, 755–769 (2017).

54. Jurchescu, O. D. Large-Area Organic Electronics: Inkjet Printing and Spray Coating Techniques. in *Organic Electronics* 319–339 (Wiley-VCH Verlag GmbH & Co. KGaA, 2013). doi:10.1002/9783527650965.ch13

55. Xu, J. *et al.* Multi-scale ordering in highly stretchable polymer semiconducting films. *Nat. Mater.* **18**, 594–601 (2019).

56. Halogenated Solvent Cleaning: National Emission Standards for Hazardous Air Pollutants (NESHAP) | Stationary Sources of Air Pollution | US EPA. Available at: https://www.epa.gov/stationary-sources-air-pollution/halogenated-solvent-cleaning-national-emission-standards-hazardou-0. (Accessed: 7th May 2020)

57. Ong, B. S., Wu, Y., Liu, P. & Gardner, S. High-Performance Semiconducting Polythiophenes for Organic Thin-Film Transistors. *J. Am. Chem. Soc.* **126**, 3378–3379 (2004).

58. Andersson, M. R. *et al.* Regioselective polymerization of 3-(4-octylphenyl)thiophene with FeCl3. *Macromolecules* **27**, 6503–6506 (1994).

59. Trznadel, M., Pron, a, Zagorska, M., Chrzaszcz, R. & Pielichowski, J. Effect of Molecular Weight on Spectroscopic and Spectroelectrochemical Properties of Regioregular Poly(3-hexylthiophene). *Macromolecules* **31**, 5051–5058 (1998).

60. Morita, T. *et al.* Enhancement of transport characteristics in poly(3-hexylthiophene) films deposited with floating film transfer method. *Appl. Phys. Express* **2**, 12–15 (2009).

61. Dauendorffer, A., Nagamatsu, S., Takashima, W. & Kaneto, K. Optical and Transport Anisotropy in Poly(9,9$'$-dioctyl-fluorene- alt -bithiophene) Films Prepared by Floating Film Transfer Method. *Jpn. J. Appl. Phys.* **51**, 055802 (2012).

62. Nagamatsu, S. *et al.* Backbone arrangement in 'friction-transferred' regioregular poly(3-alkylthiophene)s. *Macromolecules* **36**, 5252–5257 (2003).

63. Hosokawa, Y. *et al.* Molecular orientation and anisotropic carrier mobility in poorly soluble polythiophene thin films. *Appl. Phys. Lett.* **100**, 203305 (2012).

64. Sze, S. M. & Ng, K. K. *Physics of semiconductor devices*. (John Wiley & Sons, 2007).

65. Kaneto, K. & Takashima, W. Fabrication and characteristics of Schottky diodes based on regioregular poly(3-hexylthiophene)/Al junction. *Curr. Appl. Phys.* **1**, 355–361 (2001).

66. Güllü, O., Aydoğan, S. & Türüt, A. High barrier Schottky diode with organic interlayer. *Solid State Commun.* **152**, 381–385 (2012).

67. Gunduz, B., Yahia, I. S. & Yakuphanoglu, F. Electrical and photoconductivity properties of p-Si/P3HT/Al and p-Si/P3HT:MEH-PPV/Al organic devices: Comparison study. in *Microelectronic Engineering* **98**, 41–57 (2012).

68. Kumari, N. *et al.* Role of device architecture and AlO X interlayer in organic Schottky diodes and their interpretation by analytical modeling. *J. Appl. Phys.* **126**, 125501 (2019).

69. Chabinyc, M. L. X-ray scattering from films of semiconducting polymers. *Polym. Rev.* **48**, 463–492 (2008).

70. Kumari, N., Pandey, M., Nagamatsu, S., Nakamura, M. & Pandey, S. S. Investigation and Control of

Charge Transport Anisotropy in Highly Oriented Friction-Transferred Polythiophene Thin Films. *ACS Appl. Mater. Interfaces* **12**, 11876–11883 (2020).

71. Someya, T. *et al.* Paper-like electronic displays: Large-area rubber-stamped plastic sheets of electronics and microencapsulated electrophoretic inks. *PNAS* **98**, 4835–4840 (2004).

72. Myny, K. *et al.* An 8-bit, 40-instructions-per-second organic microprocessor on plastic foil. *IEEE J. Solid-State Circuits* **47**, 284–291 (2012).

73. Chou, H.-H. *et al.* A chameleon-inspired stretchable electronic skin with interactive colour changing controlled by tactile sensing. *Nat. Commun.* **6**, 8011 (2015).

74. Ling, H., Liu, S., Zheng, Z. & Yan, F. Organic Flexible Electronics. *Small Methods* **2**, 1800070 (2018).

75. Lewis, J. Material challenge for flexible organic devices. *Mater. Today* **9**, 38–45 (2006).

76. Crossland, E. J. W. *et al.* Anisotropic charge transport in spherulitic Poly(3-hexylthiophene) films. *Adv. Mater.* **24**, 839–844 (2012).

77. Pandey, M., Nagamatsu, S., Takashima, W., Pandey, S. S. & Hayase, S. Interplay of Orientation and Blending: Synergistic Enhancement of Field Effect Mobility in Thiophene-Based Conjugated Polymers. *J. Phys. Chem. C* **121**, 11184–11193 (2017).

78. Tseng, H. R. *et al.* High-mobility field-effect transistors fabricated with macroscopic aligned semiconducting polymers. *Adv. Mater.* **26**, 2993–2998 (2014).

79. Park, Y. *et al.* Single-Crystal Poly[4-(4,4-dihexadecyl-4H-cyclopenta[1,2-b:5,4-b']dithiophen-2-yl)-*alt* -[1,2,5]thiadiazolo[3,4- *c*]pyridine] Nanowires with Ultrahigh Mobility. *Nano Lett.* **19**, 1028–1032 (2019).

80. Lee, J. *et al.* An Ultrahigh Mobility in Isomorphic Fluorobenzo[*c*][1,2,5]thiadiazole-Based Polymers. *Angew. Chemie Int. Ed.* **57**, 13629–13634 (2018).

81. Tripathi, A. S. M., Kumari, N., Nagamatsu, S., Hayase, S. & Pandey, S. S. Facile fabrication of large area oriented conjugated polymer films by ribbon-shaped FTM and its implication on anisotropic charge transport. *Org. Electron.* **65**, 1–7 (2019).

82. Nahid, M. M., Gann, E., Thomsen, L. & McNeill, C. R. NEXAFS spectroscopy of conjugated polymers. *European Polymer Journal* **81**, 532–554 (2016).

83. Zhang, X. *et al.* Molecular packing of high-mobility diketo pyrrolo-pyrrole polymer semiconductors with branched alkyl side chains. *J. Am. Chem. Soc.* **133**, 15073–15084 (2011).

84. Spano, F. C. Modeling disorder in polymer aggregates: The optical spectroscopy of regioregular poly(3-hexylthiophene) thin films. *J. Chem. Phys.* **122**, 234701 (2005).

85. Kumari, N. *et al.* 2D positional profiling of orientation and thickness uniformity in the semiconducting polymers thin films. *Org. Electron.* **68**, 221–229 (2019).

86. Beer–Lambert law (or Beer–Lambert–Bouguer law). in *IUPAC Compendium of Chemical Terminology* (IUPAC, 2008). doi:10.1351/goldbook.b00626

87. Clark, J., Silva, C., Friend, R. H. & Spano, F. C. Role of intermolecular coupling in the photophysics of disordered organic semiconductors: Aggregate emission in regioregular polythiophene. *Phys. Rev. Lett.* **98**, 206406 (2007).

88. Clark, J., Chang, J. F., Spano, F. C., Friend, R. H. & Silva, C. Determining exciton bandwidth and film microstructure in polythiophene films using linear absorption spectroscopy. *Appl. Phys. Lett.* **94**, 163306 (2009).

89. Kumar, A., Takashima, W., Kaneto, K. & Prakash, R. Nano-dimensional self assembly of regioregular poly (3-hexylthiophene) in toluene: Structural, optical, and morphological properties. *J. Appl. Polym. Sci.* **131**, 40931 (2014).

90. Chang, M., Lee, J., Kleinhenz, N., Fu, B. & Reichmanis, E. Photoinduced Anisotropic Supramolecular Assembly and Enhanced Charge Transport of Poly(3-hexylthiophene) Thin Films. *Adv. Funct. Mater.* **24**, 4457–4465 (2014).

91. Pandey, M., Pandey, S. S., Nagamatsu, S., Hayase, S. & Takashima, W. Influence of backbone structure on orientation of conjugated polymers in the dynamic casting of thin floating-films. *Thin Solid Films* **619**, 125–130 (2016).

92. Kumari, N., Pandey, M., Nagamatsu, S. & Pandey, S. S. 2D positional mapping of casting condition driven microstructural distribution in organic thin films. *Jpn. J. Appl. Phys.* **59**, SCCA06 (2020).

93. Wang, S. D., Miyadera, T., Minari, T., Aoyagi, Y. & Tsukagoshi, K. Correlation between grain size and device parameters in pentacene thin film transistors. *Appl. Phys. Lett.* **93**, 043311 (2008).

94. Pandey, M., Nagamatsu, S., Pandey, S. S., Hayase, S. & Takashima, W. Enhancement of carrier mobility along with anisotropic transport in non-regiocontrolled poly (3-hexylthiophene) films processed by floating film transfer method. *Org. Electron.* **38**, 115–120 (2016).

95. Lunt, R. R., Benziger, J. B. & Forrest, S. R. Relationship between Crystalline Order and Exciton Diffusion Length in Molecular Organic Semiconductors. *Adv. Mater.* **22**, 1233–1236 (2010).

96. Soylu, M., Yahia, I. S., Yakuphanoglu, F. & Farooq, W. A. Modification of electrical properties of Al/p-Si Schottky barrier device based on 2′-7′-dichlorofluorescein. *J. Appl. Phys.* **110**, 074514 (2011).

97. Hyun Kim, C., Yaghmazadeh, O., Bonnassieux, Y. & Horowitz, G. Modeling the low-voltage regime of organic diodes: Origin of the ideality factor. *J. Appl. Phys.* **110**, 093722 (2011).

98. Kuik, M. *et al.* 25th Anniversary Article: Charge Transport and Recombination in Polymer Light-Emitting Diodes. *Adv. Mater.* **26**, 512–531 (2014).

99. Haldi, A., Sharma, A., Potscavage, W. J. & Kippelen, B. Equivalent circuit model for organic single-layer diodes. *J. Appl. Phys.* **104**, 064503 (2008).

100. Koster, L. J. A., Smits, E. C. P., Mihailetchi, V. D. & Blom, P. W. M. Device model for the operation of polymer/fullerene bulk heterojunction solar cells. *Phys. Rev. B* **72**, 085205 (2005).

101. De Bruyn, P., Van Rest, A. H. P., Wetzelaer, G. A. H., De Leeuw, D. M. & Blom, P. W. M. Diffusion-limited current in organic metal-insulator-metal diodes. *Phys. Rev. Lett.* **111**, 186801 (2013).

102. Diemer, P. J. *et al.* Quantitative analysis of the density of trap states at the semiconductor-dielectric interface in organic field-effect transistors. *Appl. Phys. Lett.* **107**, (2015).

103. Veres, J., Ogier, S. D., Leeming, S. W., Cupertino, D. C. & Khaffaf, S. M. Low-k insulators as the choice of dielectrics in organic field-effect transistors. *Adv. Funct. Mater.* **13**, 199–204 (2003).

104. Richards, T., Bird, M. & Sirringhaus, H. A quantitative analytical model for static dipolar disorder broadening of the density of states at organic heterointerfaces. *J. Chem. Phys.* **128**, 234905 (2008).

105. McCulloch, I. *et al.* Liquid-crystalline semiconducting polymers with high charge-carrier mobility. *Nat. Mater.* **5**, 328–333 (2006).

106. Blom, P. W. M., Tanase, C., de Leeuw, D. M. & Coehoorn, R. Thickness scaling of the space-charge-limited current in poly(p-phenylene vinylene). *Appl. Phys. Lett.* **86**, 092105 (2005).

107. Nicolai, H. T. *et al.* Space-charge-limited hole current in poly(9,9-dioctylfluorene) diodes. *Appl. Phys. Lett.* **96**, 172107 (2010).

108. Streetman, B. G. & Banerjee, S. *Solid State Electronic Devices*. (Oxford:Pearson).

109. Aziz, H. *et al.* Degradation processes at the cathode/organic interface in organic light emitting devices with Mg:Ag cathodes. *Appl. Phys. Lett.* **72**, 2642 (1998).

110. Semov, Y. I. Work Function of Oxidized Metal Surfaces and Estimation of Al2O3 Film Band Structure Parameters. *Phys. status solidi* **32**, K41-44 (1969).

111. Agarwala, V. K. & Fort, T. Work function changes during low pressure oxidation of aluminum at room temperature. *Surf. Sci.* **45**, 470–482 (1974).

112. Shi, Y. *et al.* Work function engineering of electrodes via electropolymerization of ethylenedioxythiophenes and its derivatives. *Org. Electron.* **9**, 859–863 (2008).

113. Oh, S.-W. *et al.* The photovoltaic effect of the p–n heterojunction organic photovoltaic device using a nano template method. *Curr. Appl. Phys.* **5**, 55–58 (2005).

114. Moliton, A. & Nunzi, J.-M. How to model the behaviour of organic photovoltaic cells. *Polym. Int.* **55**, 583–600 (2006).

115. Brabec, C. J., Sariciftci, N. S. & Hummelen, J. C. Plastic Solar Cells. *Adv. Funct. Mater.* **11**, 15–26 (2001).

116. Kraft, T. M., Berger, P. R. & Lupo, D. Printed and organic diodes: devices, circuits and applications. *Flex. Print. Electron.* **2**, 033001 (2017).

117. Kim, C. H. *et al.* Capacitive behavior of pentacene-based diodes: Quasistatic dielectric constant and dielectric strength. *J. Appl. Phys.* **109**, 083710 (2011).

118. Gustafsson, G., Inganäs, O., Sundberg, M. & Svensson, C. Rectifying metal/poly(3-hexylthiophene) contacts. *Synth. Met.* **41**, 499–502 (1991).

119. Jiang, T. *et al.* Thiophene Derivatives on Gold and Molecular Dissociation Processes. *J. Phys. Chem. C* **121**, 27923–27935 (2017).

120. Singh, V., Thakur, A. K., Pandey, S. S., Takashima, W. & Kaneto, K. A comparative study of Al and LiF:Al interfaces with poly (3-hexylthiophene) using bias dependent photoluminescence technique. *Org. Electron.* **9**, 790–796 (2008).

121. Gupta, S. *et al.* Ozone oxidation methods for aluminum oxide formation: Application to low-voltage organic transistors. *Org. Electron.* **21**, 132–137 (2015).

122. Wan, A., Hwang, J., Amy, F. & Kahn, A. Impact of electrode contamination on the α-NPD/Au hole injection barrier. *Org. Electron.* **6**, 47–54 (2005).

123. Pandey, M., Pandey, S. S., Nagamatsu, S., Hayase, S. & Takashima, W. Solvent driven performance in thin floating-films of PBTTT for organic field effect transistor: Role of macroscopic orientation.

Org. Electron. **43**, 240–246 (2017).

124. Deegan, R. D. *et al.* Contact line deposits in an evaporating drop. *Phys. Rev. E* **62**, 756–765 (2000).

125. Perelaer, J. *et al.* The Spreading of Inkjet-Printed Droplets with Varying Polymer Molar Mass on a Dry Solid Substrate. *Macromol. Chem. Phys.* **210**, 495–502 (2009).

126. Wang, S. D., Minari, T., Miyadera, T., Tsukagoshi, K. & Tang, J. X. Contact resistance instability in pentacene thin film transistors induced by ambient gases. *Appl. Phys. Lett.* **94**, 083309 (2009).

127. Mukherjee, A. K. & Kumari, N. Current voltage perspective of an organic electronic device. *Phys. Lett. A* **382**, 1413–1418 (2018).

128. Armbruster, O., Lungenschmied, C. & Bauer, S. Dielectric response of doped organic semiconductor devices: P3HT:PCBM solar cells. *Phys. Rev. B* **84**, 085208 (2011).

129. Choulis, S. A. *et al.* High ambipolar and balanced carrier mobility in regioregular poly(3-hexylthiophene). *Appl. Phys. Lett.* **85**, 3890–3892 (2004).

130. Chabinyc, M. L., Toney, M. F., Kline, R. J., McCulloch, I. & Heeney, M. X-ray scattering study of thin films of poly(2,5-bis(3-alkylthiophen-2-yl)thieno[3,2-b]thiophene). *J. Am. Chem. Soc.* **129**, 3226–3237 (2007).

131. Hamidi-Sakr, A., Biniek, L., Fall, S. & Brinkmann, M. Precise Control of Lamellar Thickness in Highly Oriented Regioregular Poly(3-Hexylthiophene) Thin Films Prepared by High-Temperature Rubbing: Correlations with Optical Properties and Charge Transport. *Adv. Funct. Mater.* **26**, 408–420 (2016).

132. DeLongchamp, D. M. *et al.* High Carrier Mobility Polythiophene Thin Films: Structure Determination by Experiment and Theory. *Adv. Mater.* **19**, 833–837 (2007).

133. Bucella, S. G. *et al.* Macroscopic and high-throughput printing of aligned nanostructured polymer semiconductors for MHz large-area electronics. *Nat. Commun.* **6**, 8394 (2015).

134. Biniek, L. *et al.* High-temperature rubbing: A versatile method to align π-conjugated polymers without alignment substrate. *Macromolecules* **47**, 3871–3879 (2014).

135. Soeda, J. *et al.* Highly Oriented Polymer Semiconductor Films Compressed at the Surface of Ionic Liquids for High-Performance Polymeric Organic Field-Effect Transistors. *Adv. Mater.* **26**, 6430–6435 (2014).

136. Yabuuchi, Y. *et al.* Coating speed dependence of main chain orientation and aggregation of PBTTT-C16 in the bar-coated thin film. *Jpn. J. Appl. Phys.* **59**, SDDA04 (2020).

137. Schuettfort, T. *et al.* Microstructure of polycrystalline PBTTT films: Domain mapping and structure formation. *ACS Nano* **6**, 1849–1864 (2012).

138. Lee, M. J. *et al.* Anisotropy of Charge Transport in a Uniaxially Aligned and Chain-Extended, High-Mobility, Conjugated Polymer Semiconductor. *Adv. Funct. Mater.* **21**, 932–940 (2011).

139. Salleo, A., Chabinyc, M. L., Yang, M. S. & Street, R. A. Polymer thin-film transistors with chemically modified dielectric interfaces. *Appl. Phys. Lett.* **81**, 4383–4385 (2002).

140. Orgiu, E. *et al.* The dramatic effect of the annealing temperature and dielectric functionalization on the electron mobility of indene-C60 bis-adduct thin films. *Chem. Commun.* **51**, 5414–5417 (2015).

141. Umeda, T., Kumaki, D. & Tokito, S. Surface-energy-dependent field-effect mobilities up to 1

cm2/V s for polymer thin-film transistor. *J. Appl. Phys.* **105**, 024516 (2009).

142. Mas-Torrent, M. & Rovira, C. Crystal Structure Performance Relationship in OFETs. in *Functional Supramolecular Architectures* 649–682 (WILEY-VCH Verlag & Co. KGaA, 2014). doi:10.1002/9783527689897.ch21

143. Giri, G. *et al.* Effect of Solution Shearing Method on Packing and Disorder of Organic Semiconductor Polymers. *Chem. Mater.* **27**, 2350–2359 (2015).

144. Tripathi, A. S. M. *et al.* Anisotropic charge transport in highly oriented films of semiconducting polymer prepared by ribbon-shaped floating film. *Appl. Phys. Lett.* **112**, 123301 (2018).

145. Wang, Q. *et al.* Role of Schottky Barrier and Access Resistance in Organic Field-Effect Transistors. *J. Phys. Chem. Lett.* **11**, 1466–1472 (2020).

146. Krammer, M. *et al.* Critical evaluation of organic thin-film transistor models. *Crystals* **9**, 85 (2019).

147. Bhargava, K. & Singh, V. Electrical characterization and parameter extraction of organic thin film transistors using two dimensional numerical simulations. *J. Comput. Electron.* **13**, 585–592 (2014).

148. Aryal, M., Trivedi, K. & Hu, W. (Walter). Nano-Confinement Induced Chain Alignment in Ordered P3HT Nanostructures Defined by Nanoimprint Lithography. *ACS Nano* **3**, 3085–3090 (2009).

149. Tripathi, A. S. M., Gupta, R. K., Sharma, S., Nagamatsu, S. & Pandey, S. S. Molecular orientation and anisotropic charge transport in the large area thin films of regioregular Poly(3-alkylthiophenes) fabricated by ribbon-shaped FTM. *Org. Electron.* **81**, 105687 (2020).

150. Adachi, C. Third-generation organic electroluminescence materials. *Japanese Journal of Applied Physics* **53**, 060101 (2014).

151. Forrest, S. R. The path to ubiquitous and low-cost organic electronic appliances on plastic. *Nature* **428**, 911–918 (2004).

152. Gudesen Nordal Leistad, H. G. P.-E. G. I. Electrically addressable passive device, method for electrical addressing of the same and uses of the device and the method. 4–25 (2000).

153. Scott, J. C. Is There an Immortal Memory? *Science* **304**, 62–63 (2004).

154. Kim, S. G., Han, J. S., Kim, H., Kim, S. Y. & Jang, H. W. Recent Advances in Memristive Materials for Artificial Synapses. *Advanced Materials Technologies* **3**, (2018).

155. Ma, L. P., Liu, J. & Yang, Y. Organic electrical bistable devices and rewritable memory cells. *Appl. Phys. Lett.* **80**, 2997–2999 (2002).

156. Ma, L., Pyo, S., Ouyang, J., Xu, Q. & Yang, Y. Nonvolatile electrical bistability of organic/metal-nanocluster/organic system. *Appl. Phys. Lett.* **82**, 1419–1421 (2003).

157. Ouyang, J., Chu, C. W., Szmanda, C. R., Ma, L. & Yang, Y. Programmable polymer thin film and non-volatile memory device. *Nat. Mater.* **3**, 918–922 (2004).

158. Naber, R. C. G., Asadi, K., Blom, P. W. M., De Leeuw, D. M. & De Boer, B. Organic nonvolatile memory devices based on ferroelectricity. *Advanced Materials* **22**, 933–945 (2010).

159. Rehman, M. M., Yang, B. S., Yang, Y. J., Karimov, K. S. & Choi, K. H. Effect of device structure on the resistive switching characteristics of organic polymers fabricated through all printed technology. *Curr. Appl. Phys.* **17**, 533–540 (2017).

160. Nguyen, V. C. & Lee, P. S. Coexistence of write once read many memory and memristor in blend of poly(3,4-ethylenedioxythiophene): Polystyrene sulfonate and polyvinyl alcohol. *Sci. Rep.* **6**, (2016).

161. Tsao, H. Y. & Lin, Y. J. Resistive switching behaviors of Au/pentacene/Si-nanowire arrays/heavily doped n-type Si devices for memory applications. *Appl. Phys. Lett.* **104**, (2014).

162. Bozano, L. D. *et al.* Organic materials and thin-film structures for cross-point memory cells based on trapping in metallic nanoparticles. *Adv. Funct. Mater.* **15**, 1933–1939 (2005).

163. Casula, G. *et al.* Air-stable, non-volatile resistive memory based on hybrid organic/inorganic nanocomposites. *Org. Electron.* **18**, 17–23 (2015).

164. Yang, D. S., Chung, K. & Kim, J. Controlled alignment of polymer chains near the semiconductor-dielectric interface. *Org. Electron.* **76**, 105484 (2020).

165. Pandey, M., Pandey, S. S., Nagamatsu, S., Hayase, S. & Takashima, W. Controlling Factors for Orientation of Conjugated Polymer Films in Dynamic Floating-Film Transfer Method. *J. Nanosci. Nanotechnol.* **17**, 1915–1922 (2017).

166. Chua, L. O. Memristor—The Missing Circuit Element. *IEEE Trans. Circuit Theory* **18**, 507–519 (1971).

167. Ebenhoch, B., Thomson, S. A. J., Genevičius, K., Juška, G. & Samuel, I. D. W. Charge carrier mobility of the organic photovoltaic materials PTB7 and PC71BM and its influence on device performance. *Org. Electron.* **22**, 62–68 (2015).

168. Baklar, M. *et al.* Bulk charge transport in liquid-crystalline polymer semiconductors based on poly(2,5-bis(3-alkylthiophen-2-yl)thieno[3,2-b]thiophene). *Polym. Chem.* **1**, 1448–1452 (2010).

169. Asadi, K., Li, M., Stingelin, N., Blom, P. W. M. & De Leeuw, D. M. Crossbar memory array of organic bistable rectifying diodes for nonvolatile data storage. *Appl. Phys. Lett.* **97**, 193308 (2010).

170. Brinkmann, M., Hartmann, L., Biniek, L., Tremel, K. & Kayunkid, N. Orienting Semi-Conducting π-Conjugated Polymers. *Macromol. Rapid Commun.* **35**, 9–26 (2014).

171. Khim, D. *et al.* Uniaxial Alignment of Conjugated Polymer Films for High-Performance Organic Field-Effect Transistors. *Adv. Mater.* **1705463**, 1705463 (2018).

172. Umeda, T., Kumaki, D. & Tokito, S. Surface-energy-dependent field-effect mobilities up to 1 cm2/V s for polymer thin-film transistor. *J. Appl. Phys.* **105**, 024516 (2009).

173. Diao, Y. *et al.* Solution coating of large-area organic semiconductor thin films with aligned single-crystalline domains. *Nat. Mater.* **12**, 665–671 (2013).

174. Becerril, H. A., Roberts, M. E., Liu, Z., Locklin, J. & Bao, Z. High-performance organic thin-film transistors through solution-sheared deposition of small-molecule organic semiconductors. *Adv. Mater.* **20**, 2588–2594 (2008).

175. Lee, J. *et al.* Solution-Processable Ambipolar Diketopyrrolopyrrole–Selenophene Polymer with Unprecedentedly High Hole and Electron Mobilities. *J. Am. Chem. Soc.* **134**, 20713–20721 (2012).

176. Lee, J. *et al.* Boosting the Ambipolar Performance of Solution-Processable Polymer Semiconductors via Hybrid Side-Chain Engineering. *J. Am. Chem. Soc.* **135**, 9540–9547 (2013).

177. Chu, P. H. *et al.* Toward Precision Control of Nanofiber Orientation in Conjugated Polymer Thin Films: Impact on Charge Transport. *Chem. Mater.* **28**, 9099–9109 (2016).

178. Jiang, Y. *et al.* Fast Deposition of Aligning Edge-On Polymers for High-Mobility Ambipolar Transistors. *Adv. Mater.* **31**, 1805761 (2019).

179. Kim, N. K. *et al.* High-Performance Organic Field-Effect Transistors with Directionally Aligned Conjugated Polymer Film Deposited from Pre-Aggregated Solution. *Chem. Mater.* **27**, 8345–8353 (2015).

180. Shin, E.-S. & Noh, Y.-Y. Effect of pre-aggregation in solution state on the performance of organic field-effect transistors with indacenodithiophene-co-benzothiadiazole. *Org. Electron.* **53**, 111–116 (2018).

181. Kim, N. K., Shin, E. S., Noh, Y. Y. & Kim, D. Y. A selection rule of solvent for highly aligned diketopyrrolopyrrole-based conjugated polymer film for high performance organic field-effect transistors. *Org. Electron.* **55**, 6–14 (2018).

182. Luo, C. *et al.* General strategy for self-assembly of highly oriented nanocrystalline semiconducting polymers with high mobility. *Nano Lett.* **14**, 2764–2771 (2014).

183. Pandey, M., Nagamatsu, S., Pandey, S. S., Hayase, S. & Takashima, W. Orientation Characteristics of Non-regiocontrolled Poly (3-hexyl-thiophene) Film by FTM on Various Liquid Substrates. *J. Phys. Conf. Ser.* **704**, 012005 (2016).

184. Wu, Y. *et al.* Controlled orientation of liquid-crystalline polythiophene semiconductors for high-performance organic thin-film transistors. *Appl. Phys. Lett.* **86**, 1–3 (2005).

185. Veres, J., Ogier, S., Lloyd, G. & De Leeuw, D. Gate insulators in organic field-effect transistors. *Chemistry of Materials* **16**, 4543–4555 (2004).

186. Tanaka, H. *et al.* Thermoelectric properties of a semicrystalline polymer doped beyond the insulator-to-metal transition by electrolyte gating. *Sci. Adv.* **6**, 8065–8079 (2020).

187. Zhao, L. H. *et al.* Role of borderline solvents to induce pronounced extended-chain lamellar order in π-stackable polymers. *Macromolecules* **44**, 9692–9702 (2011).

188. Gao, J. Spectroscopic Studies of Conjugated Polymer Nanostructures and Polymer/Acceptor Blends. *Chem. ETDs* (2014).

Achievements

Publications

1. **N. Kumari**, M. Pandey, S. Nagamatsu, M. Nakamura, S. S. Pandey "Investigation and control of charge transport anisotropy in highly oriented friction transferred polythiophene thin films" ACS Appl. Mater. Interfaces 12 (2020) 11876- 11883. (IMPACT FACTOR 8.45)
2. **N. Kumari**, M. Pandey, K. Hamada, D. Hirotani, S. Nagamatsu, S. Hayase, S. S. Pandey "Role of Device Architecture and AlO_X Interlayer in Organic Schottky Diodes and Their Interpretation by Analytical Modeling" *Journal of Applied Physics* 126 (2019), 125501. (IMPACT FACTOR 2.32)
3. **N. Kumari**, M. Pandey, S. Nagamatsu, S. S. Pandey "2D Positional Mapping of Casting Condition Driven Microstructural Distribution in Organic Thin Films" *Japanese Journal of Applied Physics* 59(SC) (2019), SCCA06. (IMPACT FACTOR 1.47)
4. **N. Kumari**, A. Tripathi, S. Sadakata, M. Pandey, S. Nagamatsu, S. Hayase, S. S. Pandey "2D positional profiling of orientation and thickness uniformity in the semiconducting polymers thin films" *Organic Electronics* 68 (2019), 221–229. (IMPACT FACTOR 3.49)
5. M. Pandey, **N. Kumari**, S. Nagamatsu, S. S. Pandey " Recent Advances in Orientation of Conjugated Polymers for Organic Field-Effect Transistors" *Journal of Material Chemistry C* 7 (2019) 13323-13351. (IMPACT FACTOR 6.64)
6. A. Tripathi, **N. Kumari**, S. Sadakata, M. Pandey, S. Nagamatsu, S. Hayase, S. S. Pandey "Facile fabrication of large area oriented conjugated polymer films by ribbon-shaped FTM and its implication on anisotropic charge transport" *Organic Electronics* 65 (2019), 1–7. (IMPACT FACTOR 3.49)
7. A. K. Mukherjee, **N. Kumari** "Current voltage perspective of an organic electronic device" *Physics Letters A* 382 (2018) 1413–1418. (IMPACT FACTOR 2.09)
8. N. Yadav, K. Bhargava, **N. Kumari**, S. S. Pandey, V. Singh "Comparative Analysis of Metal Diffusion Effects in Polymer Films Coated with Spin Coating and Floating Film Transfer Techniques" *Synthetic Metals* 264 (2020) 116378. (IMPACT FACTOR 2.53)
9. K. Bhargava, N. Yadav, **N. Kumari**, S. S. Pandey, V. Singh "Reduced contact resistance in organic field-effect transistors fabricated using floating film transfer method". Submitted to *Thin Solid Films* (IMPACT FACTOR 1.89)
10. **N. Kumari**, M. Pandey, A K Mukherjee, S. Nagamatsu, M. Nakamura, S. S. Pandey " Bistable Resistive Switches Fabricated with Layer-by-Layer Printing of Conjugated Polymers". In preperation
11. **N. Kumari**, M. Pandey, S. Nagamatsu, M. Nakamura, S. S. Pandey "Solvent assisted Friction Transferred edge-on Oriented Polymer Thin-film Organic Field Effect Transistors". Submitted to *ACS Appl. Mater. Interfaces* (IMPACT FACTOR 8.45)

12. **N. Kumari**, M. Pandey, S. Nagamatsu, S. S. Pandey "Orientation of Semiconducting Polymers via Swift Printing and Drawing Techniques for High Performance Organic Electronic Devices". (in preparation for *Organic Electronics*)

PUBLICATION (in Conference Proceedings) (***** Presenting Author)

1. **N. Kumari***, M. Pandey, A. S. M. Tripathi, S. Nagamatsu, S. Hayase, S. S. Pandey "Facile fabrication of large area oriented conducting polymer films and their swift characterization through two-dimensional positional profiling" The Society of Nanometric Interfacial Controlled Electronic Devices (NICE 2019-2), The Japan Society of Applied Physics 19 (2019) 7-12.
2. **N. Kumari**, S. Nagamatsu, S. S. Pandey* "Orientation of Semiconducting Polymers via Swift Printing and Drawing techniques for High Performance Organic Electronic Devices" AM-FPD'20 Japan (Invited paper).

Presentations

International Conferences (* Presenting Author)

1. N. Kumari, S. Nagamatsu, and S. S. Pandey "Orientation of Semiconducting Polymers via Swift Printing and Drawing Techniques for High Performance Organic Electronic Devices" Submitted to AM-FPD20, The 27th International Workshop On Active-Matrix Flatpanel Display And Devices, September 1-4, 2020 (on schedule) Ryukoku University Avanti Kyoto Hall, Kyoto, Japan (Oral, Invited).

2. N. Kumari, M. Pandey, S. Nagamatsu, M. Nakamura and S. S. Pandey "Effect of dielectric interface on charge transport anisotropy in polymer thin-film transistors fabricated by friction transfer method" 67th Spring meeting of Japan Society of Applied Physics (JSAP), Yotsuya Campus, Sophia University, Tokyo, Japan Mar 12-15, 2020, 13p-A409-1 (Oral)

3. S. Jana, R. K. Pandey, **N. Kumari**, T. Manaka, S. S. Pandey, R. Prakash "Investigation of molecular orientation in thin films of polythiophenes fabricated on air-liquid interface" 67th Spring meeting of Japan Society of Applied Physics (JSAP), Yotsuya Campus, Sophia University, Tokyo, Japan Mar 12-15, 2020, 13p-A409-2 (Oral)

4. Shyam S. Pandey, **Nikita Kumari**, Shubham Sharma, Shuichi Nagamatsu, Shuzi Hayase "Molecular Orientation and Device Performance in Organic Electronic Devices: Control & Visualization" 7th International Symposium on Applied Engineering and Sciences (SAES2019) 11th–12th November 2019, Malaysia Universiti Putra Malaysia, Serdang, Selangor, Malaysia (Keynote, Materials Sciences).

5. N. Kumari, S. Nagamatsu, S. S. Pandey y "Molecular Orientation and 2D Positional Mapping: A Facile and Powerful Approach for Organic Electronic Devices" EM-NANO 2019 at AQUA Incubation center, Shinshu University, June 19-22, 2019, B2-4 (Oral, Invited)

6. S. Sharma, **N. Kumari**, S. S. Pandey "Impact of the Regio specificity on the Molecular Self Assembly in P3HT Thin Films Prepared by FTM" ICANN2019, IIT Guwahati, Dec 18-21, 2019, A1063 (Poster)

7. N. Yadav, **N. Kumari**, S. S. Pandey, V. Singh "A Comparative Study Related to Nature of Interfer between Metal and Conjugated Polymer: Role of Molecular Ordering" 32nd International Microprocesses and Nanotechnology Conference (MNC2019), International Conference Center Hiroshima, Japan, Oct 28-31, 2019, 29D-2-4 (Oral)

8. Shubham Sharma, **Nikita Kumari**, Shuichi Nagamatsu, Shyam S. Pandey "Investigation of Molecular Self-Assembly in Oriented Thin Films of RRP3HT Prepared by Ribbon-Shaped FTM" 7th International Symposium on Applied Engineering and Sciences (SAES2019) 11th–12th November 2019, M-18, Malaysia Universiti Putra Malaysia, Serdang, Selangor, Malaysia, Malaysia.

9. N. Kumari, M. Pandey, R. K Gupta, A. K. Vats, S. Nagamatsu, S. Hayase and S. S. Pandey "Alkyl-Chain Length Dependent Optical and Electronic Properties of Donor-Acceptor Copolymers" ICMAT 2019 and IUMRS-ICA 2019 at Marina Bay Sands, Singapore, June 23- June 28 on dated 27 June 2019, Sym-h-09, (Poster).

10. S. S. Pandey, M. Pandey, **N. Kumari**, A.S.M. Tripathi, S. Nagamatsu and S. Hayase "Large Area Molecular Orientation of Conjugated Polymers and its Visualization by 2D Positional Mapping for Organic Electronics" ICMAT 2019 and IUMRS-ICA 2019 at Marina Bay Sands, Singapore June 23- June 28 on dated 28 June 2019, Sym-P-10, (Oral, Invited).

11. N. Kumari, M. Pandey, S. Nagamatsu, S. Hayase and S. S. Pandey "Improvement in the Performance of Organic Schottky Diodes through Combined Effect of Charge Double Layer and Oxide Interlayer" 66th Spring meeting of Japan Society of Applied Physics (JSAP), Tokyo Institute of Technology, March 9-12, 2019. 10a-S222-6, (Oral).

12. N. Kumari, M. Pandey, A.SM Tripathi, S. Nagamatsu, S. Hayase and S. S. Pandey "Two-Dimensional Positional Mapping of Macroscopically Oriented Thin Films of Organic Semiconducting Polymers" 6th Symposium on Applied Engineering And Sciences (SAES), Kyushu Institute of Technology, December 15-16, 2018, C-17 (Oral)

13. A. S. M Tripathi, **N. Kumari**, S. Nagamatsu, S. Hayase and S. S. Pandey "Utilization of Oriented Conjugated Polymer Film Prepared by ribbon shaped FTM Towards Its Application for Flexible Organic Field Effect Transistor" 6th Symposium on Applied Engineering And Sciences (SAES), Kyushu Institute of Technology, December 15-16, 2018, C-19 (Oral)

14. S. S. Pandey, M. Pandey, **N. Kumari**, A.S.M. Tripathi, S. Nagamatsu and S. Hayase "Correlating Molecular Orientation and Device Performance in Organic Electronic Devices based on Oriented Thin Films of Conjugated Polymers" 6th Symposium on Applied Engineering And Sciences (SAES), Kyushu Institute of Technology, December 15-16, 2018, C-37 (Oral)

15. S. S. Pandey, M. Pandey, **N. Kumari**, A.S.M. Tripathi, S. Nagamatsu and S. Hayase "Orientating Thin Films of Conjugated Polymers by FTM and Its Visualization by 2D Positional Mapping for Organic Electronics" India-Japan Workshop on Biomolecular Electronics and

Organic Nanotechnology for Environment Preservation (IJWBME-2018), NPL, New Delhi, India December 6-9, 2018 (Oral; Invited)

16. N. Kumari, S. Sadakata, M. Pandey, S. Nagamatsu, S. Hayase and S. S. Pandey "Positional profiling of optical anisotropy in large area oriented conducting polymer films by an ingenious and economical approach" ICSM 2018, July 1-6, 2018, Busan, Korea, MA3-03 (Oral).

17. S. Pandey, M. Pandey, A.S.M. Tripathi, S. Sadakata, **N. Kumari**, S. Nagamatsu, S. Hayase "FTM as A Highly Facile Method towards Fabrication of Macroscopically Oriented Thin Films for Anisotropic Electronic Devices" International Conference on the Science and Technology of Synthetic Metals (ICSM) 2018, July 1-6 Busan, South Korea, MoA2-03, (Oral).

Acknowledgment

I would like to extend my most sincere gratitude to **Prof. Shyam S. Pandey**, my Ph.D. supervisor. Throughout the last three years, he remained the continuous source of inspiration, motivation, and knowledge for me. His keen interest in futuristic technological innovations inspired me to explore the new possibilities for clean fabrication techniques. He was always there to solve any issues with the experiments or with my conceptual understanding; moreover, he also trusts the scientific instincts of the students and provides adequate guidance as well as the freedom to explore the possibilities at its fullest. His such qualities helped to become a competent researcher. From his work ethics and time management, I learned a lot and which certainly will be helpful for me to become a sincere professional as well as a good human being.

I am highly grateful to **Prof. Shuichi Nagamatsu** for his invaluable support throughout my research works. His experience in the field of organic electronics was immensely beneficial for me and scientific discussions with him were very helpful for me to understand many key concepts of this area. I am thankful to **Prof. Shuzi Hayase** for providing many required research facilities. I am also sincerely thankful to **Prof. Masakazu Nakamura** for providing many experimental facilities as well as feedback on my work, which improved the quality of my research works a lot.

I am thankful to **Prof. Ayash Kanto Mukherjee** from IIT Patna who recommended for me for the Ph.D. course here. His consistent support and guidance also helped me a lot.

I am very grateful to my whole family for their belief, patience, and understanding. Although I stayed away from them for the last three years, their support was a great source of joy, happiness, and motivation for me. I would like to extend my profound gratitude to my mother **Mrs. Asha Kumari**, she always provided me mental support and comfort whenever I faced disappointment or struggled in life.

I am sincerely thankful to my senior **Dr. Manish Pandey**, who always provided his guidance and critical feedback right from the inception of an idea, through the planning, and also during the execution and compilation of the research works. His consistent support was very helpful to me. I would like to thank my other seniors and colleagues also **Dr. Kapil Gaurav**, **Dr. Kengo Hamada**, **Mr. Daisuke Hirotani**, and **Ms. Shifumi Sadakata**, for providing all sorts of help throughout my Ph.D. work. I am also grateful to KIT for providing me all kinds of facilities including various scholarships and different financial support for attending domestic and overseas conferences. I am very thankful to the staffs of the international division for their kind help.